Application of quantitative cross-linking mass spectrometry methods to study interactome differences.

Anna Bakhtina

A dissertation

submitted in partial fulfillment of the

requirements for the degree of

Doctor of Philosophy

University of Washington

2024

Reading Committee:

James E. Bruce, Chair

Michael J. MacCoss

Shao-En Ong

Program Authorized to Offer Degree:

Genome Sciences

University of Washington

Abstract

Application of quantitative cross-linking mass spectrometry methods to study interactome differences.

Anna Bakhtina

Chair of the Supervisory Committee:
James E. Bruce
Genome Sciences

Proteins carry out the vast majority of biological function inside living cells. They do so by changing their shapes, interacting with one another and other molecules such as DNA and RNA. Gaining an understanding of intra and inter molecular protein interactions on a systems-level would allow for much deeper understanding of how biological functions are performed and regulated. Quantitative comparisons of these interactions between different systems or upon perturbations can increase understanding of remodeling associated with the aging, disease, and treatments. Here, cross-linking mass spectrometry is demonstrated with quantitative comparisons of protein interactions within intact systems, such as cells and membrane bound organelles. This work shows that reproducible remodeling of interactomes associated with aging in skeletal muscle mitochondria can be detected with isobaric quantitative protein interaction reporter (iqPIR) technologies. Moreover, changes in the interactome showed correlation with

age-associated mitochondrial functional decline. Interactome differences associated with distinct functional differences in different cell types were also observed. Quantitative comparison of interactomes of human cell lines HEK293, HeLa and MCF7 uncovered differences in chromatin remodeling, mitochondrial transport and others that are independent of protein abundance levels. Utilizing a novel genetic mouse model that allows isolation of mitochondria from tubule or podocyte kidney cells, quantitative cross-linking and mass spectrometry enabled identification of differentially regulated proteins and pathways in mitochondria within these cell types that would otherwise remain unknown.

TABLE OF CONTENTS

LIST OF FIGURES

ACKNOWLEDGEMENTS

I would love to thank Dr. Matthew Bush for giving me an opportunity to join my first research lab as an undergraduate student and for introducing me to the field of mass spectrometry. Dr. Kimberly Davidson, a graduate student in the lab was a great first mentor and showed a lot of patience and support. My post-graduate work in the lab of Dr. Sarah Franklin was my first introduction to proteomics and research as a full-time job. I am grateful to Dr. Franklin for giving me the opportunity and trusting me with the responsibility to manage lab's mass spectrometer. I would love to thank Aman Makaju, who was my first mentor in the lab and introduced me to the ins and outs of proteomics research. Dr. Marta Szulik and Dr. Junco Warren were great mentors too and a pleasure to work with. My fellow lab mates Emilee Horiuchi, Steven Valdez, Dr. Katie Davis, Dr. Sam Hickenlooper made the lab a fun place to be. I would love to thank Brian Giebel, Maureen Larsen, Sarah Pressl, who made life at Genome Sciences so much easier and whole grad school experiences much less stressful. I want to thank my mentors during my rotations, Dr. Judit Villen, Dr. Ian Smith, Dr. Mike MacCoss, Dr. Brooke Nunn. Amazing experience in their lab made choosing a lab to join so much harder. I want to thank Dr. Jim Bruce for giving me the opportunity to learn the whole new field of cross-linking mass spectrometry and to allow me to participate in so many exciting projects. Dr. Juan Chavez was a great mentor and a great source of knowledge about pretty much anything. Drs. Helisa Wippel, SungGun Park, Nate Kaiser and Andy Keller were great mentors and incredible people to work with. My fellow students, Dr. Martin Mathay and Dr. Jared Mohr became good friends and mentors too. My partner, Evan Leahy, offered support and encouragement when everything seemed impossible. His wonderful family always made me feel included and supported. Most of all, I want to thank my mom, Zoia Bakhtina, whose

immense love and unwavering belief in me made this possible. I also would love to express my gratitude to all the people back home who helped her and me in most trying times.

DEDICATION

To my mom

“Take the Adventure, heed the call, now ere the irrevocable moment passes!”

-Kenneth Grahame, The Wind in the Willows

Chapter 1. INTRODUCTION

1.1 INTERACTOMICS CAPTURE CHANGES IN PROTEIN BEHAVIOR

Understanding molecular mechanisms behind physiological, pathological and aging processes affecting human health has long been a primary goal of biomedical research. In recent years both established and great advances in molecular omics technologies have revolutionized the depth and scale at which it is possible to interrogate molecular machineries and processes. In general, omics technologies refer to the set of techniques that aim to gain a system level view of all genes (genome)[1], RNA transcripts that are made by transcribing the genes (transcriptome)[2], proteins translated from the RNA (proteome)[3] and their post-translational modifications (PTMs)[4] and small molecules (such as lipids[5] and metabolites[6]) produced by orchestrated work of many proteins (**Figure 1.1**). In the end, changes in any of these "-omes" would lead to change in protein behaviors as proteins are the ultimate effectors in biology. Proteins perform their tasks by changing their positions within the cell, their shapes and their interactions with one another or other macromolecules, such as DNA and RNA, or small molecules, collectively referred to as the interactome. Measurement of the ultimate effects on proteins to elucidate mechanisms behind physiological and pathological processes is a primary aim of the emerging field of interactomics. More traditionally, interactomics has been defined as the study of protein-protein interactions (PPIs) where two distinct proteins interact and/or form stable complexes to perform biological function[7]. But with the developing understanding of importance of interaction between proteins and other macromolecules, such as DNA and RNA, interactions within the protein, i.e. conformations, and interaction between proteins and lipids and metabolites, compels the expansion of a broader definition of the interactome to including all intra- and inter- molecular interactions

of proteins. Therefore, the development of methods that enable capture of different types of molecular interactions and their effects on proteins greatly benefits biomedical sciences.

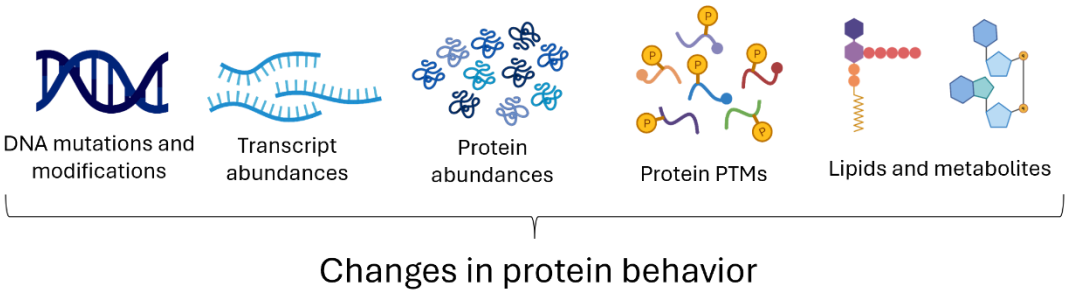

Figure 1.1. 'Omics' technologies to study molecular landscapes of biological systems.

1.2 METHODS TO STUDY MOLECULAR INTERACTIONS AND THEIR ALTERATIONS

Molecular interactions in biological systems have long been studied by various methods. A large focus has been placed on PPIs since how proteins interact with one another and what complexes they form is central to all biological processes[8]. One of the earliest methods to detect binary interactions between two proteins of interest is the yeast two-hybrid which requires genetically modifying the proteins with complementary transcription factors derived domains so the transcription of a reporter gene is activated if proteins interact with one another[9]. Revolutionary at the time, this method has played a central role in both basic research and drug development[10,11]. But it required extensive genetic manipulations that could obscure true PPIs and can be limiting in types of proteins that can be studied. Biochemical methods, such as co-immunoprecipitation uses antibody-antigen specific interaction to "pull down" a protein of interest and proteins that interact with it from cellular and tissue lysates preserving at least some context of PPIs[12]. Interacting proteins can be then determined by either western blotting (necessitating knowing a candidate interactor beforehand) or with tandem mass spectrometry where no prior knowledge is required[13]. Antibody based pull-downs coupled to mass

spectrometry to discover novel PPIs is referred to as affinity purification mass spectrometry (AP-MS)[14]. Advances in quantitative mass spectrometry based proteomic methods allowed to use AP-MS to study changes in PPIs in perturbed systems such as pathologies and drug treatments[15,16]. Over the last decade AP-MS has become a staple in studying PPIs in an unbiased fashion. AP-MS requires target-specific antibodies or modification of bait proteins with an affinity tag, such as FLAG or HA, but several large scale studies where proteomes were systematically tagged to create large scale interaction landscapes have been undertaken[17-19]. While AP-MS is usually applied to complex systems such as cells and tissues, the required disruption of cellular environments (i.e. lysis) can distort the interaction landscape. Proximity labeling methods could be beneficial as selection for interacting proteins happens before cellular structures are disrupted[20]. In proximity labeling experiments, a peroxidase or a biotinylating enzymes are fused to the protein of interest and that converts a small molecule into a short half-life reactive species that can tag, usually with biotin, nearby proteins that are within a 1-10 nm radius. Biotinylated proteins can then be enriched and identified with tandem mass spectrometry coupled to liquid chromatography (LC-MS/MS). Non-biotin-based tagging approaches have also been developed and click chemistry have been utilized for enrichment[21]. This resolved spatio-temporal maps of protein interactions and the study protein trafficking between with the cells[22]. Still these methods require genetic engineering and are unable to provide insight on interacting protein surfaces or any structural information for individual proteins or their complexes. Moreover, interactions between proteins and other molecules, such as nucleic acids or metabolites can be hard to detect, although some exciting developments on this front have recently been shown[23].

Methods that can detect structural alterations in proteins that are caused by changes in PPIs, DNA-protein and RNA-protein interactions, protein PTMs and protein-ligand interactions

without requiring extensive genetic engineering are of great value. Methods that rely on detection of changes in protein surfaces accessibility to various reagents because of a perturbation can be useful in determining affected proteins. Limited proteolysis coupled to mass spectrometry (LiP-MS) leverages a non-specific protease in the native environments and the fact that changes in interactomes can affect the accessibility of protein surfaces to be cleaved[24]. Protein footprinting methods, such as fast photochemical oxidation (FPOP)[25] and hydrogen-deuterium exchange (HDX)[26] utilizes labeling and reports either protein residue side chain solvent accessibility (FPOP) or residue backbone accessibility (HDX) that can be determined with mass spectrometry. Originally limited to purified proteins or cellular lysates these methods are now being extended to *in vivo* studies[27,28]. While LiP-MS, FPOP-MS and HDX-MS can detect effects on proteins caused by perturbations of all inter- and intra- molecular interactions, they do not directly capture any of them. A method that has a readout that preserves at least some of these interactions and allows some interpretation of others could be a holy grail in study of interactomes.

1.3 CROSS-LINKING MASS SPECTROMETRY TO STUDY INTERACTOMES

Cross-linking mass spectrometry (XL-MS) has been implemented to study protein conformations and interactions for several decades now. The central idea in the protein cross-linking is formation of covalent bonds between protein residues that are preserved and can be identified by mass spectrometry. XL-MS experiment starts with application of a cross-linking molecule to the system of interest (**Figure 1.2**)[29]. Cross-linking reagents, usually referred to as cross-linkers, contains several reactive groups (usually two, but cross-linkers with up to four groups have been reported[30]) that are connected by a spacer. The most common reactive groups target side chains of lysine residues but other residue specific and non-specific reactivities have been implemented

too[31-34]. The length of a spacer sets the constraint that is used to calculate maximum allowed distance between cross-linked residues. Only residues that are within the allowed distance and are available for cross-linking (not post translationally modified and are solvent accessible) could be cross-linked. Reactive residues and spacer are the fundamental components of every cross-linker but some cross-linkers have other features greatly increasing their usability. Cross-link formation efficiency in complex systems such as cells and tissues is inherently low: high concentration of lysine residues and a limited concentration possible for a cross-linker due to solubility constraints mean that only a small percentage of residues will actually be cross-linked. Therefore, having a way to enrich for cross-linked peptides can greatly increase the depth of coverage[35]. An enrichable tag can be attached to a spacer. Biotin moiety that can be enriched through an interaction with streptavidin or avidin is a popular choice for a tag[36]. Attachment of negatively charged phospho groups that utilize the same principles for enrichment as phosphopeptides have recently been introduced[37,38]. Click chemistry, a biorthogonal reaction that has had a big impact on the field of chemical biology is also being explored. Versatility of this reaction could, in theory, allow to "click" a large variety of enrichable groups[39]. The enrichment usually is done on a peptide level; therefore, after the cross-linking reaction is complete, the cross-linked system is processed for bottom-up proteomics (the cells, tissues or organelles are lysed and proteins are digested with proteases, such as trypsin). Enrichment alone is usually not enough to achieve meaningful coverage in complex samples, so a fractionation is performed. Most common fractionation methods used are strong cation exchange (SCX) or size exclusion chromatography (SEC)[40]. In SCX peptides mixtures are separated based on a charge while SEC separates based on size. Cross-linked peptides, commonly referred as cross-links, tend to have both larger size than linear peptides (as they include two tryptic peptides connected by a cross-

linker and since a lysine residue in each peptide will have cross-linker attached to it, it won't be available for trypsin during digestion so a lot of cross-linked peptides can be larger because of missed cleavages). For the same reason cross-linked peptides also tend to bear more positive charges at lower pH. This is leveraged by the SCX where a higher concentration of salt is needed to elute cross-links compared to linear peptides. There is another group of peptides derived from XL-MS experiments that show intermediate chromatographic properties in SEC and SCX enrichment. These peptides are formed when only one reactive group of a cross-linker reacts with a lysine residue while the other gets hydrolyzed in an aqueous environment of the cell. These cross-linking products are usually referred to as mono-links or dead-ends (DEs). While they do not provide information about PPIs or intraprotein molecular interactions they can be valuable when assessing specific residues availability for cross-linking due to either solvent accessibility or PTMs[41].

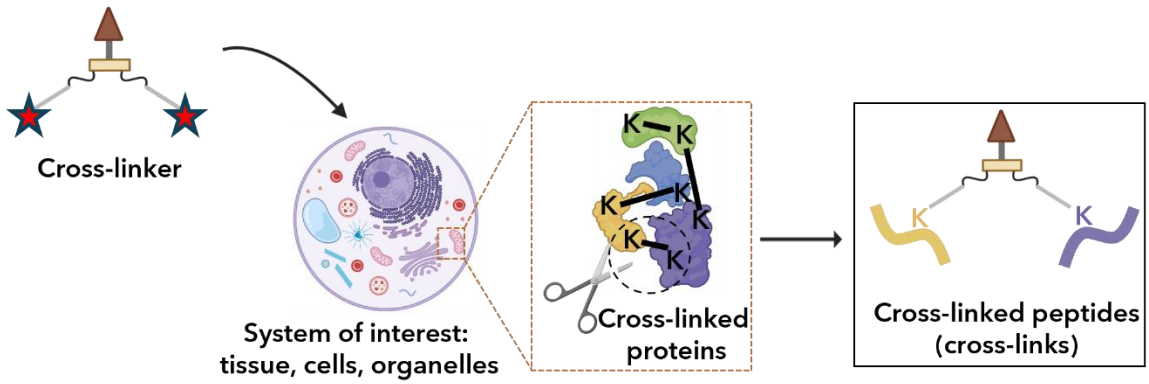

Figure 1.2 Generic XL-MS experimental workflow. Cross-linker molecules are added to a system to be investigated. Cross-linked proteins are then extracted and digested with protease. Covalent cross-link is preserved during digestion. Cross-linked peptides can then be isolated and analyzed using mass spectrometry.

After cross-linked peptides are fractionated and enriched they are ready for LC-MS/MS analysis. Cross-links are separated using reverse phase chromatography, just as in traditional bottom-up

proteomics experiments. The parameters of data acquisition in a mass spectrometer can vary greatly. Depending on a configuration of mass analyzers it is possible to implement real-time analysis where peaks that could potentially be cross-linked species (charge > 3) observed in MS1 scans are selected for fragmentation in MS2 scans [42]. MS2 spectra are analyzed in real time for a potential to contain cross-linked species based on characteristic peaks or if there is a set of peaks that sums up to a precursor mass. How the MS2 spectrum is searched for a relationships that potentially could be cross-linked peptides is cross-linker dependent[42,43]. If there is a relationship, three peaks (one of them being reporter of a known mass, and the other two a potential peptides that were cross-linked) that sum up to a precursor peak, the individual peptides peaks are selected for MS3 analysis used for peptide identification. This workflow depends on the presence of MS-cleavable bonds in the cross-linker. If there were no MS-cleavable bonds incorporated into cross-linker designs, then only MS2 analysis is possible. This makes identification of cross-linked peptides more challenging during data processing as the search space becomes quite large (as each spectrum needs to be searched for a pairwise combinations of peptides not just a single peptide).

In recent years, large scale XL-MS studies have primarily used MS cleavable cross-linkers. One of the MS cleavable cross-linkers is protein interaction reporter (PIR) that has been used for more than a decade now[44]. This peptide based cross-linker incorporates proline-aspartate (D-P) bonds that are MS cleavable (**Figure 1.3**). Moreover, the cleavage of this bonds is symmetrical, meaning that in most cases after the fragmentation there is only one peak corresponding to each peptide unlike other cross-linkers[45]. Although PIR is MS cleavable and can be used with MS3 methods, it has also been shown to be effective using an MS2 strategy[46].In MS2 based PIR experiments, after potential cross-linked species is selected for fragmentation, HCD

fragmentation is used to produce both peaks corresponding to a reporter (a part of a cross-linker that is not attached to a peptide after MS cleavage) and peptides with a stump (a portion of a cross-linker that stays attached to the lysine residue in the peptides). In the same spectrum, a fragmentation pattern along the peptide backbone is produced that could be used for identification. After the data is acquired an algorithm[46] is used to determine MS2 spectra that contain cross-linked peptides and then these spectra are searched against the database allowing for more than one peptide to be selected as a match for each spectrum (**Figure 1.3**)[47]. The results of the search are then used to assemble identified peptides into cross-links and validate the data[48]. PIR based cross-linking experiments have been useful in investigation of viral, bacterial, mitochondrial and cancer related interactomes and changes in them[49-53].

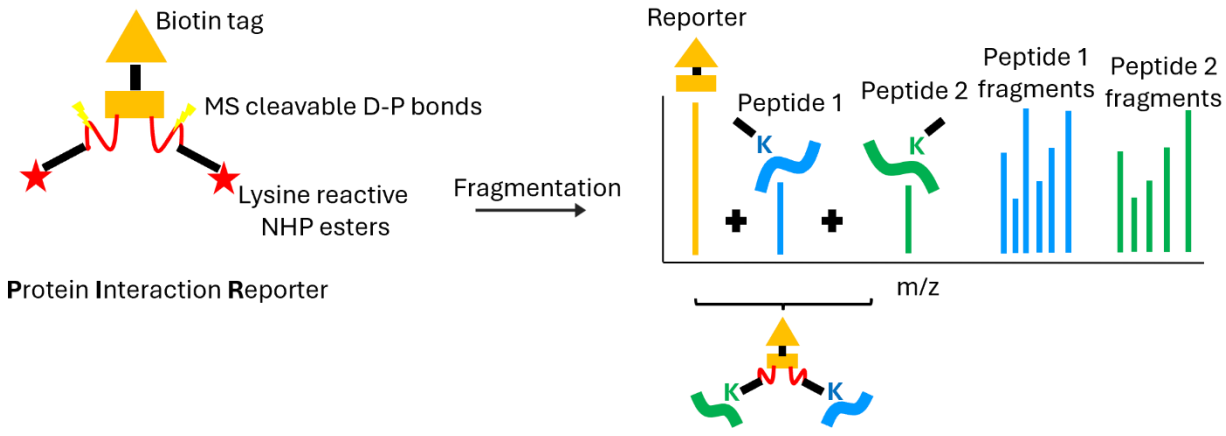

Figure 1.3 Protein interaction reporter and a fragmentation pattern of a cross-linked peptide pair in MS2 space.

1.4 *IN VIVO* QUANTITATIVE CROSS-LINKING FOR STRUCTURAL BIOLOGY

Contents of this section are adapted from the following work: Chemical cross-linking and mass spectrometry enabled systems-level structural biology. Luke Botticelli*, Anna Bakhtina*, Nathan K. Kaiser, Andrew Keller, Seth McNutt, James E. Bruce, Feixia Chu. *In revision* at CURR OPIN STRUC BIOL

Over the last two decades XL-Ms has been applied to study systems of varying complexities, from a single purified proteins or protein complexes to cellular lysates. One of the great advantages of XL-MS is that unlike traditional structural techniques, such as X-ray crystallography and cryo electron microscopy, it can be used to capture protein interactions and conformations in the native environments, i.e. intact organelles and cells. This is known as in *vivo* XL-MS as it is performed on intact, membrane bound systems (**Figure 1.4**)[54]. While the utility of *in vivo* XL-MS is apparent, it comes with a set of challenges. Cross-linker used in these experiments has to be membrane permeable and as lysine concentration inside the *in vivo* systems is high, enrichable cross-linkers can be really useful to counteract low cross-linking efficiency. Regardless of the challenges though, in vivo XL-MS is the most useful type of cross-linking experiments to look at the interactomes that are representative of proteins native environments.

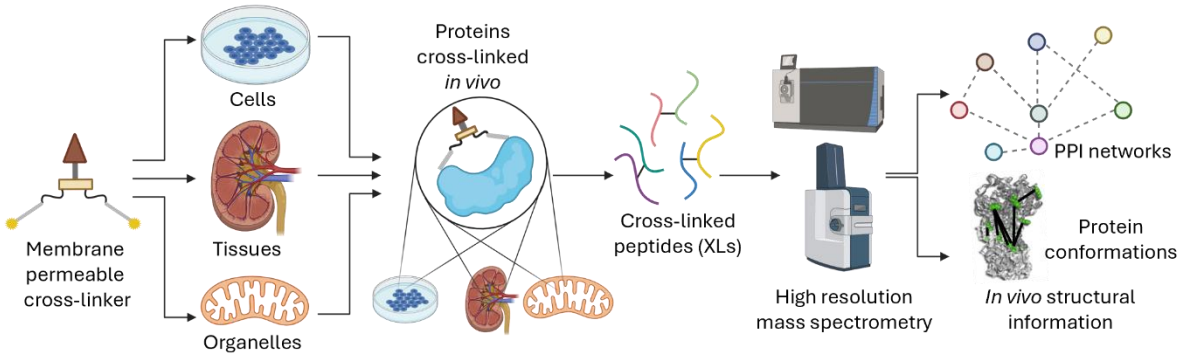

Figure 1.4 In vivo cross-linking workflow. In vivo cross-linking experiments utilize membrane permeable cross-linking reagent to capture native protein-protein interactions and conformations in intact cells, tissues and organelles. After the in vivo reaction is complete, proteins are extracted and digested, cross-links can be additionally enriched by various methods and analyzed on a high-resolution mass spectrometer, such as Orbitrap or TIMS-TOF instruments. Mass spectrometry data is than used to identify cross-links and obtain intra (conformations) and inter (PPIs) protein structural networks representatives on native states.

Methods that can enable quantitative XL-MS (qXL-MS) add another dimension to structural insights. Besides mapping PPI networks, qXL-MS elucidates changes in cross-linked levels in

different samples. This capability informs how protein conformations, interactions, and/or modification levels are altered [55]. While SILAC and isotope labeled cross-linkers enable MS^1-based XL quantitation (**Figure 1.5**)[56-58], qXL-MS strategies have also been developed that rely on traditional quantitative proteomics methods, such as parallel reaction monitoring (PRM)[59], tandem mass tag (TMT)[60] , label free quantitation (LFQ)[61], Data Independent Acquisition (DIA)[62], or qXL-MS specific methods such as isobaric cross-linker approaches[63]. Implementation of traditional quantitation methods might require optimization for cross-linked samples. For example, identification of TMT-labeled cross-linked peptides benefits from increased normalized collision energy (NCE) compared to unlabeled cross-links[64]. Implementing a stepped NCE resulted in higher reporter ion intensities, necessary for a reliable quantitation, with MS^2 based identification and quantitation outperforming MS^3. Recently, a hybrid strategy utilizing MS^3 for identification and subsequent selection of cross-links with targeted PRM quantitation was used with a commercial cross-linker[65]. LFQ, where cross-link abundance is estimated by integrating its precursor peak in MS^1 scans, was applied to compare respiratory supercomplex formation in WT and transgenic mice[66]. DIA-based quantitative proteome strategies have also supported qXL-MS[62], and further instrumentation advances such as Parallel Accumulation Serial Fragmentation (PASEF) enable XL identification and quantitation from cellular and cell lysate samples[67].

An alternative quantitative approach involves modifying cross-linker molecules by inserting heavy isotopes at specific locations to produce two[63] or multiple isobaric molecules[68] to facilitate multiplexed quantitation of *in vivo* cross-linked peptide levels[69]. Isobaric cross-linkers such as isobaric quantitative Protein Interaction Reporter (iqPIR) reagents enable quantitation in MS^2 spectra using multiple peptide, fragment ions and replicate measurements to determine variance and establish statistical confidence filters on quantified ratios (**Figure 1.5**)[70]. Apportionment

algorithms are employed to the overlapping isotope envelopes of stump-containing peptide and fragment ions on the basis of the predicted relative peak intensities[70]. Encoding quantitative information into cross-linker molecules can reduce variability associated with sample processing since cross-linked proteins can be mixed pre-digestion.

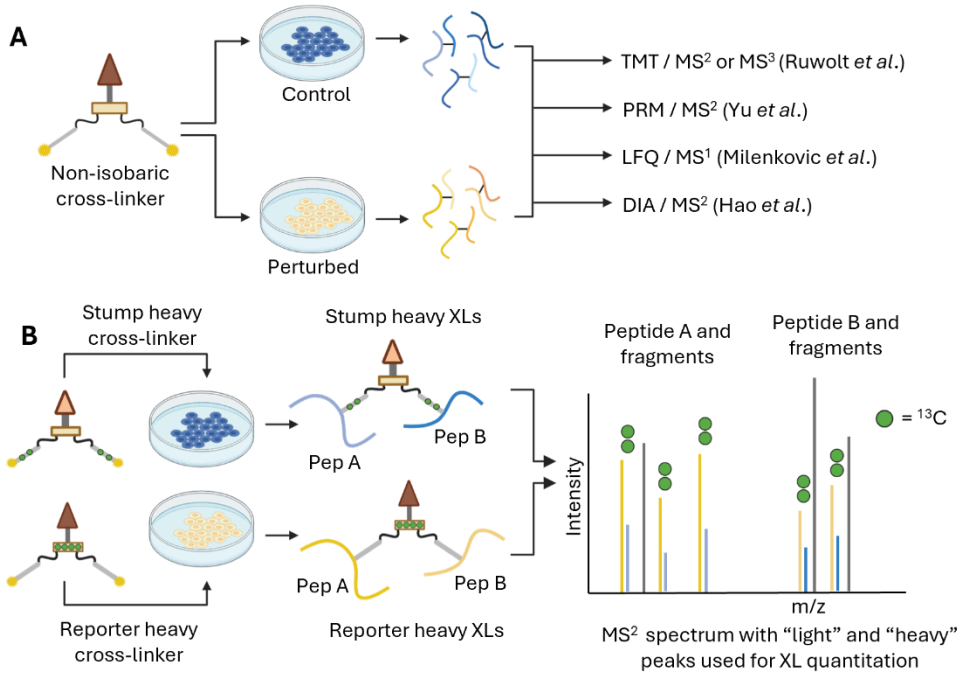

Figure 1.5 Quantitative cross-linking mass spectrometry (qXL-MS) methods. A. In non-isobaric quantitative cross-linking, the same cross-linking reagent is added to the systems to compare, such as perturbed cells and controls. After cell lysis and protein digestion, cross-links can be modified, mixed and enriched together (TMT) or separately (PRM, LFQ, DIA). For the non-isobaric qXL-MS quantitation principles are the same as for linear peptides. B. In isobaric quantitative cross-linking such as iqPIR, a set of isobaric cross-linkers is added to the systems to compare. Cross-linked peptides from one system will bear a heavy cross-linker and cross-linked peptides from the other a light cross-linker. Proteins can be mixed before the digestion, processed and analyzed together. After fragmentation, peptides and their fragments with lysines that were cross-linked are used to make ratios of heavy and light cross-links that are used for quantitation.

1.5 AIMS OF THIS WORK

In this current work I have applied iqPIR based quantitative cross-linking mass spectrometry to study interactome changes between different cell types and induced by aging. For cell type

interactome differences, I compared three commonly used in biomedical research human cell lines, HEK293, HeLa and MCF-7. I was able to show that qXL-MS allowed us to detect differences that were independent of protein levels. I have demonstrated that combining quantitative interactomics with quantitative proteomics could give a deeper view on molecular differences between complex systems. I have then compared mitochondrial interactomes and proteomes originating from two different cell types with the same organ. Utilizing novel mouse model that allows to isolate mitochondria from either podocyte or tubular cells from mouse kidney, I was able to show that even when proteomes are quite similar, addition of interactome dimension allows to see subtle differences in metabolic processes within the mitochondria of these two cell types. I have also applied qXL-MS to see if there are reproducible interactome changes induced by aging by comparing muscle mitochondria isolated from young and old mice. I have demonstrated that indeed with iqPIR we are able to see the differences and even more excitingly these interactome remodeling correlates with mitochondrial functional decline that is associated with muscle aging. Overall, this work demonstrates how advances in qXL-MS brought by development of iqPIR, opens a door to investigate remodeling of molecular landscapes in health and disease on a new level.

Chapter 2. SKELETAL MUSCLE MITOCHONDRIAL INTERACTOME REMODELING IS LINKED TO FUNCTIONAL DECLINE IN AGED FEMALE MICE.

The contents of this chapter are adapted from the following work: Bakhtina AA, Pharaoh GA, Campbell MD, Keller A, Stuppard RS, Marcinek DJ, Bruce JE. Skeletal muscle mitochondrial

interactome remodeling is linked to functional decline in aged female mice. Nat Aging. 2023 Mar;3(3):313-326. doi: 10.1038/s43587-023-00366-5.

2.1 ABSTRACT

Genomic, transcriptomic, and proteomic approaches have been employed to gain insight into molecular underpinnings of aging in laboratory animals and in humans. However, protein function in biological systems is under complex regulation and includes factors in addition to abundance levels, such as modifications, localization, conformation, and protein-protein interactions. We have applied new quantitative chemical cross-linking technologies to uncover changes in the muscle mitochondrial interactome contributing to functional decline in aging in female mice. Statistically significant age-related changes in protein cross-links relating to assembly of electron transport system complexes I and IV, activity of glutamate dehydrogenase, and coenzyme-A binding in fatty acid beta-oxidation and TCA enzymes were observed. These changes showed remarkable correlation with measured CI based respiration differences within the same young-old animal pairs, indicating these cross-link levels offer new molecular insight on commonly observed age-related phenotypic differences. Each observed cross-link can serve as a protein conformational or protein-protein interaction probe in future studies making this dataset a unique resource for many additional in-depth molecular studies that are needed to better understand complex molecular changes that occur with aging.

2.2 INTRODUCTION

Aging is a complex process involving several interconnected features that contribute to the progressive decline in function, vulnerability to chronic disease, and ultimately death[71]. Among the hallmarks of aging is mitochondrial dysfunction, first proposed as a major component of

aging in 1956[72]. In muscle, aging is accompanied by declines in mass and strength. Decreases in mitochondrial function are thought to be primary mediators of age-related muscle loss[73]. Many phenotypes of aging have been observed in mitochondria including changes in reactive oxygen species (ROS) production, electron transport system (ETS) efficiency and respiration, ATP production, mitochondrial quality control, mitochondrial biogenesis, and mitophagy[74]. Mitochondrial function is among the most significant changes accompanying muscle aging on the cellular level[73,75,76]. Muscle mitochondria have been a primary focus of aging research due to their central role in maintaining metabolic and redox homeostasis, regulating metabolite levels, meeting energy demand during exercise, and the relative ease of muscle biopsy in humans compared to other tissues. Large-scale approaches have been employed to study muscle aging in laboratory animals and humans, including deep quantitative proteomic and transcriptomic profiling of several age groups in humans[77,78] and mice[79-81]. However, protein function is maintained under complex biological regulation and includes factors in addition to abundance levels, such as modifications, localization, conformations, and protein-protein interactions (PPIs). While large-scale studies have been applied to investigate differential mitochondrial protein modifications with age[82-84], quantitation of large-scale changes in protein conformations and PPIs, collectively referred to here as the interactome, have previously not been possible.

Recently developed quantitative cross-linking mass spectrometry technologies (qXL-MS) were applied to elucidate interactome changes in aged female murine skeletal muscle mitochondria contributing to age-related mitochondrial functional decline. Reported here are results from initial investigations of female murine muscle mitochondrial interactomes that enable identification of statistically significant changes associated with aging. Recently advanced

isobaric quantitative protein interaction reporter (iqPIR) technologies enabled reproducible detection of age-related mitochondrial interactome changes[70]. Muscle mitochondria from young and old mice were isolated and cross-linked with iqPIR molecules (**Figure 2.1**). Young and old mitochondrial samples were paired, processed, and analyzed to quantify age-related mitochondrial interactome changes. Before cross-linking, mitochondrial protein yield was measured together with functional measurements such as oxygen consumption rates on Complex I (CI) and Complex II (CII) substrates and citrate synthase (CS) activity. This allowed the initial correlation of age-related mitochondrial phenotypic or functional changes with molecular level interactome remodeling. In addition to changes in PPIs, quantifying site-specific interaction of the iqPIR reporter molecules provides new insights into protein activity by identifying changes in 1) protein structure associated with activity, as in glutamate dehydrogenase, described below and 2) substrate binding to protein active sites. Among these data, significant age-related decreases in cross-link levels within the antenna domain of glutamate dehydrogenase (DHE3) were observed that correlated with decreased glutamate and malate driven respiration. Similarly, CI late-stage assembly and binding of cytochrome c oxidase subunit NDUFA4 (NDUA4) subunit to complex IV (CIV) was impaired and correlated with decreased CI-linked respiration. Traditional methods, such as blue native polyacrylamide gel electrophoresis (BN-PAGE) can distinguish large assemblies but lack resolution to provide quantitative differences between late stage assemblies[85]. Moreover, BN-PAGE can only enable visualization of complexes that survive extraction and interactions of ETS complex subunits like NDUA4 appear highly dependent on extraction conditions. Thus, qXL-MS is uniquely suited to study changes in complex assembly and composition and provide biological insight on ETS dysregulation observed with aging. Finally, as previously shown with qXL-MS data[59], each identified link can

be targeted with parallel reaction monitoring (PRM) methods in other labs to visualize conformational and interactome changes with many other perturbations or interventions. Therefore, in addition to biological insight on large-scale age-related protein conformation and interaction changes discussed below, these data can serve as a resource for many additional studies to better visualize molecular changes underpinning age-related mitochondrial functional decline.

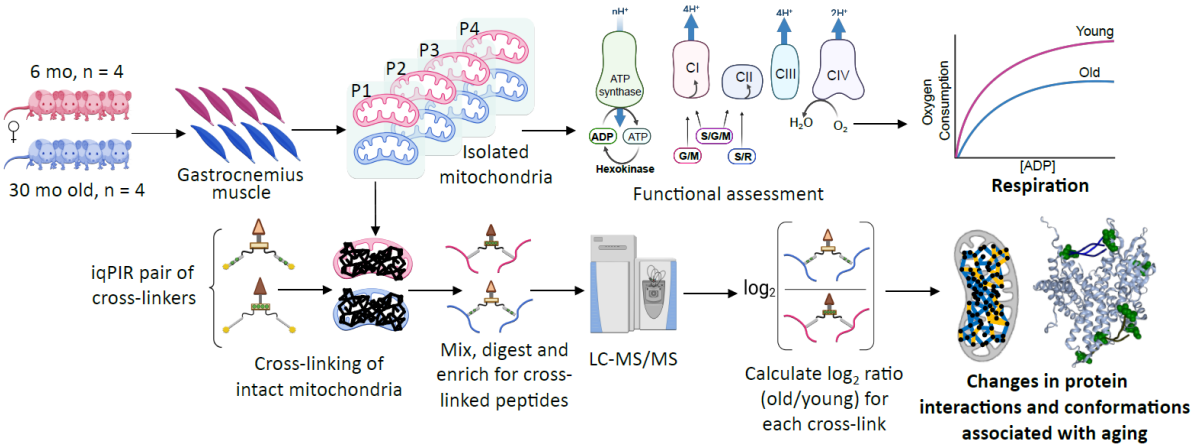

Figure 2.1 Experimental workflow. Gastrocnemius muscle was excised from 4 young (6 months) and 4 old (30 months) female mice and mitochondria were isolated. Each mitochondrial pellet (n = 8) was resuspended, and part of the homogenate was used to measure oxygen consumption for CI: glutamate and malate (G/M), CII: succinate and rotenone for inhibiting CI (S/R), and CI&CII: succinate, glutamate, and malate (S/G/M). Mitochondria from the same homogenate were then cross-linked with binary iqPIR reagents: mitochondria from old mice (n = 4) were crosslinked with reporter heavy (RH) and mitochondria from young mice (n = 4) were crosslinked with stump heavy (SH) iqPIR molecules. Mitochondria were then lysed, proteins were reduced, alkylated, and mixed in a 1:1 ratio based on total protein mass for each young old mouse pair and digested with trypsin overnight. Cross-linked peptides were by strong cation exchange and avidin capture of biotin tag on the cross-linker. Peptides were then separated by LC and MS2 spectra were collected for peptides with charge greater or equal to 4. The data were processed, and abundance of each cross-linked peptide pair was determined using newly developed iqPIR informatics. The dataset was uploaded to XLinkDB to view cross-linked peptides, quantitation, protein and complex structures and networks among other dataset features.

2.3 RESULTS

2.3.1 *Generation of mitochondrial interactome of aged muscle*

Samples from four old (30 months) and four young (6 months) female mice were cross-linked and then paired into four direct comparisons of individual old and young samples (one young and one old mouse in each pair designated P1, P2, P3, P4) for mass spectrometry analysis. The pairings were assigned based on mitochondrial protein content of each sample to maximize protein amounts. In total, 1864 cross-linked peptide pairs, hereafter referred to as cross-links, were identified at 1% cross-link level FDR from these four pairs. 533 cross-links are interprotein (formed by lysine residues originating from two distinct proteins) and 1331 are intraprotein (from the same protein). Mapping all identified intralinks on to recently predicted structures[86] shows that 931 (89%), the overwhelming majority of intralinks, agree with the models: Euclidean distances between alpha carbons of cross-linked lysine residues are less than or equal to 35 angstroms (Figure 2.7). Interlinks are formed between two proximal proteins, so it is expected that these two proteins are localized together within mitochondria. 80% (393) of identified interlinks are between inner membrane associated proteins and only two interlinks are between proteins that are not expected to colocalize (matrix and outer membrane) based on submitochondrial localization information from Mitocarta 3.0 with each pair of interlinked proteins (**Figure 2.2**)[87]. Mapping of intralinks shows that most intralinks are from matrix and inner membrane proteins. Overrepresentation of interlinks from inner membrane proteins is most likely due to many multisubunit protein complexes associated with the inner membrane (**Figure 2.2**).

Median normalized $\log_2$ ratios of confidently quantified crosslinks (no more than 1 missing value across biological replicates and 95% confidence < 0.5) in aged mitochondria compared to young,

follow normal distribution, except biological replicate 4 (**Figure 2.2**). On average, at least 7 ions were used to derive each log_2 ratio (Figure 2.7) increasing confidence in each cross-link quantitation. To produce a log_2 ratio for a given cross-link, it must be present in both channels in a pair: reporter heavy (RH) cross-link in old sample and stump heavy (SH) cross-link in young. On average, 1156 cross-links are quantified in each replicate (1229, 1099, 1001, 1297 respectively), meaning that the majority of the cross-links were formed in both samples, making it unlikely to form by chance. Quantitation with iqPIR technologies and informatics showed excellent reproducibility based on observed pairwise Pearson's R values between 0.5 and 0.76 (**Figure 2.2**). Redundancy in cross-link quantitation exists in some cases because multiple peptide sequences with redundant linkage can be formed during sample processing due to trypsin missed cleavage events during digestion or from methionine oxidation. These cases offer internal quality control on quantitation. Log_2 ratios for such multiple cross-links generally show excellent agreement (Figure 2.7) and further increase confidence in quantitation for a residue pair. Cross-links quantified in every sample show remarkable agreement across the four biological replicates (**Figure 2.2**). Reproducibility and robustness of quantitative values produced by the iqPIR method enabled identification of cross-links with statistically significant changes (Bonferroni corrected $p \leq 0.05$) in aging mitochondria (**Figure 2.2**). There is no submitochondrial enrichment of significantly changed links compared to all cross-links (Figure 2.7). Analysis of KEGG pathways and GO biological processes show enrichment in proteins involved in glutamate metabolism, tricarboxylic acid (TCA) cycle, and oxidative phosphorylation (**Figure 2.2** and Figure 2.7). As expected, total mitochondrial protein recovered from each gastrocnemius following isolation was lower in aged samples due to muscle atrophy and decreased input (**Figure 2.2**). However, CS activity expressed per mg protein was significantly increased

following mitochondrial enrichment in aged samples (**Figure 2.2**). This finding is consistently reported for isolated muscle mitochondria in the literature, and CS activity is a better metric of mitochondrial content when comparing across ages than mitochondrial protein content in enriched fractions[88]. Respiration rates in aged mitochondria are significantly decreased when expressed per CS activity (**Figure 2.2**, Figure 2.7).

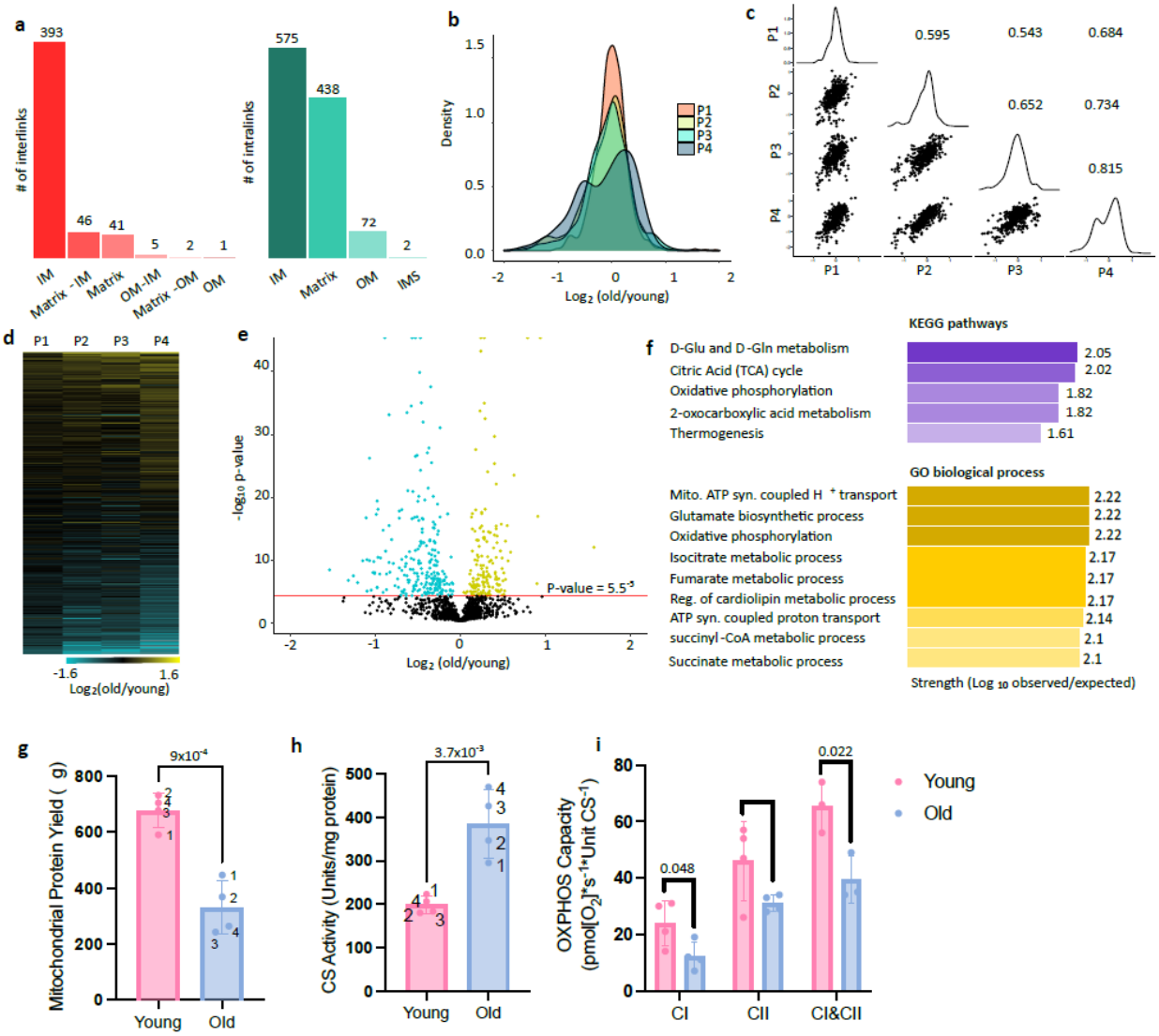

Figure 2.2. Quantitative cross-linking enables detection of reproducible changes in the interactome of aging mitochondria. a. Sub-mitochondrial localization of protein pairs identified in interprotein links (left) and proteins with intralinks (right). b. Distributions of $\log_2$ ratios (old/young) of confidently quantified XLs for each biological replicate. Pairwise correlation plots (c) of confidently quantified cross-links (no missing values and 95% confidence interval <

0.5 for each ratio) with Pearson's R values between 0.54 and 0.81 and heat map (d) show reliable and reproducible quantitation of cross-links. e. Confidently quantified cross-links (no more than 2 missing values and 95% confidence interval < 0.5 for each ratio) with significant changes (Bonferroni corrected p-value < 0.05 from two-sided t-test). f. KEGG and GO Pathways enriched in the cross-links with statistically significant changes (FDR corrected p-value < 0.01) arranged by strength: $\log_{10}$ (observed / expected). This measure describes how large the enrichment effect is. It is the ratio between the number of proteins in the network that are annotated with a term and the number of proteins that we expect to be annotated with this term in a random network of the same size. g. Protein yield from mitochondrial enrichment of both gastrocnemius muscles is decreased with age and (h) CS activity per mg protein in the mitochondrial enrichments is increased with age. Each rep of young and old mitochondria is denoted by a number next to the data point. i. Maximum oxidative phosphorylation (OXPHOS) capacity of the ETS from isolated mitochondria with CI substrates (glutamate and malate), CII substrates (succinate and rotenone), or combined CI&CII substrates (glutamate, malate, and succinate) measured as oxygen consumption rate (OCR) at saturating ADP concentrations normalized to units of CS activity. Statistical significance in g-i determined by unpaired two-tailed student's t-test. Mean ± SD. Exact p-values from two-sided Student's t-test are shown for comparisons that are statistically significant.

2.3.2 *Complex I and Complex IV integrity are impaired with age.*

The present mitochondrial interactome studies resulted in identification of many cross-links originating from ETS complexes and supercomplexes (SC) or respirasome interlinks. Respiratory electron transport and CI biogenesis have been reported as the top pathways affected in aging muscle on a transcriptome level but also the pathways that have the lowest correlation between transcript and protein levels, making the interpretation of its role in aging muscle more complicated[89]. Decreased NAD^+/NADH is a hallmark of cell senescence and aging in muscle tissues and is driven in part by CI activity[90]. CI consists of a membrane embedded part and protruding matrix arm that each assemble independently[91]. In the matrix arm there are many interlinks as well as intralinks that are either unchanged or slightly increased in aged mitochondria consistent with previous reports of elevated complex I subunit expression in aged mouse skeletal muscle[92]. Conversely, the only matrix arm cross-links with age-related decrease are between NADH-ubiquinone oxidoreductase 75 kDa subunit (NDUS1) and NADH

dehydrogenase [ubiquinone] flavoprotein 1 (NDUV1) subunits (**Figure 2.3**), yet all intralinks in each subunit are either unchanged or increased (**Figure 2.3**). Comparison of $\log_2$ ratios of NDUS1 – NDUV1 cross-links with $\log_2$ ratios of all other cross-links involving these proteins, including intralinks from both proteins and their interlinks to other CI subunits, revealed a statistical difference (p-value = 9.6*10−6, Welch two-sample t-test excluding P1 from comparison and 1.35*10−5 with all 4 replicates, **Figure 2.3**, Figure 2.8). NDUS1 and NDUV1 interlinks with other subunits in the matrix arm and intralinks in all CI subunits except for NADH dehydrogenase [ubiquinone] 1 alpha subcomplex subunit 8 (NDUA8) also do not change or show slight increase with age (Figure 2.8). Two residues on NDUS1 (K84 and K87) were identified cross-linked to the same residue on NDUV1 (K81). One possible explanation for this observation could involve change in post translational modification (PTM) levels at NDUV1 K81 since it is involved in both links with decreased levels. NDUV1 is a target for desuccinylation by NAD-dependent protein deacetylase sirtuin-5 (SIRT5) and deacetylation by NAD-dependent protein deacetylase sirtuin-3 (SIRT3)[93,94]. However, if modification levels at a particular lysine were altered, one would expect that all quantified cross-links involving this residue will change accordingly, indicating a more or less accessible lysine due to the PTM. NDUV1 intra-link (K81-K104) shows no age-related changes, so increased modification of NDUV1 K81 cannot explain the decreased NDUS1-NDUV1 interlinks discussed above. NDUS1 and NDUV1 are among the last subunits to be incorporated in the complex and thus, this interaction is an indicator of fully assembled CI (**Figure 2.3**)[95]. The cross-links are also close to flavin mononucleotide (FMN) binding which is a primary site of CI ROS production, making these subunits especially vulnerable to ROS damage[96].

A recently reported CI salvage pathway to achieve efficient maintenance of CI function is accomplished through replacement of damaged subunits instead of assembling the whole complex from scratch[97]. Differential effects of aging on protein abundance and stability of matrix and membrane proteins of CI have been previously reported and are expected to lead to impaired assembly[92,98]. Taken together, these data indicate impaired assembly or elevated turnover of N-module in old mitochondria. Using in-gel activity assays, we find a significant effect of age on CI activity (Figure 2.9). Defects in CI assembly have been shown to lead to increased production of superoxide and premature senescence, and lower abundance of matrix subunits can be a predictor of longevity. There have also been recent reports of coordinated assembly of ETS complexes. In particular, Complex III (CIII) was shown to mediate CI assembly[99]. CIII deficiency led to stalling of CI assembly, especially incorporation of the N-module. Interlinks between CI and CIII as well as several CIII subunit intralinks are also decreased in aged mitochondria (Figure 2.8).

Interlinks between cytochrome c oxidase subunit 6B1 (CX6B1) and NDUA4 of CIV were among the cross-links that exhibited the largest age-related level decreases (**Figure 2.3**). NDUA4 has been identified to be a small subunit of CIV rather than CI as previously thought[100]. NDUA4 is not required for CIV assembly and CIV is functional without it, but loss of NDUA4 impairs CIV activity[101]. No NDUA4 intralinks were quantified in this study, but comparing NDUA4-CX6B1 interlinks to CX6B1 intralinks revealed statistically significant decreases of interprotein link levels, p-value = 5.9*10−6 excluding P1 from comparison and 0.03 with all 4 replicates (**Figure 2.3** and Figure 2.8) indicating reduced interaction between these subunits rather than reduced CIV levels. Recently, structural characterization of CIV containing NDUA4 subunits has been possible by judicious choice of complex extraction/purification conditions[101] revealing

NDUA4 resides at the CIV homodimer interface and precludes CIV homodimer formation[100]. Balsa et al. showed that stable knock down of NDUA4 reduced both the activity and stability of CIV that could be rescued by myc-NDUA4 expression[100]. Therefore, the observed reduction of NDUA4-CIV interaction indicated by multiple reduced NDUA4-CX6B1 cross-link levels would be expected to decrease CIV stability and activity in mitochondria from old mice. Using in-gel activity assays, we find a significant effect of age on CIV activity (Figure 2.9). We have also recently reported decrease of NDUA4-CX6B1 interaction in a mouse model of heart failure, suggesting that similar mechanisms might be at play[102]. A more precise role of NDUA4 and its effects on CIV is not yet clear and is a subject of ongoing studies[103,104].

Increases in heterogeneity and differential rates of aging are well established including in C57BL6/J mice[105,106]. For both CI and CIV links discussed previously, biological replicate one (P1) deviates from other replicates, showing little or no age-related change in these cross-links (**Figure 2.3**). Overall, CI-linked respiration declined significantly in aged samples (**Figure 2.2**). Notably however, the aged sample from P1 had no apparent decline in CI-linked respiration compared to young control, which coincides with this pair demonstrating minimal effects of age on CI protein interactions (**Figure 2.3**). Intriguingly, the magnitude of change in CI assembly cross-links and CX6B1-NDUA4 cross-links in CIV showed strong correlation with decline in respiration on CI substrates across all sample pairs: Pearson's R^2 0.63 and 0.95 respectively, while showing no correlation with CII respiration (**Figure 2.3**, Figure 2.8).

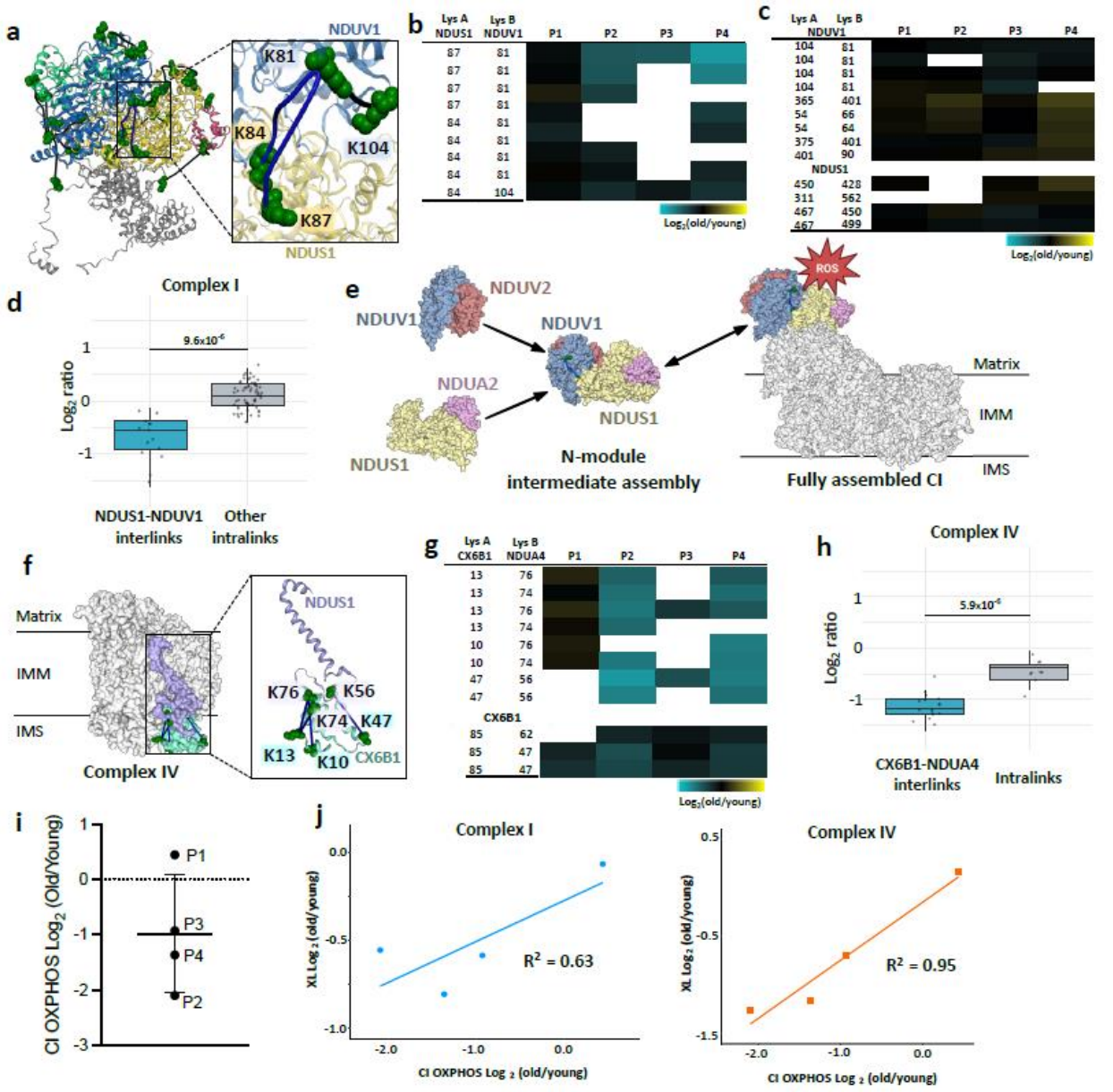

Figure 2.3 Assembly of Complex I and Complex IV integrity is affected in aging muscle.

a. Decreased interprotein cross-links between Nduv1 and Ndus1 mapped to CI structure (PDB 6G72) are shown in blue and non-changing intralinks are shown in black. b. Heatmap of log_2 ratios of NDUS1-NDUV1 cross-linked peptide pairs for each biological replicate (P1, P2, P3, P4). c. Heatmap of log_2 ratios of intraprotein cross-linked peptides from NDUS1 and NDUV1. d. Boxplots of cross-linked peptide pairs in biological replicates P2, P3, P4 (NDUS1-NDUV1 XLs n = 14, other links n = 60; visualized as median and 25th and 75th percentiles, with whiskers indicating minima and maxima) with Welch's two sided t-test show statistically significant difference between NDUS1-NDUV1 interlinks and intralinks and interlinks to other CI subunits. e. N-module is assembled from subcomplexes NDUV1-NDUV2 and NDUS1-NDUA2 at the end of whole CI assembly. It is frequently replaced due to ROS damage. f. NDUA4-CX6B1 interlinks mapped to a CIV structure (PDB 5Z62). g. Heatmap

of log_2 ratios of cross-linked peptide pairs between NDUA4 and CX6B1 (top) and CX6B1 intralinks (bottom). h. Boxplots of cross-linked peptide pairs in biological replicates P2, P3, P4 (CX6B1-NDUA4 XLs n = 16, other links n = 9; visualized as median and 25th and 75th percentiles, with whiskers indicating minima and maxima) with Welch's two-sided t-test show statistically significant difference between NDUA4-CX6B1 interlinks and CX6B1 intralinks. i. Log_2 fold change of CI linked oxidative phosphorylation in old samples compared to young for each pair. Mean ± SD. j. Correlation plots between average log_2 ratios of CI (left) or CIV (right) cross-links changing with age and log_2 fold change in CI respiration for each pair with multiple R^2 shown.

2.3.3 *DHE3 cross-links associated with activation are decreased.*

DHE3 catalyzes interconversion of glutamate and alpha-ketoglutarate (α-KG) and is encoded by the glud1 gene. A primary DHE3 in vivo function involves catalysis of oxidative deamination of glutamate to produce ammonia and α-KG[107], a TCA cycle intermediate. α-KG is also involved in regulation of many cellular processes outside of the TCA cycle, such as epigenetic regulation, protein hydroxylation and ATP synthase regulation (**Figure 2.4**). Connection between DHE3 glycation levels to liver aging has been reported before, but DHE3 abundance levels have not previously been correlated with aging in muscle[108]. In agreement with that notion, two DHE3 intralink levels were quantified that were unchanged in any of the biological replicates, indicating that DHE3 protein levels were unaltered with age. DHE3 exists as a hexamer, comprising a dimer of trimers, and is a subject of intricate and diverse regulatory mechanisms[109]. Each trimer forms a protruding structure where helices from all three subunits form an "antenna" with largely unknown function (**Figure 2.4**). This antenna is only present in higher organisms and coevolved with the complex regulatory network of DHE3, suggesting the antenna may serve in a regulatory capacity[110]. Decreased homodimeric links in the DHE3 antenna region were also among the largest decreased age-related changes quantified in the present study (Figure 2.10Figure 2.9). These included multiple cross-linked peptide pairs arising from missed cleavage products and were observed in all biological replicates, with more moderated changes in P1

where functional decreases were also moderated (**Figure 2.4**, Figure 2.10). Upon substrate binding, DHE3 forms an abortive complex ((DHE3*NAD(P)H*Glu) and its release is facilitated by ADP[109]. Since ADP serves as an activator of DHE3, quantitative cross-linking experiments were also performed with mitochondria isolated from HEK293 cells comparing ADP-treated and control untreated mitochondria. These experiments revealed strong increases in DHE3 antenna homodimer links in both biological replicates (**Figure 2.4**). The combination of ADP-stimulation with old/young interactome data suggests the possibility that DHE3 activity is repressed in aged muscle mitochondria. If so, this may contribute to the observed reduced malate and glutamate stimulated respiration in mitochondria from aged muscle (**Figure 2.2**). DHE3 is essential for delivery of NADH to CI during glutamate/malate stimulated respiration. The decreases of antenna cross-links correlate with change in CI respiration and show no correlation with respiration on CII (**Figure 2.4**, Figure 2.10). The total ability to fuel respiration using glutamate alone is also decreased with age across a range of glutamate concentrations, and a shift in the kinetic response to glutamate stimulation (Figure 2.10).

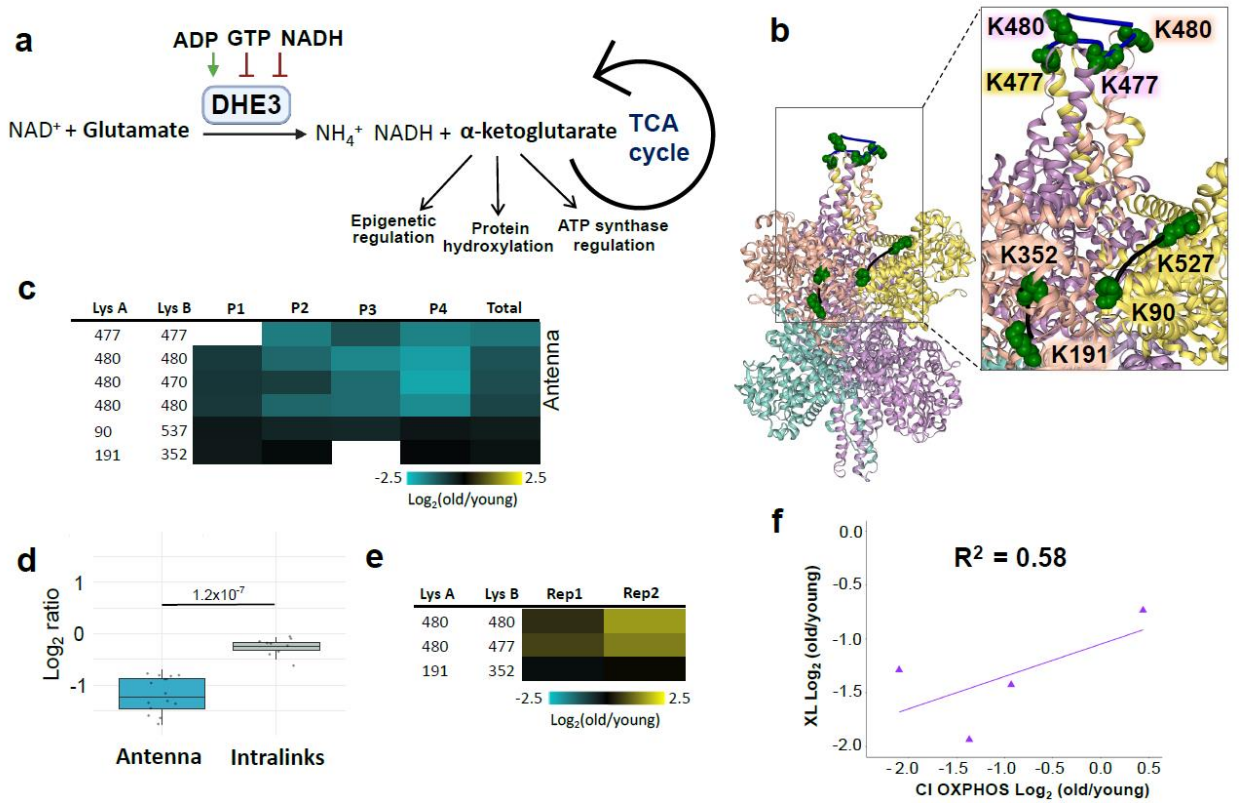

Figure 2.4 Cross-link levels associated with glutamate dehydrogenase (DHE3) activation are decreased in aged mitochondria. a. DHE3 converts glutamate and NAD+ to NADH and α-KG, a TCA cycle intermediate that is involved in many cellular processes. ADP is a potent DHE3 activator while NADH and GTP inhibit it. b. DHE3 cross-links quantified in aging mouse mitochondria; non-changing intralinks are shown in black and decreasing links in the "antenna" (K477-K477, K477-K480, K480-K480) mapped to one of the trimers in the hexamer (bovine structure 6DHM) are shown in blue. c. Log_2 (old/young) ratio for each cross-linked peptide pair in each biological replicate is summarized in heatmap. d. Boxplots of "antenna" ratios and other intralink ratios (antenna XLs n = 19, other links n = 9; visualized as median and 25th and 75th percentiles, with whiskers indicating minima and maxima) with Welch two-sided t-test p-value displayed. e. Heatmap of cross-linked peptide pairs quantified in 2 biological replicates of ADP treated HEK293 mitochondria. f. Correlation between average log_2 ratio for DHE3 antenna cross-links and CI respiration with multiple R^2 shown.

2.3.4 *FAO and TCA enzymes show less accessible substrate sites.*

Impairment of fatty acid metabolism with aging has been shown in multiple organs and models. Aging mouse heart has a decreased free fatty acid flux, TCA cycle flux, and insulin stimulated anaplerosis[111]. Levels of free fatty acids in blood plasma are decreased with age while

triglyceride levels are increased[112]. In addition, muscle contraction leads to a shift in fatty acid oxidation (FAO) and TCA cycle substrate flux and muscle recovery from contraction is impaired with age[113]. FAO and TCA cycle substrates and intermediates show strikingly different patterns in old mice after the unloading and following recovery compared to young mice. Surprisingly though, transcript levels of the proteins involved do not show significant differences, confounding understanding of the mechanisms underlying the changed FAO and TCA cycle fluxes. Many cross-linked peptides from several FAO and TCA enzymes were quantified in this study, including very long-chain specific Acyl-CoA dehydrogenase (ACADV), acetyl-CoA acetyltransferase (THIL), succinate-CoA ligase (ADP/GDP-forming) subunit alpha (SUCA) and succinate-CoA ligase (ADP-forming) subunit beta (SUCB). ACADV, encoded by gene acadvl, catalyzes the first step in beta oxidation. Although the majority of ACADV intralinks showed a slight increase in aged mitochondria, indicating possible slightly elevated protein levels, a subset of four links were significantly decreased in aged muscle mitochondria (**Figure 2.5**, Figure 2.11). All decreased ACADV links span the binding pocket of fatty acyl-CoA and involve residue K279. The ACADV structure PDB: 2IX5 which contains CoA illustrates that CoA phosphate groups reside within salt bridge formation distance from K279 (**Figure 2.5**) suggesting that binding of CoA would reduce link formation at this residue. A similar situation was observed with a subset of 8 cross-link levels (out of 18) quantified in THIL, encoded by acat1, which catalyzes the final FAO step, that showed significant age-related decrease (**Figure 2.5**). These link level changes contrast with the remaining 10 THIL cross-links that either slightly increased or showed no change with age. Of the 8 THIL cross-links that decreased with age, 2 span the CoA binding site and K260 which is also within salt bridge distance with CoA phosphate groups as shown (**Figure 2.5**). Ligand binding can affect cross-link levels within

mitochondria as we demonstrated above; both ACADV and THIL age-related decreased links appear statistically enriched in regions involved in ligand binding indicating age-related differences in FAO exist, despite no significant changes in enzyme levels. THIL functions as a tetramer and tetramer formation is linked to higher activity and cancer progression[114]. We observed decrease in the homodimeric links at the tetramer interface indicating decreased levels of active tetramer.

The final FAO product, Acetyl-CoA, enters the TCA cycle to produce NADH that can then be used by the ETS in oxidative phosphorylation. Significant changes in TCA cycle enzyme cross-link levels in aged mitochondria were also observed, including fumarase (FUMH) (Figure 2.11), SUCA and SUCB1 (**Figure 2.5**). Enzymes SUCA and SUCB1 are subunits of succinate-CoA ligase, which converts succinyl-CoA to succinate that is both a TCA cycle intermediate and an ETS substrate. Both SUCA and SUCB1 exhibited age-related decreased cross-link levels within ligand binding regions, including a cross-link at SUCA K90 which is the SUCA CoA binding site (**Figure 2.5**). Succinyl-CoA ligase also produces ATP (or GTP in some tissues) during generation of succinate, and a nucleotide binding pocket exists in SUCB1. A total of 4 intra-links in SUCB1 were observed with age-related decreased levels, all including K143 cross-links that span the nucleotide binding pocket. Moreover, K108 and K98 in these decreased links exist within a distance compatible with salt bridge formation with GTP phosphate groups as shown in the pig crystal structure (PDB:2FP4). Since other SUCB links appear unchanged with age, these results indicate that age-related conformational differences within the ligand binding sites and not changes in protein levels mediate the observed changes in succinate-CoA ligase. Indeed, with consideration of the entire group of links, observed ratios of cross-links within both CoA and nucleotide binding regions appear significantly different from those in other succinate-CoA

ligase regions (**Figure 2.5**). Although the present age-related changes were measured in young and old murine muscle mitochondria, Wu et al. demonstrated that T cells from rheumatoid arthritis (RA) patients lack sufficient succinyl-CoA ligase activity to maintain balanced TCA cycle metabolic intermediates, implicating acetyl-CoA in controlling pro-inflammatory T cells in autoimmune disease[115]. Cross-links identified in the present interactome data offer new opportunities to investigate succinyl-CoA conformational regulation in RA and possibly many other autoimmune diseases in ways not previously possible. Taken together, these results indicate that this snapshot of the FAO and TCA pathways in aged skeletal muscle demonstrate considerable protein conformational changes linked to reduced ligand binding that are not regulated at the protein level.

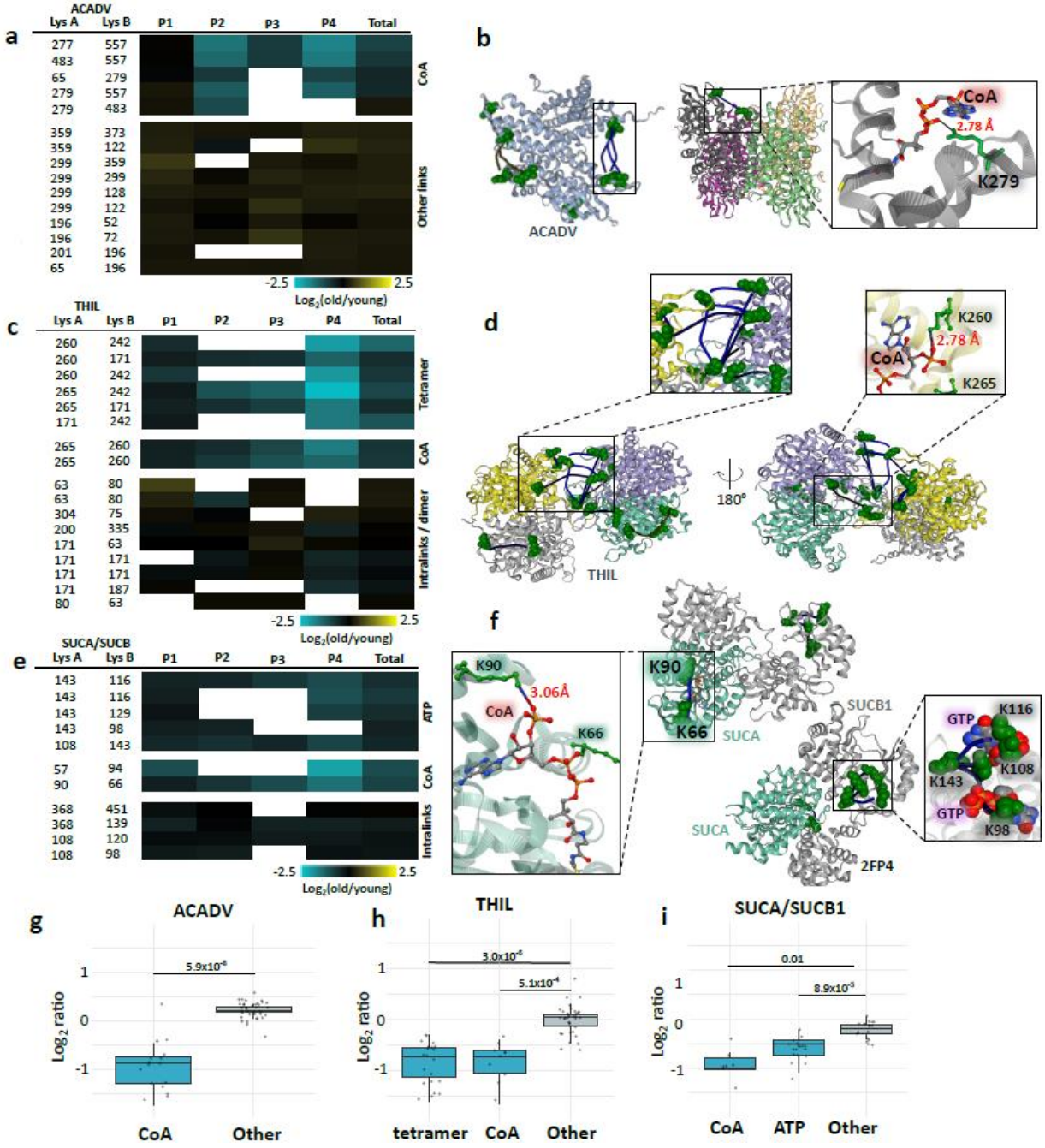

Figure 2.5 Tricarboxylic acid cycle and fatty acid beta oxidation. a. Heatmap of log_2 ratios of all ACADV cross-linked peptide pairs. b. ACADV cross-link at the CoA binding site mapped to A.Thaliana structure, a short chain specific acyl-CoA oxidase in complex with acetoacetyl-CoA (2IX5, left) and all cross-links mapped on a human structure with cross-links at CoA binding site in the box (2UXW, right). CoA from acetoacetyl-CoA is within the distance to form hydrogen bonds with side-chain nitrogen of K279. c. Heatmap of log_2 ratios of THIL cross-linked peptide pairs. d. THIL cross-links mapped to a human structure (2IB8) with zoomed in tetrameric links (left). Cross-links at the CoA binding site were also mapped on a human structure crystalized with CoA (2F2S) showing that K260

is within the salt bridge bond formation distance (right zoomed in panel). e. Heatmap of succinyl-CoA ligase cross-links. f. Succinyl-CoA ligase cross-links mapped on a pig structure of GTP specific succinyl-CoA (4XX0) crystalized with inset view of CoA proximity to SUCA K90 (left). Succinyl-CoA ligase cross-links spanning ATP/GTP binding site mapped to a pig GTP specific structure (2FP4). g, h, i. Boxplots comparing decreased cross-link levels at specific sites to $\log_2$ ratios of all other intralinks for ACADV (CoA proximal XLs n = 10, other links n = 36), THIL (CoA proximal XLs n = 10, tetramer XLs = 24, other links n = 36), and SUCA/SUCB1 (CoA proximal XLs n = 8, ADP proximal XLs n = 19, other links n = 18) visualized as median and 25th and 75th percentiles, with whiskers indicating minima and maxima. Welch's two-sided t-test was used for comparisons and exact p-values are shown on the graphs.

2.4 DISCUSSION

Large-scale mitochondrial interactome quantitation together with functional measurements provide new molecular insights on age-associated functional decline in bioenergetics and metabolism. While previous transcriptome and proteome studies have provided unparalleled ability to visualize molecular abundance level regulation important in aging, it is clear other regulatory mechanisms beyond abundance are also involved. The approach presented here combines quantitation of protein, conformation, modification, ligand binding, and protein interaction levels to provide new biological insight on age-related molecular changes. Recently, the importance of studying protein interactions and their role in aging has been brought to the attention of the community[116]. While this initial study is not comprehensive, these efforts have yielded the largest quantitative interactome dataset to define age-related mitochondrial differences thus far and includes 1521 quantified cross-links.

To date, changes in glutamate dehydrogenase mRNA or protein levels with aging have not been reported and the studies presented here are consistent with that finding. However, the present quantitative cross-linking data generate new insights on DHE3 interactions in mitochondria and age-related conformational differences that may functionally contribute to age-associated changes connecting TCA cycle, ETS and α-KG effects on lifespan. Multiple reports demonstrate α-KG involvement in lifespan extension in mice[117], flies[118], yeast[119] and worms[120]. Increase in

DHE3 activity has also been shown to accompany caloric restriction and subsequent increased lifespean[121]. Moreover, diet-based lifespan extension in flies appears to be dependent on DHE3 expression[122]. α-KG also promotes myofibroblast differentiation through epigenetic regulation by driving histone demethylation and the role of anaplerotic supply from glutamine and glutamate has been highlighted[123]. Interestingly, α-KG effect on lifespan was stronger in female mice compared to males[117]. The decreases in DHE3 antenna cross-link levels presented here are not the result of protein level changes and indicate PTM and or conformational differences exist in aged muscle mitochondria. Age-related increase in PTM levels is possible since both cross-linked residues, K477 and K480 are targets of the sirtuins SIRT3 and SIRT5, with acetylation levels of these residues increasing more than 8 fold upon SIRT3 knock out[93,94,124]. However, cross-linked sites in the DHE antenna show both decreased levels in aged vs young mitochondria where glutamate respiration is repressed, and increased levels in ADP stimulated mitochondria where glutamate dehydrogenase activity is increased. In addition to the decrease in maximum glutamate/malate stimulated CI respiration, we also observed decreased maximum glutamate only stimulated respiration and lower sensitivity of respiration to glutamate in aged mitochondria compared to young. While not conclusive, these data are also consistent with impaired glutamate metabolism because with only glutamate as a substrate NADH is supplied to the ETS by glutamate dehydrogenase and alpha-ketoglutarate dehydrogenase activity alone. Therefore, these antenna cross-link levels can serve as probes of glutamate dehydrogenase activity in many future studies, including those to help unravel Sirtuin-, diet-, or exercise-mediated lifespan or healthspan extension. For instance, quantitation of DHE3 antenna links prior to age-induced changes in mitochondrial function, with caloric restriction or other interventions can help elucidate pathways that mediate age-related reduction in glutamate respiration.

Quantitative cross-linking revealed changes in protein interactions and conformations affecting many facets of metabolism in aging muscle. Increased ROS production and alterations among mitochondrial ETS complexes are among primary aspects under study to better understand age-related mitochondrial functional decline. ETS complexes, especially CI, require coordinated and controlled assembly to achieve functional maturity[125]. Therefore, altered CI assembly uncovered in the present study should be investigated further to elucidate its role in ETS pathologies in aging. Altered activity and ligand binding in FAO and TCA cycle enzymes can bring to the forefront the contributions of TCA intermediates and fatty acid metabolism to aging phenotypes, connecting phenotypes and molecular remodeling[126-128].

Taken together, these data enable a system-wide view of the changing mitochondrial interactome landscape linking changes in glutamate dehydrogenase activity together with amino acid metabolism, TCA cycle, and energy production by oxidative phosphorylation (**Figure 2.6**). All age-related changes highlighted in this figure involve changes in protein conformations and interactions that are not readily attainable through conventional protein abundance level quantitation. Strikingly, many age-related interactome changes are well-correlated to the severity of aging mitochondrial phenotype, as shown with pairwise CI oxygen consumption ratio compared with the magnitude of changes in protein conformations, interactions and ligand binding (**Figure 2.6**).

In the present manuscript, detailed discussion of only a small subset of cross-links was possible. K-means cluster analysis of all cross-links quantified in at least 2 biological replicates (95% conf. =<1) revealed that cross-links correlating with functional measurements cluster together and non-changing cross-links from these proteins are in a separate cluster together (**Figure 2.6**). Many other cross-links in these proteins display similar patterns to those discussed above with

functional measurements, including proteins from the same pathways, such as ACSL1, CMC1, CPT1B, ATPB, and ATP5F1. The entire interactome dataset with quantitation, structures with mapped cross-links, and k-means clustering assignments is available to view online in XLinkDB[129]. Although this report only covers aging mitochondria in a single sex and single tissue, these data provide a unique, detailed, and quantitative view of mitochondrial aging in muscle that can be used to guide future studies unraveling molecular underpinnings of metabolism changes with age.

2.5 Conclusions and Future Directions

Mitochondrial protein interactomics provides a new tool to identify age-related changes in mitochondria that contribute to functional decline. This tool can now be applied to address many remaining questions including the interaction of age and sex, tissue- or cell-type specific changes such as muscle fiber type shifts, the impact of geroprotective treatments such as elamipretide or exercise training, and the human interactome.

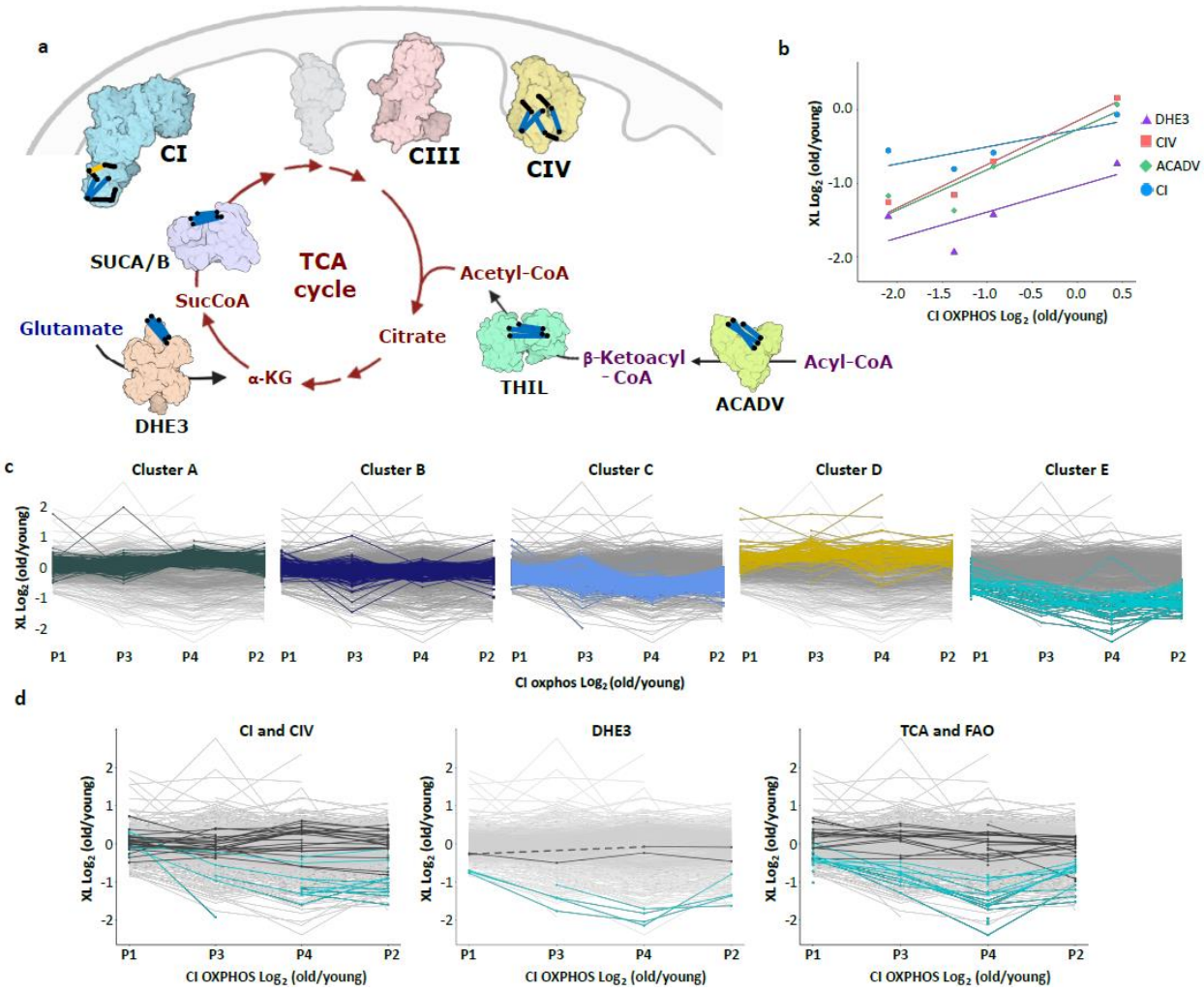

Figure 2.6 Interactome remodeling associated with changes in muscle metabolism with aging. a. Integrated pathways with age-associated changes in protein-protein interactions, protein-ligand interactions, or conformational changes highlighted in this study. b. Correlation between average of $\log_2$ ratios in each biological replicate of cross-links changed with age in DHE3 (purple triangles, $R^2 = 0.58$), CIV (red squares, $R^2 = 0.95$), ACADV (green rhombi, $R^2 = 0.87$), CI (blue circles, $R^2 = 0.63$) and CI driven respiration. c. K-means clustering of cross-links with 5 clusters. CI oxphos $\log_2$ change for P1, P2, P3, and P4 are in increasing order. d. Cross-links with age-related changing levels that are discussed in this study (light blue) cluster together (cluster E); non-changing cross-links from the same proteins are in dark grey.

2.6 METHODS

2.6.1 *Animal Husbandry.*

This study was reviewed and approved by the University of Washington Institutional Animal Care and Use Committee. Female 6-month (n = 4) and 30-month-old (n = 4) C57BL6/J mice were received from the Jackson Laboratory and used to measure CI-, CII-, and CI&CII-linked respiration and cross-linked for mass spectrometry. Further characterization of differences in aging mitochondria to assess top hits from the interactomics results were performed in female young (4-6 month, n=4) and old (27-29 month, n=5) C57BL6/J mice from the National Institute of Aging (NIA) colony. All mice were maintained at 21 °C on a 14/10 light/dark cycle at at 30-70% humidity and given standard mouse chow (LabDiet PicoLab® Rodent Diet 20) and water ad libitum with no deviation prior to or after experimental procedures.

2.6.2 *Mitochondrial Isolation.*

The gastrocnemius muscle was dissected, and mitochondrial isolation was performed by differential centrifugation. The whole muscle was homogenized in Mitochondria Isolation Buffer (210 mM Sucrose, 2 mM EGTA, 40 mM NaCl, 30 mM HEPES, pH 7.4) using a high-speed drill in a glass Dounce homogenizer on ice. The homogenate was centrifuged at 900 x g at 4 °C for 10 minutes. The supernatant was collected and centrifuged at 10,000 x g at 4 °C for 10 minutes. The supernatant was removed, and the mitochondrial pellet was resuspended in ice-cold Respiration Buffer (RB) without taurine or bovine serum albumin (BSA) (1.5 mM EGTA, 3 mM MgCl2-6H2O, 10 mM KH2PO4, 20 mM HEPES, 110 mM Sucrose, 100 mM Mannitol, 60 mM K-MES, pH 7.1). The respiration buffer for mitochondrial resuspension did not include taurine, because it is an aminoethane sulfonic acid which contains a primary amine that could react with the cross-

linker. Isolated mitochondria protein concentration was determined using standard Bradford Assay procedures.

2.6.3 *Mitochondrial Respiration.*

CI, CII, and CI&CII-linked mitochondrial respiration were assayed in mitochondria isolated from young (6-mo-old) and old (30-mo-old) female C57Bl6/J mouse gastrocnemius using an Oxygraph 2K dual respirometer/fluorometer (Oroboros Instruments, Innsbruck, Austria). RB with taurine and BSA was used for respiration measurements (1.5 mM EGTA, 3 mM MgCl2-6H2O, 10 mM KH2PO4, 20 mM HEPES, 110 mM Sucrose, 100 mM Mannitol, 60 mM K-MES, 20 mM taurine, 1 g/L BSA, pH 7.1). Hexokinase clamp (1 U/ml hexokinase, 2.5 mM D-glucose) was used to maintain equilibrium of ATP/ADP at submaximal ADP concentrations[130]. Respirometry and fluorometry reagent stocks were prepared according to Oroboros instructions (bioblast.at). Respiration was measured at 37°C with stirring during substrate and inhibitor titrations.

To measure CI, CII, and CI&CII-linked respiration, first, 10 μM cytochrome c was added to each chamber to allow measurement of respiration in isolated mitochondria without limiting by membrane damage occurring during isolation. Approximately 35 μg mitochondrial homogenate (~8-11 μL) was added to each 2 mL chamber. CI, CII, and CI&CII-linked respiration were measured in parallel for each sample by adding complex-specific substrates and inhibitors and titrating in ADP. CI-linked respiration was measured by adding 10 mM glutamate and 0.5 mM malate. CII-linked respiration was measured by adding 10 mM succinate and 0.5 μM rotenone. CI&CII-linked respiration was measured by adding 10 mM succinate, 10 mM glutamate, and 0.5 mM malate. The OXPHOS capacities for each substrate condition were determined as the maximum oxygen consumption rate (OCR) measured during a titration of ADP from 5-6000 μM

ADP. The background oxygen consumption with de-energized mitochondria was subtracted from all measured functional parameters before reporting final values.

Response to glutamate was measured in mitochondria isolated from young (4-6 month, n=4) and old (27-29 month, n=4) female C57BL6/J gastrocnemius muscles using the Oxygraph 2K dual respirometer/fluorometer. RB with taurine and BSA was used for respiration measurements without hexokinase clamp because saturating ADP concentrations were added to the chambers in a single bolus during the experiment. To measure glutamate sensitivity, a sequential titration of 50 μg mitochondrial protein, 2.5 mM ADP, 10 μM cytochrome c, and sequential additions of 1 mM glutamate up to 10 mM glutamate final concentration were performed.

The mitochondrial respiration results were analyzed using Microsoft Office Excel and GraphPad Prism 9.9 for Mac OS X (GraphPad Software, La Jolla, CA). For all comparisons, $P < 0.05$ was considered statistically significant. Comparisons between two groups were analyzed using unpaired two-tailed student's t-test. Comparisons during ADP or glutamate titrations were analyzed using repeated measures Two-way ANOVA with Sidak's multiple comparisons. titration kinetics were analyzed using nonlinear regression - [Agonist] vs. normalized response variable slope to calculate EC50. Plots depict mean ± standard deviation

2.6.4 *Citrate Synthase Activity Assay.*

CS activity is reportedly a more accurate marker of mitochondrial mass than total protein content when performing comparisons across age[131]. CS activity assay was performed on mitochondrial isolations and used to normalize mitochondrial respiration. CS Activity was measured by spectrometric quantitation (412 nm) of 5,5'dithiobis-2-nitrobenzoic acid conversion to 2-nitro-5-thiobenzoic acid in the presence of Coenzyme A thiol generated during citrate production (CS0720, Sigma) as previously described[132].

2.6.5 *In-gel Complex I and IV activity assays.*

In-gel CI and CIV activity were measured in mitochondria isolated from young (4-6 month, n=4) and old (27-29 month, n=5) female C57BL6/J gastrocnemius muscles as previously described.65 100 μg of isolated mitochondria were loaded in each gel lane. All visible bands for each complex and supercomplex on each gel were quantified In Bio-Rad ImageLab (Version 6.1 for OS X). The background was corrected using the pixels immediately outside each lane volume and the same background cut off filter value for all lanes. The volume values for each band were normalized to the CS activity per mg of protein for the sample in each lane. All values were compared by student's t-test or Two-Way ANOVA with Sidak's post hoc test in GraphPad Prism.

2.6.6 *Cross-linking of isolated muscle mitochondria.*

Isolated mitochondria from murine gastrocnemius muscles of 8 mice (4 young and 4 old) were resuspended in cross-linking buffer (170 mM Na2HPO4, pH 8.0) and either reporter heavy (RH) or stump heavy (SH) iqPIR reagent was added;15 final reaction volume was 100 uL and cross-linker concentration was 10 mM. Cross-linking reaction was allowed to proceed for 30 min at room temperature with shaking to form covalent cross-links between proximal lysine residues within and between proteins and protein complexes in intact mitochondria. Cross-linking buffer was then removed by centrifugation and mitochondrial pellets were lysed in 8M urea. Proteins were reduced with TCEP (30 min RT with shaking) and alkylated with IAA (30 min RT with shaking). Protein concentration of each mitochondrial sample was measured with a Bradford assay using Cytation plate reader. Samples were mixed pairwise (one old and one young using equal amount of protein from each sample making 4 biological replicates total. Protein mixtures

were digested with trypsin overnight (1:100 trypsin concentration at 37 C with shaking). Peptides were then acidified with TFA and cleaned using Sep-Pak c18 columns (Waters). Peptides were separated using SCX chromatography (Luna column, Agilent HPLC) into 14 fractions and fractions were pooled together as following: fractions 1 to 5, fractions 6 and 7, fraction 8, fraction 9, fraction10, fractions 11 to 14. Pooled fractions were dried in a SpeedVac and resuspended in ammonium bicarbonate buffer; pH was adjusted to 8.0 with NaOH. Biotinylated cross-linked peptides were captured with monomeric avidin (ThermoFisher Scientific 20228) for 30 min at RT with shaking. The beads were washed with ammonium bicarbonate and peptides were eluted with 0.1% formic acid in 70% ACN, dried down by vacuum centrifugation and resuspended in 20 uL of 0.1% formic acid.

2.6.7 *Mitochondrial isolation from HEK293 cells and treatment with ADP.*

HEK293 cells were grown in DMEM media supplemented with 3.5 mg/L glucose, 10% fetal bovine serum, 1% penicillin and streptomycin to confluency. The plates were washed with PBS, cells detached using EDTA 20 mM, centrifuged and washed twice in MgCl2. Cells were then resuspended in ice-cold mitochondrial isolation buffer (70 mM sucrose, 220 mM D-mannitol, 5 mM MOPS, 1.6 mM carnitine, 1 mM EDTA at pH 7.4) and homogenized in a glass homogenizer. The homogenate was centrifuged at 600 g for 5 min at 4 C. The supernatant was transferred to a 15 mL tube and centrifuged at 8000 g for 10 min at 4 C. The supernatant was then removed, and mitochondrial pellet was resuspended in 5 mL of mitochondrial isolation buffer and centrifuged at 8000 g for 10 min. The mitochondrial pellet was then resuspended in 200 uL of mitochondrial isolation buffer and split into two. ADP was added to one vial to a final concentration of 1.5 mM. Both samples were incubated at RT for 10 min with shaking. Supernatant was then removed by centrifugation and pellets were resuspended in cross-linking

buffer. RH iqPIR cross-linker and ADP was added to ADP treated sample to final concentrations of 10 and 1.5 mM respectively. SH iqPIR cross-linker was added to control sample to a final concentration of 10 mM. The cross-linking reaction was allowed to proceed for 30 min at RT with shaking. The supernatant was then removed by centrifugation and mitochondrial pellets were lysed, reduced, alkylated, combined, digested, and processed for mass spectrometric analysis the same way as murine muscle mitochondria.

2.6.8 *Mass Spectrometry and data analysis.*

Four uL of each pooled fraction was loaded on a 60 cm C8 heated column and separated on 2 hour gradient on nanoAcquity HPLC system (Waters) and analyzed with QExactive Plus mass spectrometer (ThermoFisher Scientific). Thermo Scientific Xcalibur software (4.2.28.14) was used for MS data acquisition. MS1 scans were analyzed at 70K resolution with AGC target 1e6, and maximum ion time 100 ms. Top 5 peaks with charge 4 or greater were selected for HCD fragmentation with NCE 30 and MS2 spectra were collected at 70K resolution, 5e4 AGC target, and 300 ms maximum ion time.

Raw files were converted to mzXML, and spectra containing cross-linked peptides were determined with Mango software[46]. These spectra were then searched against mouse Mitocarta 2.0 database using Comet search engine[47] and cross-linked peptides were validated with XLinkProphet[48]. Identified cross-links were quantified using iqPIR algorithm and results were uploaded to XLinkDB database. Normalized $\log_2$ ratios and associated p-values based on the Student's t-test on each quantified ion for every cross-link (t = sqrt(df*mean/std) and p-values calculated with the pt function of R: pt(-abs(t), df) where t is the t-statistic and df the degrees of freedom) were downloaded from XLinKDB and correlation plots between biological replicates, density plots for each replicate, volcano plot indicating significantly changed cross-links, box-

plots and t-test comparisons were generated in R using tidyverse package and R markdown is provided[133]. In all boxplots horizontal line represents median, the lower and upper hinges correspond to the first and third quartiles (the 25th and 75th percentiles) and the whiskers extend to the value no further than 1.5 IQR. Pathway enrichment analysis and network of differentially expressed cross-links were generated using STRING web-application. KEGG and GO terms are displayed in the order of strength to describe how large the enrichment effect is. The strength value is the ratio between the number of proteins in the network that are annotated with a term and the number of proteins that is expected to be annotated with this term in a random network of the same size. All displayed terms have FDR corrected p-value less than 0.01.70 Heatmap of all common cross-links was generated for cross-links quantified with 95% confidence (interval within which one can be sure with 95% confidence that the actual mean value resides, calculated as 1.96 * std / sqrt(num_reps) assuming normal distribution) less than 0.5 in all 4 biological replicates. Cross-links were mapped on available structures with either Euclidean distances or SASD distances calculated by Jwalk.71

2.6.9 *Statistics and Reproducibility*

No statistical method was used to predetermine sample size. No data were excluded from the analyses. The experiments were not randomized. The Investigators were not blinded to allocation during experiments and outcome assessment. An F-test was used to test for unequal variances in the respirometry data, but no conditions had significant differences in variance. Normality for XL-MS data is presented in **Figure 2.2**. Variance was not measured in XL-MS as the data analysis was performed by pairing samples. Therefore, the variance cannot be calculated for each population. Welch's t-test was used for comparisons between cross-link population.

SUPPLEMENTAL FOR CHAPTER 2

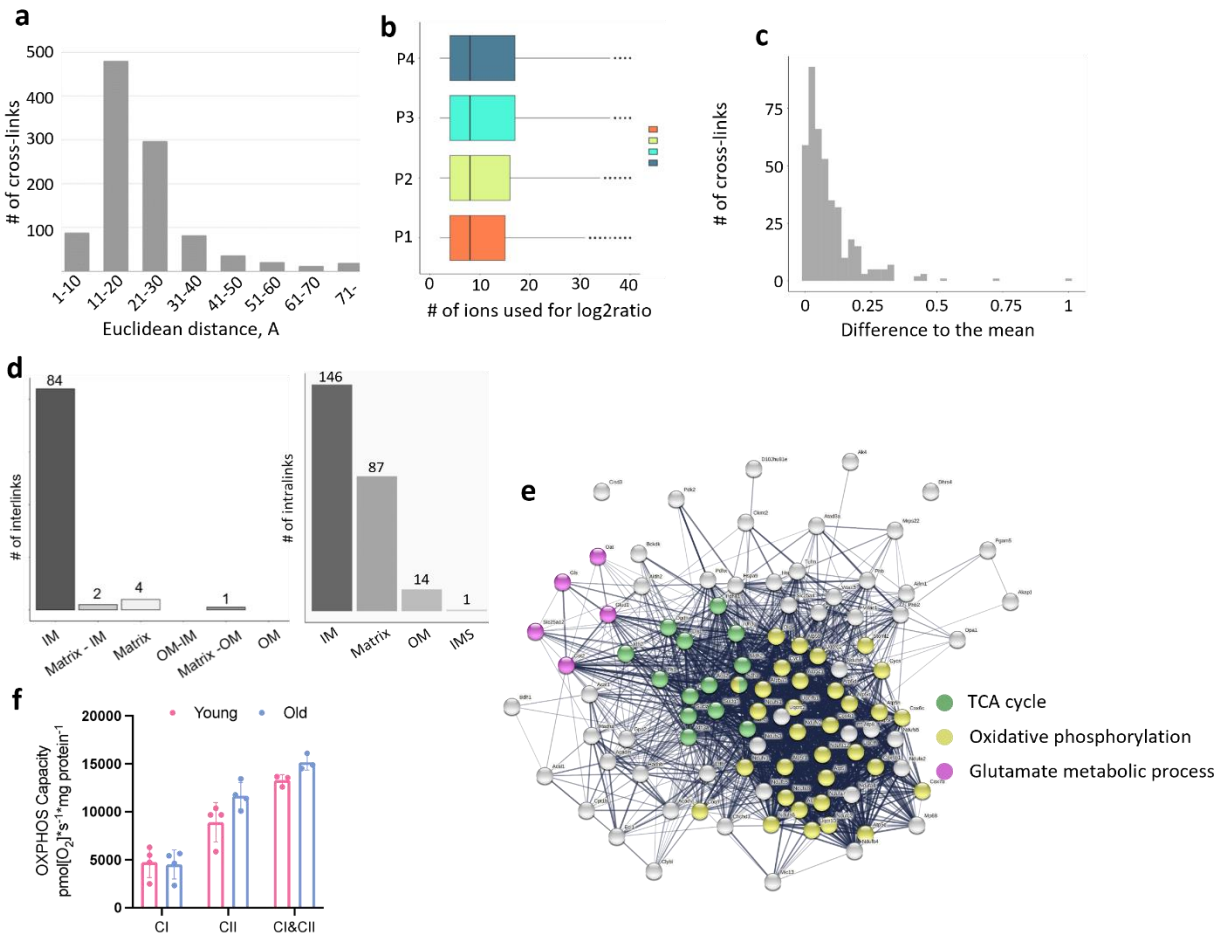

Figure 2.7 Global quantitative cross-linking measurements. a. Histogram of calculated Euclidean distances for all intraprotein cross-links mapped to AlphaFold predicted structures. b. Boxplots of number of ions used for each $\log_2$ ratio in P1, P2, P3, P4. X-axis is capped at 40 for readability but there are ratios in each sample with more than 40 ions. c. Histogram of differences between a mean $\log_2$ ratios for cross-linked residue pairs based on multiple cross-linked peptides (cross-links that connect the same lysines, but can be identified in differently cleaved or modified peptides) and each cross-linked peptide pair d. Submitochondrial localization of significantly changed interlinks (left) and intralinks (right). e. STRING network of proteins with significantly changed cross-links. f. Isolated gastrocnemius mitochondria oxphos capacity normalized by amount of protein from the 4 young (6 months) and 4 old (30 months) female mice. Mean ± SD.

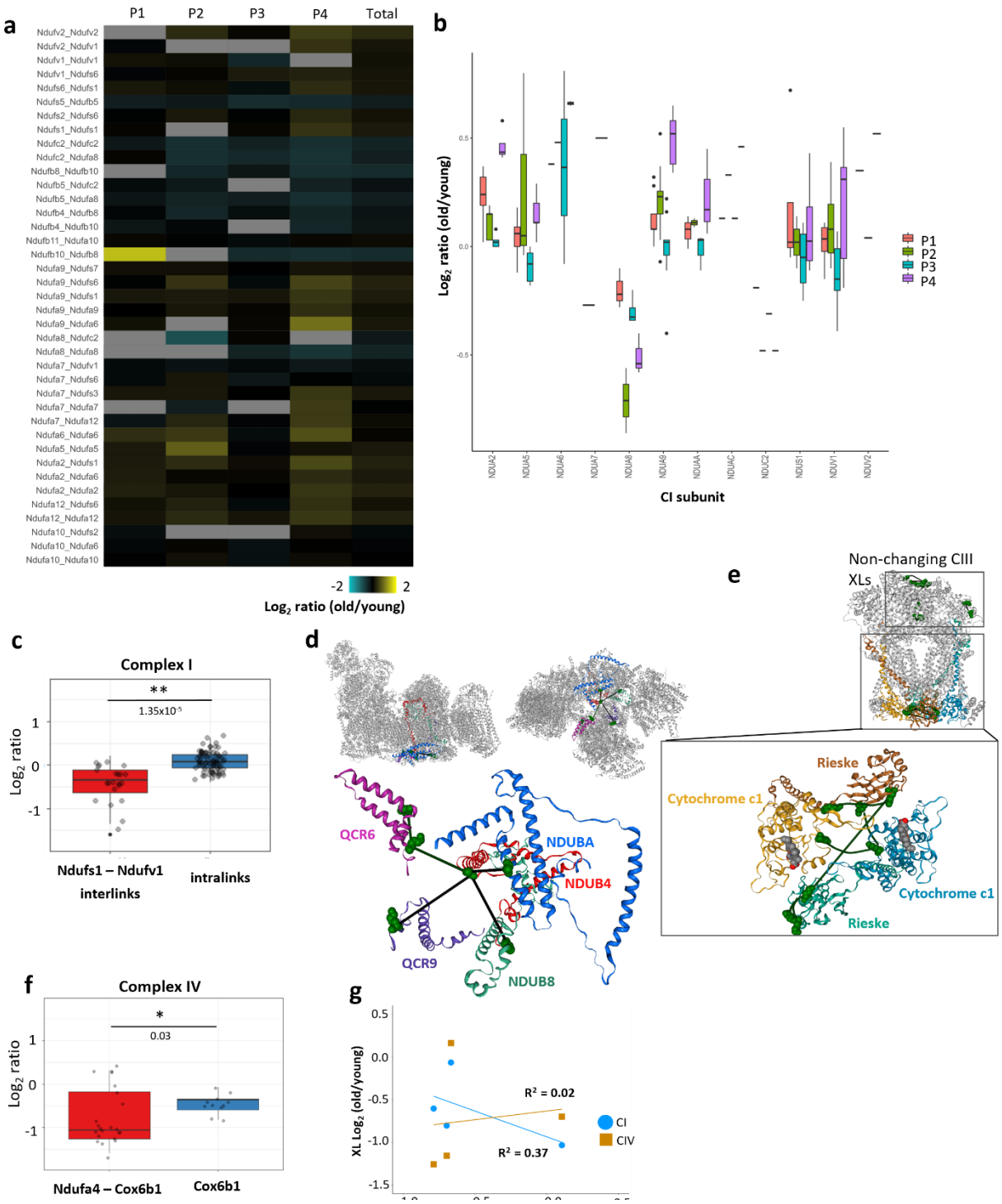

Figure 2.8 Complex I and Complex IV cross-linking analysis. a. Heatmap of $\log_2$ ratios of all NDUS1 and NDUV1 cross-links and interprotein cross-links to other CI subunits. b. Boxplots of all intralinks in CI subunits by a biological replicate. c. Boxplots of crosslinks downregulated in aging and non-changing Intralinks based on all 4 biological replicates for CI (NDUV1XLs n = 34, other links n = 112; visualized as median and 25th and 75th percentiles, with whiskers indicating minima and maxima and CIV (f). Interlinks n = 30, other links n = 14; visualized as median and

25th and 75th percentiles, with whiskers indicating minima and maxima; P-values are from Welch two-sided t-test. Structure of supercomplex (PDB 5GUP) with cross-linked CI and CIII subunits highlighted (top) and specific CI-CIII crosslinks mapped to the subunits (bottom); decreased cross-linked are in green. e. CIII cross-links mapped to a bovine structure. Subunits with decreased intralinks highlighted and zoomed in (right). g. Correlation plots of CI and CIV cross-links changing in aging mitochondria and CII OXPHOS with multiple R-squared displayed.

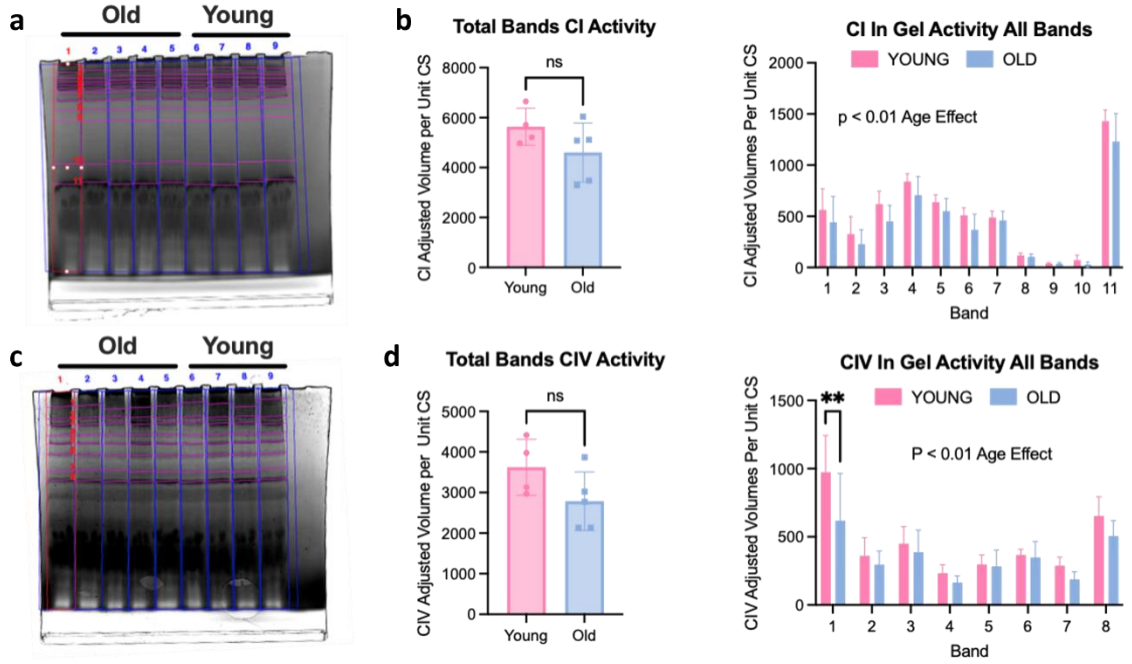

Figure 2.9 Complex I and Complex IV in gel activity measurements show decrease in aged muscle mitochondria. a. In-gel CI activity assay blot with identified bands. b. Quantification of total CI activity (left; statistical significance determined by unpaired two-tailed student's t-test; p=0.1726) and CI activity for each identified band (right; statistical significance determined by Ordinary Two-Way ANOVA with Sidak's post-hoc test; p=0.0011 age main effect). c. In-gel CIV activity assay blot with identified bands. d. Quantification of total CIV activity (left; statistical significance determined by unpaired two-tailed student's t-test; p=0.1219) and CIV activity for each identified band (right; statistical significance determined by Ordinary Two-Way ANOVA with Sidak's post-hoc test; p=0.0045 age main effect; p=0.0059 for Band 1 Sidak's post hoc test). Both activity assays were performed using isolated gastrocnemius mitochondria from young (4-6 month, n=4) and old (27-29 month, n=5) NIA C57BL/6J female mice. Mean ± SD. ns - not significant, **p<0.01 by Sidak's post-hoc test.

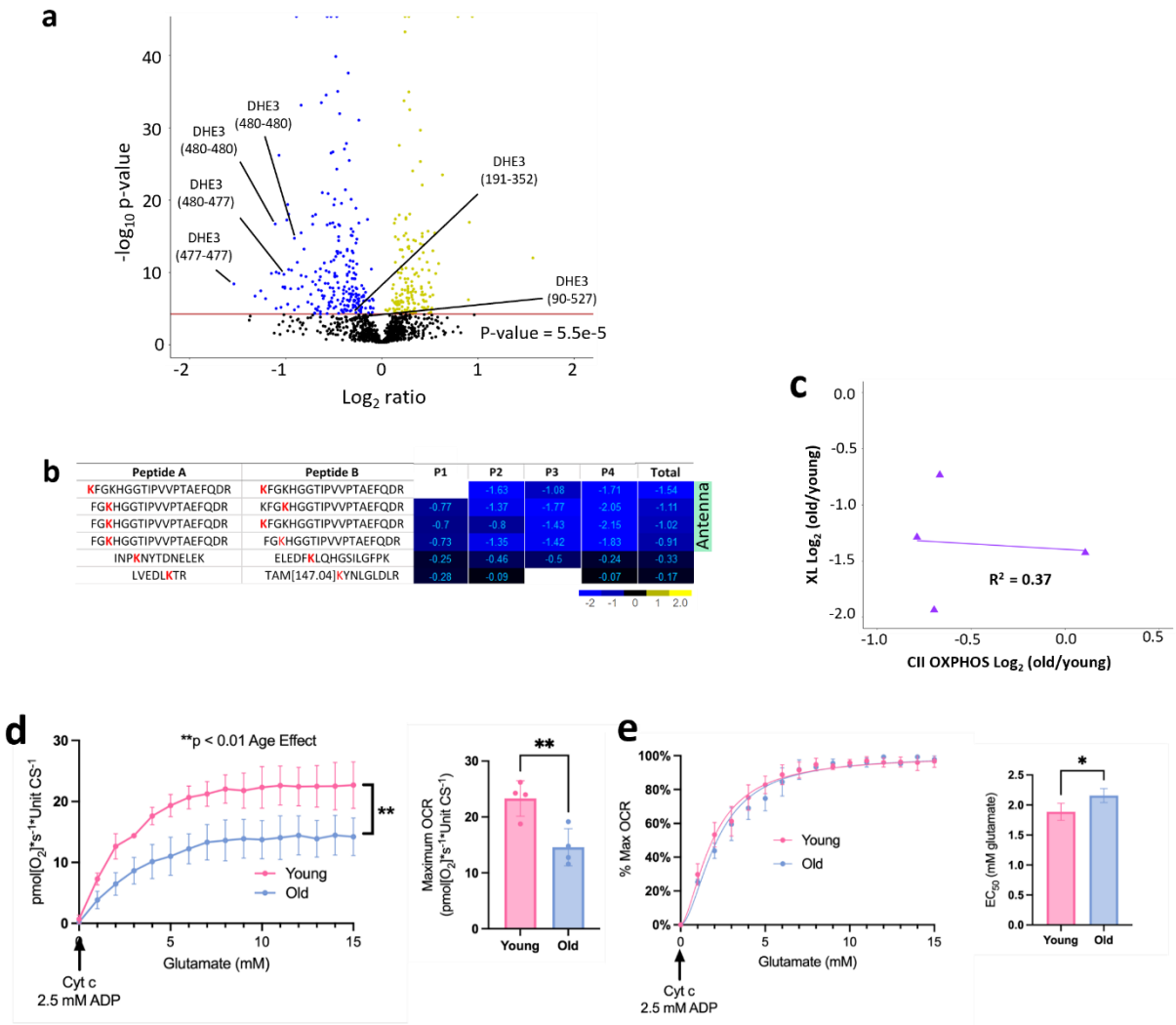

Figure 2.10 Antenna specific DHE3 cross-links decreased with aging. a. Decreased and non-changing cross-link levels in glutamate dehydrogenase highlighted on the volcano plot with Bonferroni corrected p-value=0.05. b. Heatmap of all DHE3 cross-linked peptide pairs with each individual peptide sequence shown. Cross-linked lysine residues are in red. c. Correlation plots of DHE3 antenna cross-links changing in aging mitochondria and CII OXPHOS. e. Normalized glutamate stimulated respiration across a range of glutamate concentrations (left; statistical significance determined by Two-Way RM ANOVA with Sidak's post-hoc test; p=0.0058 age main effect) and maximum respiration capacity with glutamate stimulation (right; statistical significance determined by unpaired two-tailed student's t-test; p=0.0009) in young (4-6 mo, n=4) and old (27-29 mo, n=4) female NIA C57BL/6J isolated gastrocnemius mitochondria. f. The kinetics of glutamate stimulated respiration are altered with age (left; nonlinear regression determined by [Agonist] vs. normalized response -- Variable slope) in young (4-6 mo, n=4) and old (27-29 mo, n=4) female NIA C57BL/6J isolated gastrocnemius mitochondria. The amount of glutamate required to stimulate 50% respiration calculated from the nonlinear regression is increased in old (right; statistical significance determined by unpaired two-tailed student's t-test; p=0.0253). Mean ± SD. *p<0.05, **p<0.01.

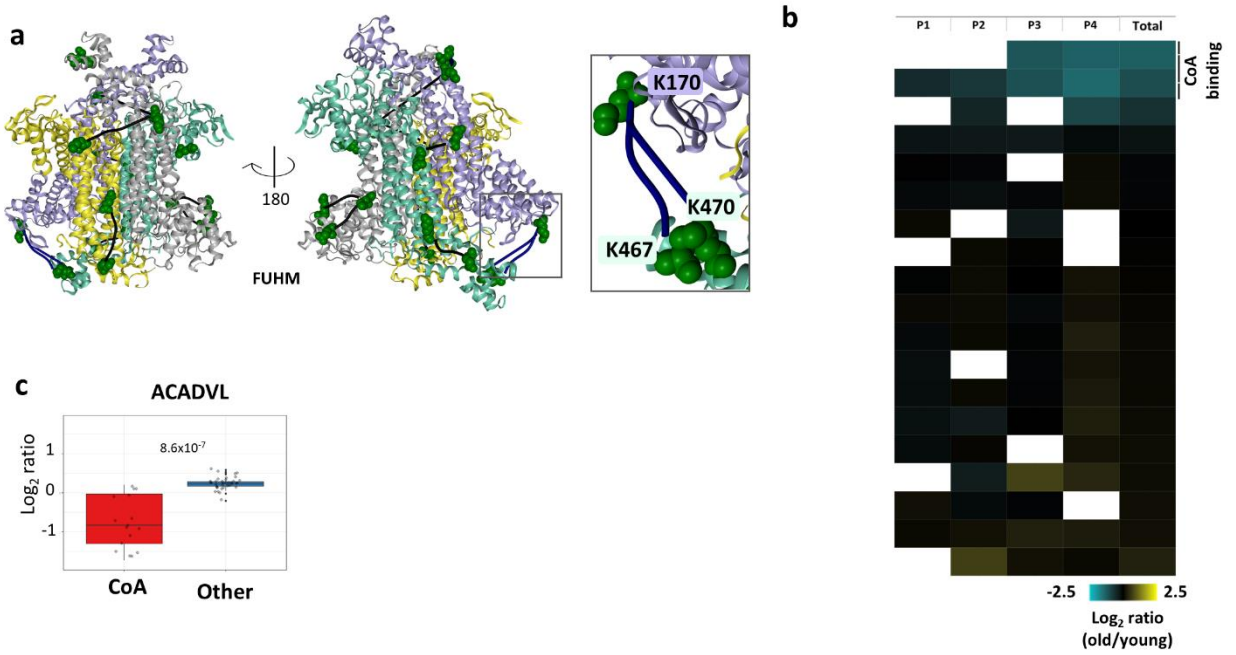

Figure 2.11 TCA cycle and FAO enzymes show decrease in cross-links proximal to CoA binding sites. a. Fumarate hydratase cross-links mapped to a E.Coli structure(PDB 4HGV). Decreased cross-link levels are shown in the zoomed in square. b. Heatmap of $\log_2$ ratios of fumarate hydratase cross-links. c. Boxplots for Acadvl cross-links based on all 4 biological replicates. CoA proximal XLs n = 21, other links n = 46; visualized as median and 25th and 75th percentiles, with whiskers indicating minima and maxima; P-values are from Welch two-sided t-test.

Chapter 3. COMBINING QUANTITATIVE PROTEOMICS AND INTERACTOMICS FOR A DEEPER INSIGHT INTO MOLECULAR DIFFERENCES BETWEEN HUMAN CELL LINES.

3.1 ABSTRACT

Cellular functional pathways have evolved through selection based on fitness benefits conferred through protein intra- and inter-molecular interactions that comprise all protein conformational features and protein-protein interactions, collectively referred to as the interactome. While the

interactome is regulated by proteome levels, it is also regulated independently by, post translational modification, co-factor, and ligand levels, as well as local protein environmental factors, such as osmolyte concentration, pH, ionic strength, temperature and others. In modern biomedical research, cultivatable cell lines have become an indispensable tool, with selection of optimal cell lines that exhibit specific functional profiles being critical for success in many cases. While it is clear that cell lines derived from different cell types have differential proteome levels, increased understanding of large-scale functional differences requires additional information beyond abundance level measurements, including how protein conformations and interactions are altered in certain cell types to shape functional landscapes. Here we employed quantitative in vivo protein cross-linking coupled to mass spectrometry to probe large-scale protein conformational and interaction changes among three commonly employed human cell lines, HEK293, MCF-7 and HeLa cells. Isobaric quantitative Protein Interaction Reporter (iqPIR) technologies were used to obtain quantitative values for thousands of cross-linked lysine residues across three cell lines. This data illustrated highly reproducible (R^2 values of 0.8 for all biological replicates) quantitative interactome levels across multiple biological replicates. We also measured protein abundance levels in these cells using data independent acquisition quantitative proteomics methods. Combining quantitative interactome and proteomics information allowed visualization of cell type-specific interactome changes mediated by proteome level adaptations as well as independently regulated interactome changes to gain deeper insight into possible drivers of these changes. Among the biggest detected alterations in protein interactions and conformations are changes in RNA-binding proteins, chromatin remodeling complexes, mitochondrial proteins and glyoxolase system. Overall, these data demonstrate the utility and reproducibility of quantitative cross-linking to study systems-level

interactome variations. Moreover, these results illustrate how combined quantitative interactomics and proteomics can provide unique insight on cellular functional landscapes.

3.2 INTRODUCTION

Human cell lines are widely used as model systems for biological research. Because these cell lines are originally derived from human tissues, the physiological and molecular alterations of these cells in response to environmental perturbations, e.g., drug treatment, are often considered a proxy to what happens in more complex living systems. Human cell lines have been used for vaccine and antibody production, drug discovery, studies on drug metabolism and cytotoxicity, and synthesis of biological compounds[134]. Furthermore, the information provided by biological studies using cell lines as a model is key to understand the molecular mechanisms of human diseases. Among the most commonly used human cell lines are the cervical cancer cell line HeLa, breast cancer MCF-7, and immortalized embryonic kidney HEK293. Albeit originating from the same species, these cell lines present cell-specific differences on the molecular level, including varying protein abundance levels[135], different protein-protein interactions (PPIs)[17] , conformations, and function. These cellular alterations need to be considered when selecting the best model for a study. To date, some studies have applied mass spectrometry (MS)-based proteomics to compare the protein content of human cell lines and pinpoint differences in the proteomic profiles among them[135-137]. However, protein abundance levels constitute only one of many regulators of the functional landscape that exists within cells. Large scale profiling by affinity-purification MS (AP-MS) has revealed extensive customization of the PPIs across different cell lines[17]. However, large-scale AP-MS requires genetic alteration of cells to exogenously express affinity tagged bait proteins of interest, which can alter the native cellular environment and interactions of some proteins. Moreover, little or no structural information is

gained on protein interactions and conformations from most AP-MS studies. Co-fractionation coupled to mass spectrometry is another method to study protein complexes and how they vary between different cells[138]. Unlike AP-MS it does not require engineering of a tag to a specific protein but similarly to AP-MS it lacks any structural information on direct interaction within the complexes and in individual proteins. On the other hand, chemical cross-linking of proteins coupled to mass spectrometry (XL-MS) is an emerging tool to study protein structures and the interactome[40,139,140]. XL-MS is based on the reactivity of cross-linker groups toward specific side chains of proteins, usually primary amines. The distance between these reactive groups serves as a physical constraint that requires cross-linked sites exist proximal to one another and is useful for modeling protein structures and protein complex topologies[140]. While the structural information gained by XL-MS is lower resolution than traditional structural biology techniques such as X-ray crystallography and cryo-EM, the information derived from XL-MS is highly complementary[40,141] and can be combined with AlphaFold2 to advance large-scale protein-protein structure predictions[142]. Furthermore, XL-MS is applicable to intact living cells and tissues devoid of any genetic alteration, thereby providing structural insight on proteins and complexes in their native environments.

When applied quantitatively (qXL-MS)[55] offers unique insight on protein conformational and protein-protein interaction changes inside cells[69] and even in animal phenotypic comparisons[102,143]. The direct quantitation of each specific pair of lysine residues cross-linked under different conditions allows large-scale visualization of changes in molecular interactions within complex systems not possible by any other means. Combining qXL-MS data with traditional quantitative proteomics methods to obtain information about changes in protein abundances promotes deeper understanding of the regulators that drive functional changes inside

living systems. Here, we applied in vivo XL-MS using quantitative isobaric Protein Interaction Reporter (iqPIR)[63] technologies to perform a comparison of three commonly used human cell lines: HEK293, MCF-7, and HeLa. This study enabled pairwise comparison of HEK293 with HeLa and MCF-7 with HeLa (**Figure 3.1**). The iqPIR strategy allows mixing equal total protein amounts from compared samples before proteolytic digestion, decreasing variability due to subsequent sample processing. These efforts reveal the first large-scale changes in protein conformations and interactions that relate to functional changes among the three commonly studied human cell lines. The qXL-MS results also demonstrate that quantitation values from iqPIR are highly reproducible with all biological replicates and changes as low as 0.5 on a $\log_2$ scale can be detected with statistical significance. Highlighted proteins with changing cross-link ratios in different cell lines include keratins, RNA-binding proteins, chromatin remodelers, proteins involved in clearance of cytotoxic metabolites and mitochondrial proteins. Leveraging quantitative proteomics enables proposal of possible drivers of the change in the cross-link levels.

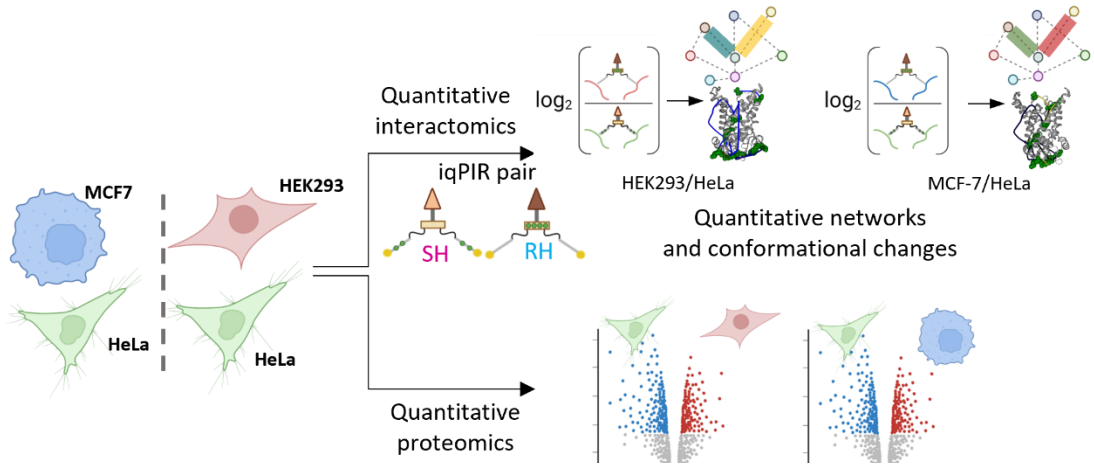

Figure 3.1 Workflow to combine DIA based quantitative proteomics and iqPIR based quantitative interactomics.

3.3 Results and Discussion

Quantitative cross-linking experiments resulted in the identification of 1797 cross-linked peptides across two biological replicate comparisons of HeLa and MCF-7 (MCF-7/HeLa), and 2361 cross-links across 4 biological replicate comparisons of HEK293 and HeLa (HEK293/HeLa). The complete cross-linking information is made available at Supplementary Table 1 and online on XLinkDB at http://xlinkdb.gs.washington.edu/xlinkdb/PHP_SAVED_VIEWS/anna/HEK293_HeLa_and_MCF7_HeLa_iqPIR_cell_lines_interactomics.php. After imposing quality filters for each quantitative value (95% confidence < 0.5 and at least 4 ions used for calculation of $\log_2$ ratio) there are 982, 851, 1020, 1158 and 878, 853 high confidence quantitative values in HEK293/HeLa and MCF-7/HeLa, respectively (**Figure 3.2**.A). The distribution of cross-linked peptide $\log_2$ ratios appears normal, with the large portion of cross-link levels not changing between the cell lines (**Figure 3.2**.B). It should be emphasized that all interactome quantitative values are derived from cross-linked product levels produced inside live cells prior to any protein extraction. Unlike quantitative proteome measurements that derive abundance information based on extracted protein levels, any differences that may or may not occur in protein extraction from one cell sample to the next in iqPIR experiments are accounted for by mixing iqPIR-labled samples with 1:1 total protein amounts and further by centering the iqPIR $\log_2$ ratio distribution to zero if needed (Figure 3.8.A). Thus, iqPIR quantitative interactome data are unique in that the derived ratios are reflective of changes that exist inside cells in terms of the amount of each cross-link level produced prior to lysis and protein extraction. As such, iqPIR ratios are affected by protein, modification, conformational, and interaction levels that exist within the cellular environment and show cell type-specific changes as illustrated for the first time below.

Moreover, the iqPIR method shows great reproducibility across multiple biological replicates, perhaps due to tight regulatory control on the intra-cellular environment where cross-linking reactions are performed. In both HEK293/HeLa and MCF-7/HeLa datasets, high correlation among forward and reverse labeling bioreplicate samples was observed, with correlation R^2 values of 0.91 and 0.88 respectively (**Figure 3.2**.C,D). On the other hand, comparison of quantitative values between a forward replicate of HEK293/HeLa and a forward replicate of MCF-7/HeLa showed much weaker correlation, as expected ($R^2 = 0.01$; Figure 3.8.B). To obtain a single $\log_2$ ratio for each cross-link species in all HEK293/Hela or MCF-7/HeLa data, all ions that provided quantitative information (i.e., released peptides and fragment ions containing cross-linked lysine sites which provided iqPIR isotopic signatures) coming from all biological and technical replicates were combined. Although differential amino acid modifications can affect protein conformations, trypsin cleavage and intra-protein cross-link levels, most cross-linked species involving linkages of the same lysine residues but differing peptide pairs, such as those arising due to trypsin missed cleavage sites and/or methionine oxidation, are anticipated to provide quantitation consistent with fully cleaved, unmodified products that have redundant linkage. The data acquired in these experiments indeed illustrate this to be the case as shown in Figure 3.8.C and provide further increased confidence in iqPIR derived quantitation of cross-linked levels. Allowing a maximum of one missing quantitative value out of four biological replicates resulted in 629 high confidence quantified cross-linked species in the HEK293 to HeLa interactome dataset. Filtering of MCF-7/HeLa interactome data for zero missing values among both biological replicates resulted in 715 high confidence quantified cross-linked species. Application of Student's t-test with Bonferroni multiple testing correction and $\log_2$ ratio greater than 0.5 or less than -0.5 resulted in 285 HEK293 cross-links and 382 MCF-7 cross-links with

log_2 ratios significantly different from HeLa (**Figure 3.2**.E,F). Among all cross-linked peptide pairs, 545 are common among all comparisons (Figure 3.8.D). We then compared protein levels among the cell lines with DIA-Based quantitative proteomics. As expected, proteomes of HEK293, MCF7, and HeLa are quite distinct from each other with many protein levels significantly different between them (Figure 3.8.E-G). Comparison of intra-link levels, where cross-linked peptides originate from the same protein, with protein abundance changes from the proteomics data can reveal cross-linked peptide level changes that are driven by proteome-level changes, and those that are independent of protein-level change. Comparison of high confidence intra-link and relevant protein level changes revealed correlation between intra-link and protein levels (HEK/HeLa $R^2 = 0.52$ and MCF7/HeLa $R^2 = 0.68$, **Figure 3.2**.G), albeit weaker correlation than observed between replicates of interactome datasets. This result is expected since changes in protein levels are likely lead to changes in cross-link levels. Cross-link level changes that differ from protein level changes indicate differences in lysine accessibility, reactivity, or site-to-site relative proximity, such as those due to interaction, modification or conformational differences that may be present in different cell types.

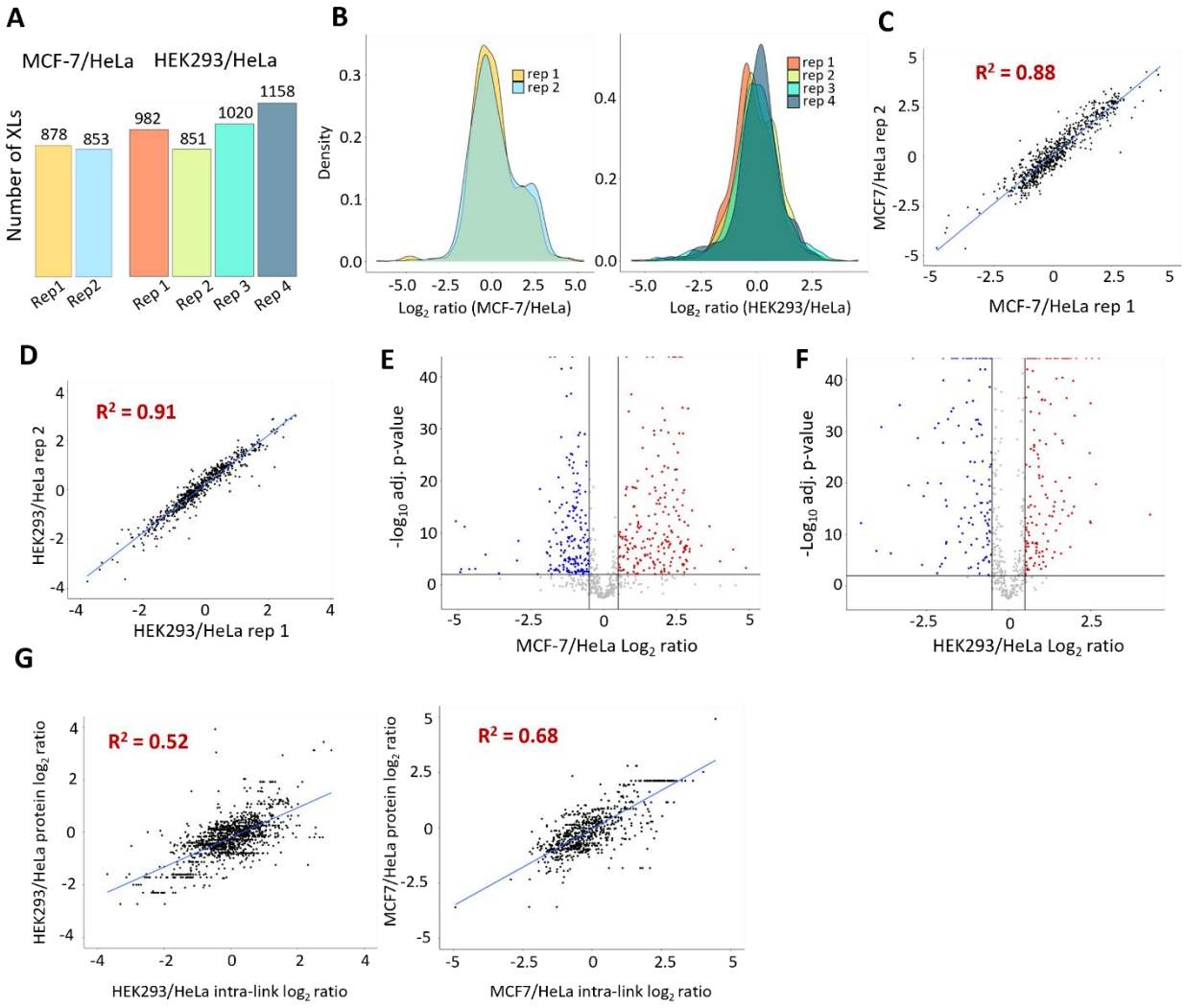

Figure 3.2 Quantitative interactome comparison of cell lines with iqPIR. A. high confidence cross-links quantified in each biological replicate. B. Distribution of $\log_2$ ratios of quantified cross-links in each biological replicate. C. Correlation between biological replicates of MCF7 and HeLa comparison, Pearson's $R^2 = 0.88$. D. Correlation between biological replicates of HEK293 and HeLa comparison, Pearson's $R^2 = 0.91$. Volcano plots with $\log_2$ ratio of crosslinks quantified with 95% confidence <= 0.5 in both biological replicates in MCF7 to HeLa comparison (E) or with 95% confidence <= 0.5 in at least 3 distinct biological replicates in HEK293 and HeLa comparison (F) based on all contributing ions. Bonferroni corrected p-value of 0.05 and |FC| > 0.5 are used to indicate significance. G. Correlation between $\log_2$ ratios for intra-protein cross-links and respective $\log_2$ ratios for proteins based on whole proteome quantitation for HEK293 and HeLa comparison with $R^2 = 0.52$ and MCF7 and HeLa comparison with $R^2 = 0.68$.

3.3.1 *Interactome changes driven by proteome-level changes*

A key advantage of combining quantitative interactome and proteome datasets is the opportunity to further evaluate novel quantitative interactome technologies against more widely established quantitative methods in cases where the changes should be coordinated. Keratins are intermediate filament proteins that form heterodimers of type 1 (keratins 9-28) and type 2 (keratins 1-8 and 71-80) and can be used as a prognostic tool in many types of cancer[144]. Type 2 keratin 8 (K2C8) and type 1 keratin 18 (K1C18) exist as heterodimers and often exhibit protein abundance interdependent upon one another [144,145]. Thus, proteome changes of either protein is expected to be coordinated with level changes of the partner as well as changes in the K2C8-K1C18 interaction levels. In MCF-7/HeLa K2C8 and K1C18 intra-link and inter-link levels are significantly increased (mean $\log_2$ ratio of 2.5) while in HEK293/HeLa interactome data these same link levels are significantly decreased by nearly the same amount (mean $\log_2$ ratio of -2.9) (**Figure 3.3.**A). Previous work in our lab showed that keratin cross-link levels change during the paclitaxel treatment of HeLa cells and are also a hallmark of chemoresistance[51,56]. With paclitaxel treatment[56] as well as in chemoresistant carcinoma cells[51] the cross-link between K1C18 lysine 119 (K119) and K2C8 K130 was observed to be increased in both cases. With iqPIR technologies, multiple ions from both cross-linked peptides provide quantitative information relevant to this interaction. For example, with the K1C18 K119-K130 K2C8 cross-link, we have 66 and 37 measurements of ratios for peptide and fragment ions in MCF-7/HeLa and HEK293/HeLa, respectively (Figure 3.9.A,B). Representative spectra from each interactome analysis, both coming from the experiments where HeLa is cross-linked with reporter heavy (RH) iqPIR cross-linker, so HeLa peptides carry a 2 Da lighter stump than either HEK293 or MCF-7, show remarkable similarity, despite opposite ratio measurements (**Figure 3.3**.B). Interactome

quantitation is done on the MS^2 level after the cross-linker is cleaved from the peptides by decomposing peaks in isotopic envelopes of peptides and their fragments into contributions from RH and stump heavy (SH) cross-linked samples (**Figure 3.3**.B,C, Figure 3.9.B). The iqPIR reporter can in principle also be used for iqPIR quantitation, but because it is the same for all cross-linked species, it can suffer from ratio compression similar to other isobaric quantitative methods[146]. For this reason, iqPIR reporter ion intensities are not included when calculating the cross-linked peptide ratios (Figure 3.9.C). Quantitative proteome-level analyses revealed that K2C8 and K1C18 protein levels are lower in HEK293 and higher in MCF7 compared to HeLa (**Figure 3.3**.D), $\log_2$ fold change of -1.6 (adj. p-value = 0.033) and -2.6 (adj. p-value = 0.002) in HEK293/HeLa and 2.15 (adj. p-value = 0.0095) and 1.18 (adj. p-value = 0.017) in MCF-7/HeLa. These data indicate generally good agreement between interactome and proteome quantitation expected for K2C8-K1C18 and further validate iqPIR quantitative capabilities. We also performed fluorescence imaging of MCF-7, HEK293, and HeLa using anti-keratin antibodies (**Figure 3.3**.E). While not directly quantitative, the images also show the same trend of keratins being more abundant in MCF-7 than in HEK293 cells. Thus, iqPIR data yield expected changes in interactome levels based on measured proteome and immunofluorescence data.

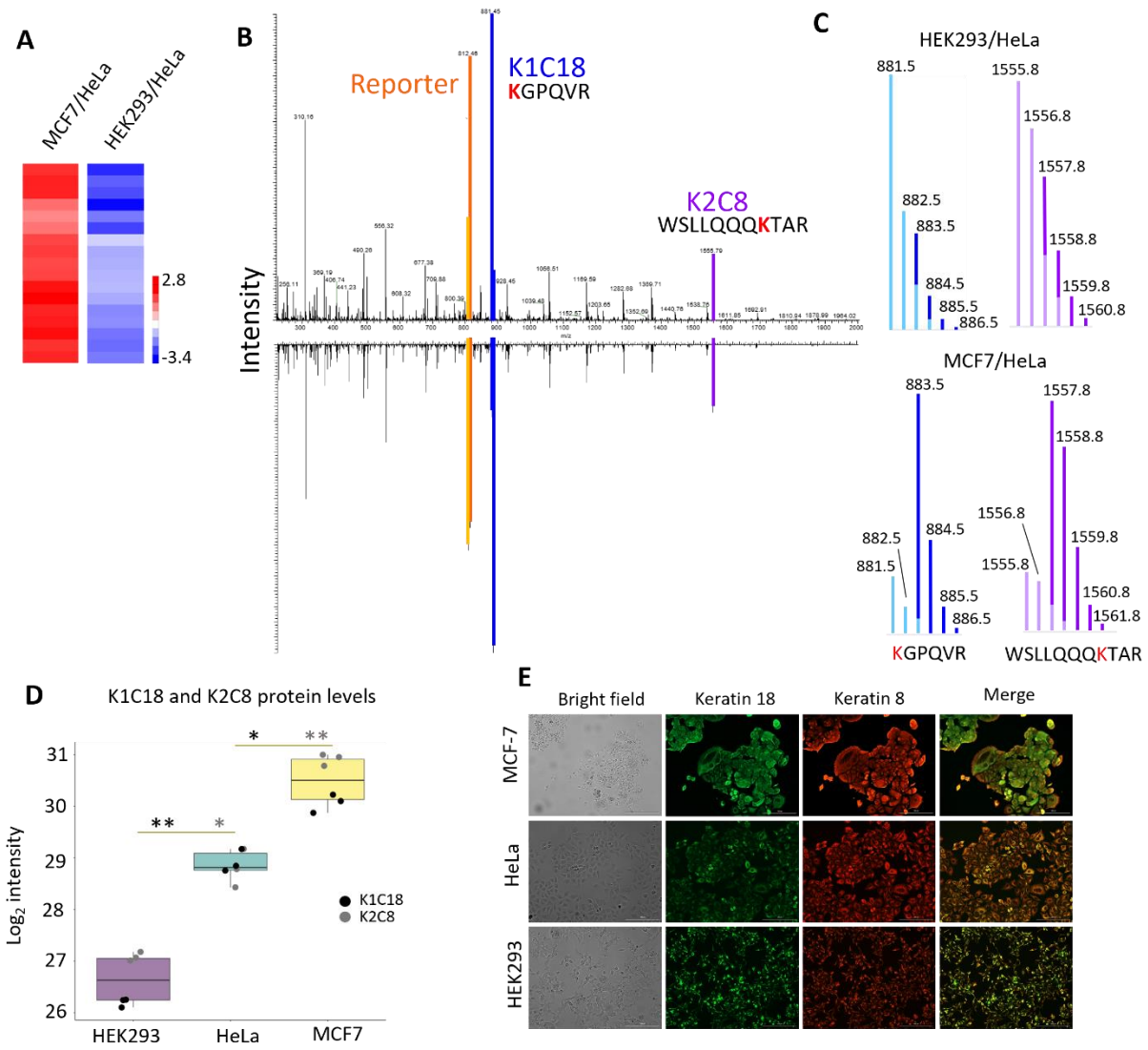

Figure 3.3 Keratins and its interactions are differentially regulated in HEK293 and MCF-7 compared to HeLa cells. A. Heatmap of $\log_2$ ratios of keratin cross-link levels produced in live cells showing that all K2C8 and K1C18 intra- and inter-link levels in HEK293 and MCF-7 cells show opposing changes, relative to link levels in HeLa cells. B. Spectra of a cross-link between K119 on keratin 18 and K130 on keratin 8 in HEK293/HeLa and MCF7/HeLa are displayed as mirror images. Peaks for reporter ions (orange), peptide A (blue), and peptide B (purple) are shown on the original spectra. C. Isotopic envelops with the apportionment from RH and stump SH for peptides A and B show the opposite direction of change in HEK293 cells and MCF7 cells compared to HeLa. In HEK-293 (cross-linked with SH) the crosslink level is decreased relative to HeLa (cross-linked with RH). In MCF7 (crosslinked with SH) the same cross-link shows the opposite change relative to HeLa (cross-linked with RH). In all plots, darker shaded color indicates apportioned intensity from SH sample, and lighter shading indicates RH samples. D. Boxplot of $\log_2$ intensities for keratin 18 and keratin 8 protein in all three cell lines with significance as determined by Student's t-test with multiple testing correction (* = 0.05, ** = 0.01. Each point indicates a value for either K1C18 (black) or K2C8 (grey) in each biological replicate. E. Immunostaining with anti-keratin 18 (green)

and anti-keratin 8 (red) antibodies in all cell lines indicating protein level differences consistent with proteome measurements.

3.3.2 *Quantitative interactomics allows a deeper view of remodeled protein networks*

One of the key advantages of interactome analysis is the potential to reveal molecular details and changes that are not driven by protein abundance level changes that may be difficult to observe otherwise. RNA-binding proteins (RBPs) interact with RNAs to regulate many key cellular processes, e.g., transcription, splicing, mRNA localization, transport, and translation[147]. Heterogeneous nuclear ribonucleoproteins (hnRNPs) are RBPs that contain their own nuclear localization signal and therefore comprise complexes with RNA primarily within the nucleus[148-150] and hnRNPs exist under complex functional regulatory control based on cellular demands. Interactome quantitation revealed large changes in cross-link levels of many hnRNPs in both HEK293/HeLa and MCF-7/HeLa datasets. A total of 61 and 102 cross-links were detected for hnRNPs in MCF-7/HeLa and HEK/HeLa interactome datasets, respectively. A quantitative network that encompasses cross-links from 19 RNA binding proteins was constructed (Figure 3.10.A**)** allowing visualization of cross-linked peptide levels that change in both MCF-7 and HEK293, only one cell comparison, or did not change. Proteome-level analysis of these proteins indicates that some exhibit levels that are changed in HEK and/or MCF-7 relative to HeLa cells and thus, are expected to exhibit altered cross-link levels. (Figure 3.10.B,C). Overall, distributions of protein level $\log_2$ fold changes show that MCF-7/HeLa values are shifted toward negative and HEK293/HeLa are shifted toward positives (**Figure 3.4**.A). A similar trend is observed on cross-link level, although with a more pronounced shift, suggesting that even greater remodeling happens on interactome level.

Among the proteins exhibiting cross-link level changes that differ from protein level changes are HNRPC (similar protein levels in all three cell lines) and ROA1 (HNRPA1) that exhibits similar

protein levels in HEK293 and HeLa, but is repressed in MCF-7 cells (**Figure 3.4**.B). HNRPC is involved in binding pre-mRNA and has a role in splicing by binding regulatory untranslated regions[151]. ROA1 is involved in RNA packaging into an array of ribonucleosomes[151] and has been found to be antagonistic toward exon usage in splicing[152]. Previous mass spectrometry studies identified peptides indicating both HNRPC and ROA1 may be components in isolated nuclear spliceosomal B and C complexes[153] although neither protein has yet been structurally characterized within resolved spliceosome complexes. The majority of HNRPC intralinks are increased in HEK293 and decreased in MCF-7, when compared to HeLa cells (**Figure 3.4**.C). The links are mapped to an SFPQ structure as previously described as there is no solved HNRPC structure[154]. Other HNRPC intra-link levels were observed with levels that were unaltered in either interactome dataset, which is expected for and consistent with unaltered HNRPC protein levels. Combining these results with observed unaltered protein levels indicates that the altered HNRPC cross-link levels reflect molecular changes due to site accessibility, reactivity, or relative site-site proximity inside these cells not driven by differential protein abundance levels. These observations must therefore arise due to differential changes in modifications, conformations, and/or molecular interactions of HNRPC within these three cell lines. Moreover, inter-protein cross-links between HNRPC and ROA1 were also observed with altered levels in these interactome comparisons (Figure 3.10.A). While all HNRPC-ROA1 inter-link levels decreased in MCF-7/HeLa data ($\log_2$ ratios of -1.79 and -1.84), these same links were observed with significant increase ($\log_2$ ratios 0.3 and 1.1) in the HEK/HeLa interactome. Protein levels of ROA1 decreased in the MCF7/HeLa proteome and thus, likely contribute to and may explain the decreased levels of ROA1 intra- and inter-link levels (**Figure 3.4**.D). However, neither HNRPC nor ROA1 protein levels changed significantly in the HEK/HeLa proteome comparison. Therefore, other molecular differences as

discussed above must give rise to increased HNRPC-ROA1 inter-linked levels in HEK/HeLa cell interactome changes. Interestingly, all HNRPC-ROA1 inter-linked peptides and all interlinks between ROA1 and all other hnRNPs other than ROA2 involve the single ROA1 lysine K350 (Figure 3.10.A). This residue falls within the nuclear targeting sequence M9 (residues 320-357), involved in the transport and localization of mRNAs[155]. The role of K350 in hnRNPs conformation and protein-protein interactions has been previously observed[154]. The present quantitative interactome data indicate that ROA1 M9 involvement in mRNA nuclear shuttling is different in HEK compared to HeLa cells in ways that are not regulated through ROA1 protein levels.

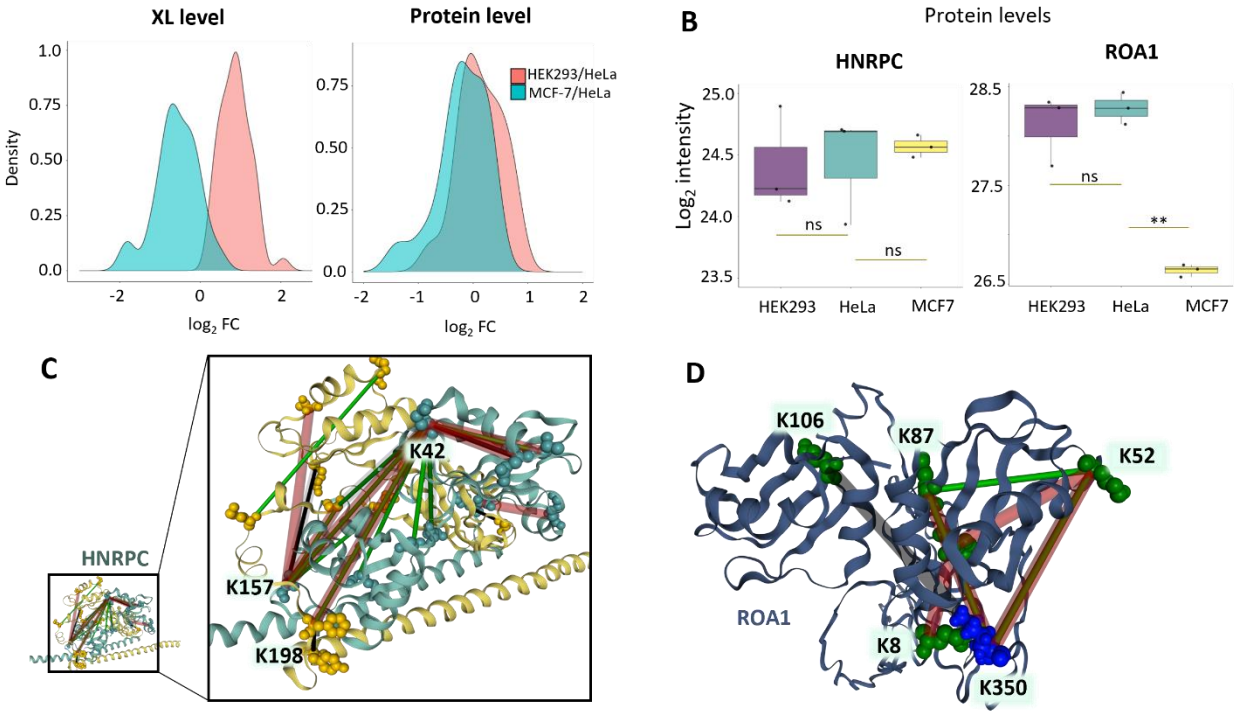

Figure 3.4 Proteome and interactome level remodeling of RNA binding proteins. **A.** Distributions of average log2 ratios of RNA binding proteins on a cross-link level (left) and protein level (right). **B.** Boxplots of log_2 intensities of HNRPC and ROA1 protein levels in all three cell lines with significance as determined by Student's t-test with multiple testing correction (** = 0.01, ns = non-significant). **C**. Cross-links for hnRNPC, mapped to the SFPQ crystal structure (PDB 4WIJ). Cross-links from HEK293/HeLa and MCF-7/HeLa are indicated with thick transparent lines and thin solid lines, respectively. The log_2 ratio intensities are represented in green for decreasing ratios compared to control, in red for increasing ratios, or black for non-changing ratios. **D.** Cross-linked peptides for ROA1 mapped to a previously described modeled structure[154]. Lysine K350, indicated in blue, is part of the nuclear targeting sequence M9.

3.3.3 *Chromatin remodeling complexes and their interaction with nucleosomes is altered between HEK293 and HeLa*

Epigenetic landscape and chromatin remodeling has been shown to play an important role in cancer onset and progression[156]. There are several important families of chromatin remodelers that have been characterized extensively. One of them is ISWI family, first discovered in drosophila[157]. A characteristic feature of a catalytic subunit of SIWI remodelers is SANT domain[158]. This domain, together with neighboring SLIDE domain, is responsible for nucleosome recognition. We have identified and quantified a cross-link (K847-K855) that spans SA1 helix of the SANT domain of SMCA5, a human ISWI catalytic subunit encoded by SMARCA5 gene (**Figure 3.5**.A, Figure 3.11.A). In HEK293/HeLa, this cross-link is increased, while it is unchanged in MCF7/HeLa. There are also no protein level differences between any of the cell lines; therefore, it is unlikely that changes in HEK293/HeLa are caused by protein abundances (**Figure 3.5**.B). We have mapped this cross-link on a structure of SANT domain of *D. Melanogaster* homologue of SMCA5, ISWI (**Figure 3.5**.C), but there is no solved structure of SMCA5 that contains SANT domain. Recently, a structure of *S. Cerevisiae* ISW1a complexed with two nucleosomes have been solved[159]. The sequence of yeast ISW1a is substantially divergent from fly ISWI (and human SMCA5), but structurally their SANT domains are similar (Figure 3.11.B). Mapping cross-linked residues on this structure shows that cross-link would be right at the contact with DNA connecting two nucleosomes (**Figure 3.5**.C). Together with non-changing protein levels we can hypothesize that increase in the cross-link is caused by the decreased interaction with DNA and nucleosomes in HEK293 cell line. Chromatin accessibility and transcriptional machinery differences between the human cell lines have been reported before[160] and present work illustrates how quantitative interactomics can help in their investigation.

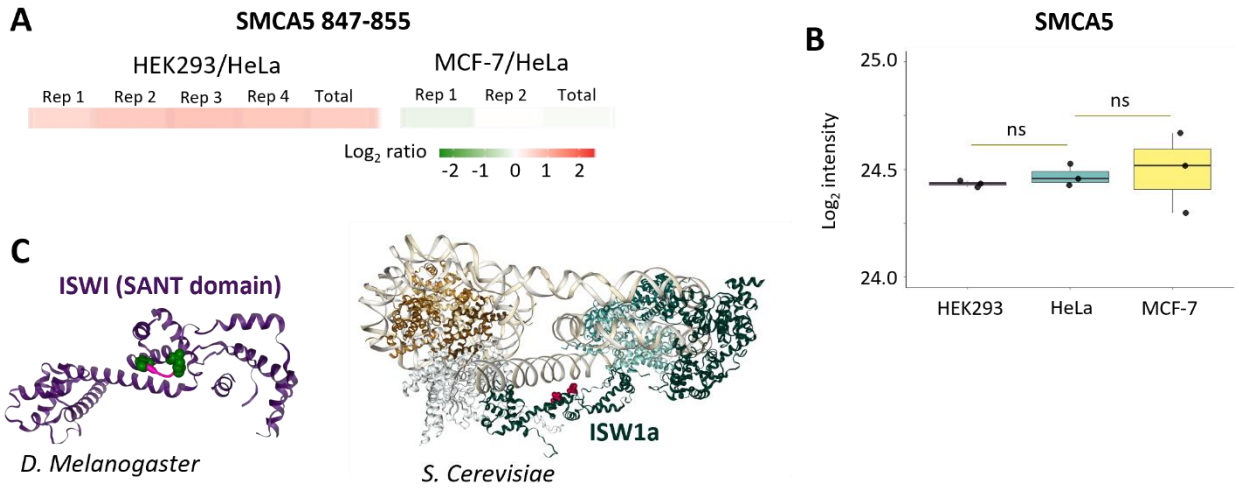

Figure 3.5 Chromatin remodeling complexes interaction with nucleosome is different in HEK293 compared to HeLa. **A.** Heatmap of $\log_2$ ratio of SMCA5 K847-K855 intralink. **B**. Boxplot of SMCA5 $\log_2$ intensities in HEK293, MCF7 and HeLa with significance as determined by Student's t-test with multiple testing correction (ns = non-significant). **C**. SMCA5 cross-link mapped to the structure of fly SANT domain (PDB:1OFC) (left) and cross-linked residues (magenta) mapped on the structure of yeast ISWE1a complexed with dinucleosomes (PDB:7X3T) (right).

3.3.4 *Clearance of cytotoxic glycolytic byproduct is impaired in MCF-7 cells compared to HeLa*

LGUL, protein glyoxalase 1 encoded by GLO1 gene, is a part of a system responsible for detoxification of cytotoxic compound methylglyoxal (MG)[161]. MG is a highly reactive byproduct of glycolysis and a precursor of glycation end-products, associated with multiple pathologies [162]. Switch to glycolytic phenotype is one of the main features of most cancers that results in accumulation of cytotoxic MG [163,164]. Overall, overexpression or increased activity of LGUL has been reported in many cancers and is associated with poor prognosis[164,165]. We have quantified K147-K158 cross-link with multiple peptides resulting from miscleavages and methionine oxidation in both HEK293/HeLa and MCF-7/HeLa datasets (**Figure 3.6**.A). Increase in this cross-link in HEK293 cells appears to be driven by increased protein levels (**Figure 3.6**.B). Unlike HEK293/HeLa though, in MCF-7/HeLa this cross-link changes in the opposite direction:

cross-link level is decreased while protein levels slightly increase (no statistical significance is reached). Mapping this cross-link on the structure with glutathione (GSH) analogue that act as competitive inhibitor shows that the cross-link spans the GSH binding pocket (**Figure 3.6**.C). Moreover it is proximal to cysteine 139 (C139), which has been reported as a site of S-glutathionylation that has an inhibitory effect on LGUL activity[166]. Both C139 modification and GSH binding could potentially affect the formation of the cross-link. Molecular dynamic simulations have shown that C139 glutathionylation might affect flexible loop where K157, involved in the cross-link discussed here, is located[166]. Overall, this data indicates that there is a possible difference in LGUL activity between HeLa and MCF7 cells that is not driven by protein levels.

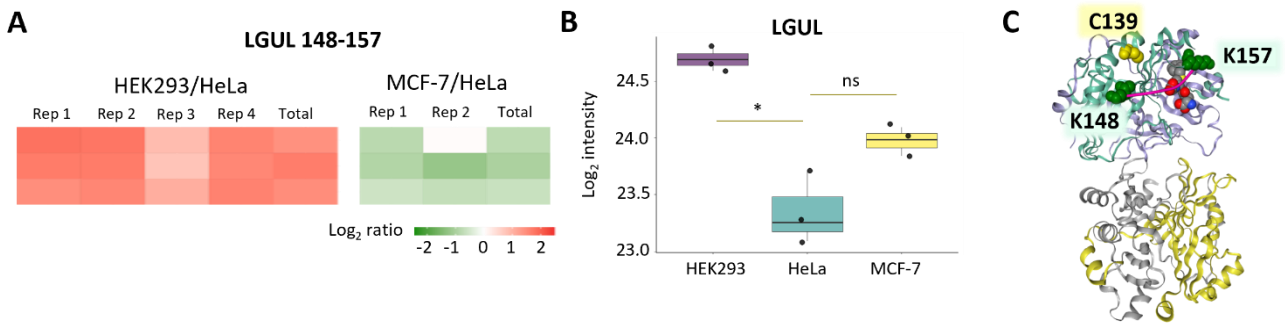

Figure 3.6 Glyoxolase 1 (LGUL) cross-link at the regulatory site is decreased in MCF-7/HeLa **. A.** Heatmap of log_2 ratios of LGUL K148-K157 cross-links in Hek293/HeLa and MCF-7/HeLa. **B.** Boxplot of LGUL log_2 protein intensities in HEK293, MCF-7 and HeLa with significance as determined by Student's t-test with multiple testing correction (* = 0.05, ns = non-significant). **C.** LGUL 148-157 cross-link mapped to a human structure with an S-benzyl-glutathione inhibitor (located between cross-linked residues) (1FRO). Cysteine modified by inhibitory glutathionylation is indicated in yellow.

3.3.5 *Integration of Quantitative Cross-Linking with Proteomic Analysis Reveals Dynamic Functional States of Adenine Nucleotide Translocase Isoforms*

Adenine nucleotide translocase (ADT) is in inner mitochondrial membrane channel responsible from transporting ADP inside and ATP outside of mitochondria[167]. We have quantified cross-links

from 2 out of 4 human isoforms, ADT2 and ADT3. In MCF7/HeLa we observe increase in ADT2/3 cross-links between K147 and K272 or K33 (**Figure 3.7**.A). As for protein levels, there is no change in the levels of ADT2 and a decrease in ADT3 in MCF7 compared to HeLa (**Figure 3.7**.B). To further investigate the functional change in ADT proteins that could be associated with these cross-links we performed iqPIR experiments on the isolated mitochondria treated with two different ADT inhibitors. We have chosen mouse cell line c2c12 due to its high mitochondrial content and ANT expression and high homology between human and mouse ADT proteins (Figure 3.11.C). Bongkrekic acid (BKA) locks ADT in its matrix open state or m-state while carboxyatractyloside (CATR) locks it in cytosol open state or c-state[167,168]. K147-K33 link when mapped on a c-state structure (PDB 1OKC and 2C3E) shows SASD more than 99 Å, indicating that this link is not likely to be formed while ADT is in c-state (**Figure 3.7**.C). In agreement with this prediction, K147-K33 link increases with BKA treatment and decreases with CATR (**Figure 3.7**.D). SASD for K147-K272 link when it is mapped on either BKA locked ADT structure (6GCI) or CATR structure (2C3E) shows plausible distances (38 and 34 Å respectively). So, it would not be possible to predict if this link is associated with m-state or c-state. But this cross-link follows the same pattern with BKA and CATR treatment of isolated mitochondria as K147-K33 cross-link. So, it is also an indicator of increased m-state. Interestingly, for ADT3, 147-272 cross-link shows a very small increase. But when we take into account decreased protein levels of ADT3 in MCF7, K147-K272 in ADT3 actually increases relative to protein levels, indicating increased levels of ADT3 m-state just like ADT2. In HEK293, protein levels for both ADT2 and ADT3 decrease relative to HeLa (**Figure 3.7**.A). The only cross-links that are different from protein levels are K147-K63 in both ADT2 and ADT3 and K147-K147 ADT2 dimer link. K147-K63 increases in both BKA and CATR treated mitochondria. So, it is unlikely to be associated with a particular

state but might be an indicator of general lower activity of ADT. The importance of ADT and its conformational states in relations to tumorigenesis and chemotherapy resistance has been explored before[169,170]. In the future quantitative interactomics and proteomics can help elucidate ADT mechanistic and metabolic role of ADT in cancer pathology.

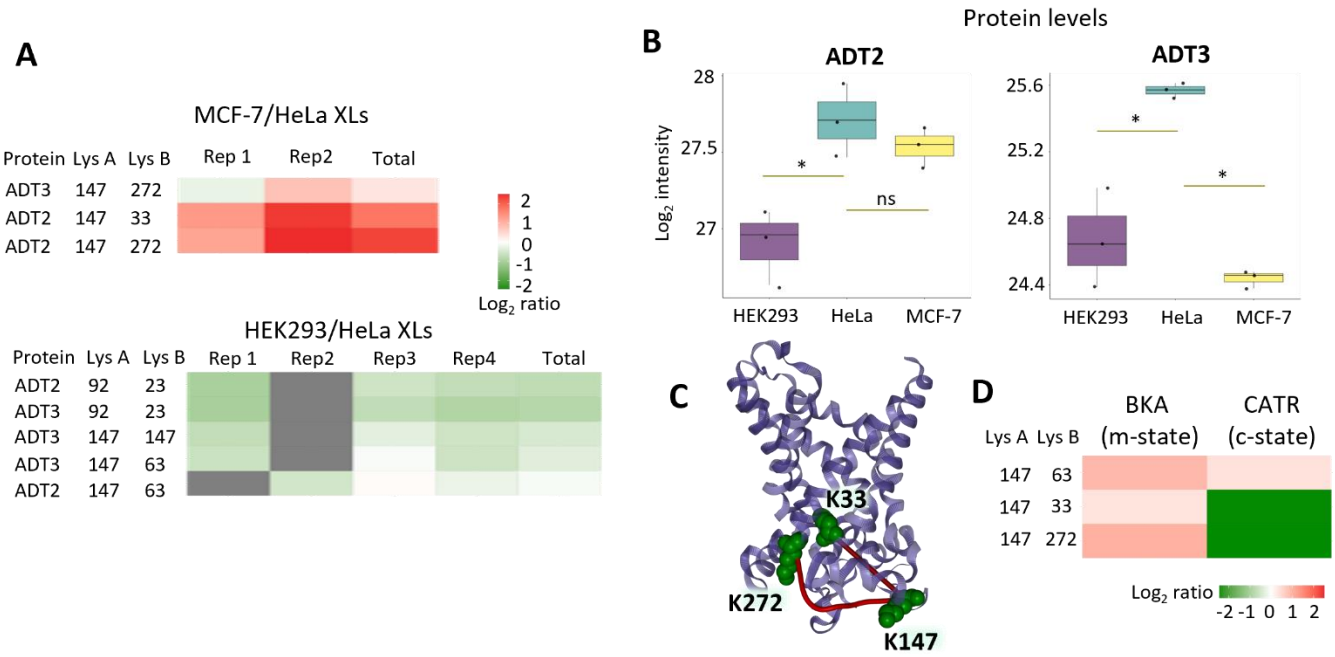

Figure 3.7 Combining quantitative interactomics and proteomics gives deeper insights into molecular differences in human cell lines. **A**. Heatmap of $\log_2$ ratios of ADT2 and ADT3 cross-links for MCF7/HeLa (top) and HEK293/HeLa (bottom). **B.** Boxplot of ADT2 and ADT3 $\log_2$ intensities in HEK293, MCF7, and HeLa with significance as determined by Student's t-test with multiple testing correction (* = 0.05, ns = non-significant). **C**. K147-K272 and K147-K33 cross-links mapped on a c-state structure. K33-K147 cross-link is mapped with Euclidean distance as SASD calculated values exceed 99 Å. **D**. Heatmap of $\log_2$ ratios in c2c12 isolated mitochondria treated with m-state inhibitor (BKA) or c-state inhibitor (CATR).

3.4 Conclusions and Future Directions

Here we have demonstrated the utility of a newly developed method for quantitative assessment of protein interactomes in cells using isobaric quantitative Protein Interaction Reporter Application of iqPIR technologies to compare interactomes of three commonly used human cell lines. These efforts demonstrated surprisingly high reproducibility and robustness of quantitative values that

enable statistical filtering to reveal significant changes among HEK293, MCF-7 and HeLa cellular interactomes. Combining the quantitative cross-linking data together with DIA based quantitative proteomics identified molecular changes inside cells that were driven by and concordant with measured protein abundance level changes. The agreement in keratin cross-link levels produced in cells with measured extracted keratin protein levels demonstrated that the presented interactome approach can produce an accurate assessment of changes from inside cells. More excitingly, additional presented examples illustrate that regulation of protein conformations and protein-protein interactions within cells independent of protein abundance level changes can be uniquely detected in this way. We have detected large scale remodeling of RNA binding proteins between three cell lines that is driven in part by changing protein levels and in part by change in protein-protein interactions and confirmations. Although additional experimentation is required to better interpret these changes, conformational change of HNPRC could be either required for or a consequence of increased interaction with ROA1 that was concurrently increase in HEK cells. Given the roles of both HNRPC and ROA1 in mRNA binding and possibly, spliceosome function, these and other hnRNP interactome changes may be indicative of increased demand for mRNA maturation and shuttling that would be expected based on increased cell growth rates and required protein production. Indeed, our previous efforts to map interactome changes during cell growth with a mitotic inhibitor[56] revealed an inhibitor concentration-dependent decrease in HNRPC-ROA1 K42-K350 and K147-K350 cross-link levels. Similar to our previous discovery that cross-link levels within enzyme complexes can serve as an indicator of in vivo enzymatic activity [143] the present observation of hnRPN interactome changes may provide novel insight on mRNA processing activity within cells.

Chromatin remodeling, glycolytic metabolism and subsequent damage by its byproducts and ADP/ATP translocation between mitochondria and cytoplasm have been extensively studied in the context of cancer[156,164,165,169-172]. Most of the studies though focus on changes in expression as measured by mRNA or protein levels. Here we have demonstrated that quantitative cross-linking allowed us to look deeper in these processes. We were able to detect changes in nucleosome interactions with chromatin remodeling complex ISWI through increase in the cross-link at the site proximal to DNA in HEK293 cells compared to HeLa. Glycolysis, upregulated in almost all cancers, creates byproducts which, if not eliminated by glyoxalase system, lead to cellular damage and eventually apoptosis[173]. In our MCF-7/HeLa comparison we have uncovered a decrease in a cross-link that is at the substrate binding site and close to cysteine with inhibitory glutothionylation, that is not driven by change in protein levels. Looking at just levels of glycolytic enzymes, some of them increasing in MCF-7 and some of them decreasing (Figure 3.11.C), it might be challenging to predict if there is any differences cytotoxic glycolytic byproducts in HeLa or MCF-7 cells. Incorporating quantitative cross-linking data allowed us to pinpoint potential difference in the enzyme PTMs and/or activity. Follow-up studies would be needed to investigate closer the differences in glyoxolase system in different cancer cell lines that are not driven by protein expression levels. Finally, differences in cross-link levels in mitochondrial ADP/ATP translocase 2 and 3 indicate increase in a particular conformational state in MCF-7 cells compared to HeLa. We were able to confirm that particular cross-links correspond to specific states by measuring changes in cross-link levels with state-specific inhibitors in isolated mitochondria. We were also able to reconcile if differing cross-link levels in ADT2 and ADT3 are the result of isoform specific regulation by comparing cross-link level changes to protein level changes. We showed that cross-link changes in the same way relative to protein levels in ADT2 and ADT3 even

though the protein level changes are not the same. Examples presented in the current work are only a small glimpse into the data generated by combining quantitative interactomics with quantitative proteomics. We have made the full interactive dataset available for the community on the XLinkDB website. Overall, we have demonstrated the utility of iqPIR based quantitative cross-linking data in conjunction with quantitative DIA based proteomics for deeper investigation of molecular differences in cell lines. In the future, this approach could be applied to tissues, organelles and other biomedically relevant samples.

3.5 METHODS

3.5.1 *Cell culture and harvesting*

HeLa cells (ATCC CCL-2), HEK-293 cells (ATCC CRL-1573), and MCF-7 breast cancer cells (ATCC HTB-22) were seeded at a density of 5×10^6 cells into 150 mm culture dishes with 20 ml of Dulbecco's modified Eagle medium (DMEM) supplemented with 10% (HeLa and HEK) and 20% (MCF-7) dialyzed fetal bovine serum (Valley Biomedical), and 1% penicillin/streptomycin (Fisher Scientific). The media was removed by aspiration and the cells were washed once with 5 mL of phosphate buffered saline (PBS). Cells were harvested with 5 mL of PBS with 5 mM EDTA for 3 min, at 37 °C. Cells were washed once with a PBS solution containing 1 mM $CaCl_2$ and 1 mM $MgCl_2$ and twice with PBS, pelleted each time by centrifugation at 300 × *g* for 3 min.

3.5.2 *In vivo cross-linking*

Chemical cross-linking was performed in biological duplicate for comparison of HeLa and MCF-7 cells lines and quadruplicates for the comparison of HEK293 and HeLa by individually adding 5 mM of each iqPIR cross-linker (stump heavy or reporter heavy[10]) in 500 µL of cross-linker buffer (170 mM Na_2HPO_4, pH 8.0) to each one of the cell suspensions. Cross-linking reactions were

performed at room temperature for 30 min, with constant shaking, as previously described[10,11]. The iqPIR labeling of cells was designed as follows: (i) HeLa stump heavy *versus* HEK reporter heavy (referred here as forward), (ii) HeLa reporter heavy *versus* HEK stump heavy (referred here as reverse), (iii) MCF-7 stump heavy *versus* HeLa reporter heavy, and (iv) MCF-7 reporter heavy *versus* HeLa stump heavy.

3.5.3 *Sample preparation*

Cross-linked cell pellets were suspended in 8 M urea solution in 0.1M NH_4HCO_3 buffer, pH 8.0, and sonicated 5 times using a GE-130 ultrasonic processor, with amplitude of 40% for 5 seconds. After Bradford assay for protein quantitation, 4 mg of protein from reporter heavy and stump heavy labeled samples were mixed in one 15 mL Eppendorf tube (8 mg total). This was followed by reduction with TCEP, alkylation with IAA, and tryptic digestion. Peptide samples were acidified to pH 2 with trifluoroacetic acid (TFA), followed by desalting by solid phase extraction using C18 Sep-Pak cartridges (Waters) and concentration by vacuum centrifugation. Resulting peptides were suspended in 500 µL of 7 mM KH_2PO_4 in 30% acetonitrile, pH 2.8 and fractionated by strong cation exchange (SCX) chromatography using an Agilent 1200 series high-performance liquid chromatography system equipped with a 250 × 10.0 mm column packed with Luna 5 mm diameter, 100 Å pore size particles (Phenomenex). Peptide were separated using a binary mobile phase solvent system consisting of solvent A and solvent B (7 mM KH_2PO_4, 350 mM KCl, 30% acetonitrile pH 2.8) at a flow rate of 1.5 mL/min using the following gradient: 0-7.5 min 100% A, 7.5-47.5 min 95% A/5% B to 40% A/ 60% B, 47.5- 67.5 min 40% A/ 60% B to 100% B, 67.5-77.5 min 100% B, 77.5-97.5 min 100% A. A total of 14 fractions were collected and pooled as follows: fractions 6-7, 8, 9, 10, and 11-14. Cross-linked peptides from SCX fractions were further

enriched using UltraLink monomeric avidin (Thermo Fisher Scientific). The enriched cross-linked peptide sample was concentrated by vacuum centrifugation and stored at -80 °C.

3.5.4 *LC-MS/MS analysis of cross-linked peptides*

Pooled peptides from SCX fractions (6-7, 8, 9, 10, and 11-14) were resuspended in 30 µL of 0.1% (vol/vol) formic acid. Fractions were centrifuged at 16,000 × *g* for 10 min at room temperature and the supernatant of each sample transferred to an LC autosampler vial (Thermo). For the Mango LC-MS/MS analysis, 3 µL of each sample (approximately 1 µg) from each pooled fraction was injected into the nano-LC system (Thermo), coupled to a Q-Exactive Plus mass spectrometer (Thermo). Each fraction was analyzed either two or three times for technical replicates of the experiment. Each peptide fraction was then loaded onto a trap column [3 cm × 100-µm i.d., stationary phase ReproSil-Pur C8 (5-µm diameter and 120-Å-pore-size particles)] with a flow rate of 2 µL/min of mobile phase: 98% (vol/vol) LC–MS solvent A [0.1% (vol/vol) FA in water] and 2% (vol/vol) LC–MS solvent B [0.1% (vol/vol) FA in acetonitrile], and chromatographically separated using an analytical column [60 cm × 75-µm i.d., stationary phase ReproSil-Pur C8 (5-µm diameter and 120-Å-pore-size particles)], applying a 240-min linear gradient: from 95% LC–MS solvent A, 5% LC–MS solvent B to 60% LC–MS solvent A, 40% LC–MS solvent B, at a flow rate of 300 nL/min. For Mango analysis of the PIR cross-linked peptides, the mass spectrometer was set to high resolution method to data-dependent acquisition (DDA) of the 5 most intense ions with charge state of +4 to +8, with a dynamic exclusion of 30 s and isolation window of 3 Da. Each MS1 scan (70,000 resolving power at 200 m/z, automated gain control (AGC) of 1×10^6, scan range 400 to 2,000 m/z, dynamic exclusion of 30 s) was followed by 5 MS2 scans (70,000 resolving power at 200 m/z, AGC of 5×10^4, normalized collision energy of 30). For ReACT[42] LC-MS^n analysis, the hybrid LQT Velos FT-ICR was set with DDA of the 6 most intense ions

with charge state of +4 to +8, with dynamic exclusion of 45 s and isolation window of 3 Da. Each MS1 scan (50,000 resolving power at 200 *m/z*, mass range 500 to 2,000 *m/z*) was followed by 1 MS2 acquisition for the "on-the-fly" mass relationship check – mass precursor = mass reporter + mass peptides – (12,500 resolving power at 200 *m/z*, CID activation, normalized collision energy of 25), and 4 MS3 acquisitions of the selected ions with a 20 ppm tolerance for mass error after the mass relationship check, and with 1+ and 2+ charge states (CID activation, normalized collision energy of 35). This strategy resulted in 2 technical replicates (mango and ReACT) for each biological replicate of MCF-7 versus HeLa (forward and reverse).

3.5.5 *Data processing and cross-link quantitation*

For mango[46] analysis, .ms2 files were generated containing individual precursor masses of released peptides for each spectrum and .peaks file containing all relationships within a 20 ppm tolerance. Comet[47] (version 2019.01 rev. 4) was used to search mzXML files against the human database downloaded from UniProt[174] on January 1st 201. For MCF-7/HeLa comparison 3,234 unique protein sequences included in the database were identified as putative cross-linked proteins through a stage 1 database approach as previously described[51]. For ReACT *in silico* analysis, MS^3 spectra containing peptide fragmentation information was searched within 10 ppm against the same database using Comet. Then, react2csv was run on search results (*pep.xml files) to map ReACT2 results to the sequences in the database. The data were filtered to an estimated maximum false discovery rate (FDR) of 1% at the non-redundant cross-linked peptide level. The cross-linking quantitation was done as describe[63]. The cross-linking results were uploaded to XLinkDB[175].. XLinkDB uses Cytoscape[176] to generate cross-link and protein networks, Lorikeet (https://uwpr.github.io/Lorikeet/) for spectrum view, xiNET[177] for cross-link network display, and

NGL viewer[178] for visualization and edition of protein structures and cross-links. AlphaFold[86] structures were uploaded to NGL viewer for cross-linking mapping.

3.5.6 *Data analysis and statistical analysis*

95% confidence interval was calculated for each log_2 ratio; cross-links with log ratio in all biological replicates (MCF-7 to HeLa comparison) or with log2ratios in at least three biological replicates (HEK293 to HeLa comparison) and with each log2ratio having 95% confidence less or equal to 0.5 and having at least 4 ions contributing to the ratio were considered quantified with high confidence. Student's one-sample t-test was performed for each log2ratio based on every peptide and peptide fragment quantified and p-value was assigned. Bonferroni multiple testing correction was applied based on number on all confidently quantified cross-links. Confidently quantified cross-links with corrected p-value less than 0.05 were considered significantly changing between cell lines in each comparison. Correlation, volcano plots, and density plots were generated in R using ggplot2 package[133].

3.5.7 *DIA proteome quantitation.*

MCF7, HeLa, and HEK293 cells were grown in triplicates in the same conditions as for cross-linking experiments. After harvesting, cells were lysed in 8M urea. Proteins were reduced with TCEP and alkylated with IAA and digested overnight with trypsin. Peptides were then desalted on c18 Seppak columns (Waters), dried down and resuspended in 0.1% formic acid. 1 ug of peptides was loaded on the column for each run. Peptides were separated on a 30 cm column packed with c18 reprosil, 5 um resin. Data was acquired and processed as described in Pino et al[179]. Briefly, gas fractionated libraries were acquired using overlapping 4 m/z windows using a pooled sample. Then large window (24 m/z) DIA data was acquired for each individual sample. The data was

processed in EncyclopeDIA[180] (and output with protein intensities was used for downstream analysis in R. Protein intensities were then $\log_2$ transformed and median normalized. The normalized values were used for heatmaps and boxplots. T-test and Benjamini-Hochberg correction for multiple testing was performed using built in R functions.

3.5.8 *C2c12 mitochondrial isolation and cross-linking*

C2c12 cells were grown in DMEM media supplemented with 20% FBS and 1% penicillin/streptomycin. Differentiation was induced by switching to 2% horse serum when the cells were 70% confluent. Cells were collected similarly to human cell lines described previously. Mitochondria was isolated according to previously published protocol[181]. Briefly, cells were homogenized in Dounce homogenizer in isolation buffer (10 mM Tris-MOPS, 1 mM EGTA, 200 mM sucrose, pH 7.4) with 1 uM BKA or CATR purchased form Cayman Chemical, or without wither for controls. The homogenates were spun down at 600g to get rid of cellular debris. Then supernatants were spun down at 7000 g and mitochondrial pellets were washed once. Mitochondria were cross-linked in 150 uL of cross-linking buffer in the presence of wither either BKA or CATR with reporter heavy reagent (RH). Controls were cross-linked with stump heavy (SH) reagent. Cross-linking reaction was allowed to proceed for 30 min. Supernatants were then removed by centrifugation and mitochondrial pellets were lysed. BKA or CATR treated cross-linked mitochondria were combined with control mitochondria in 1:1 ratio based on protein amount and processed similarly to cross-linked cell samples described earlier.

3.6 SUPPLEMENTAL FOR CHAPTER 3

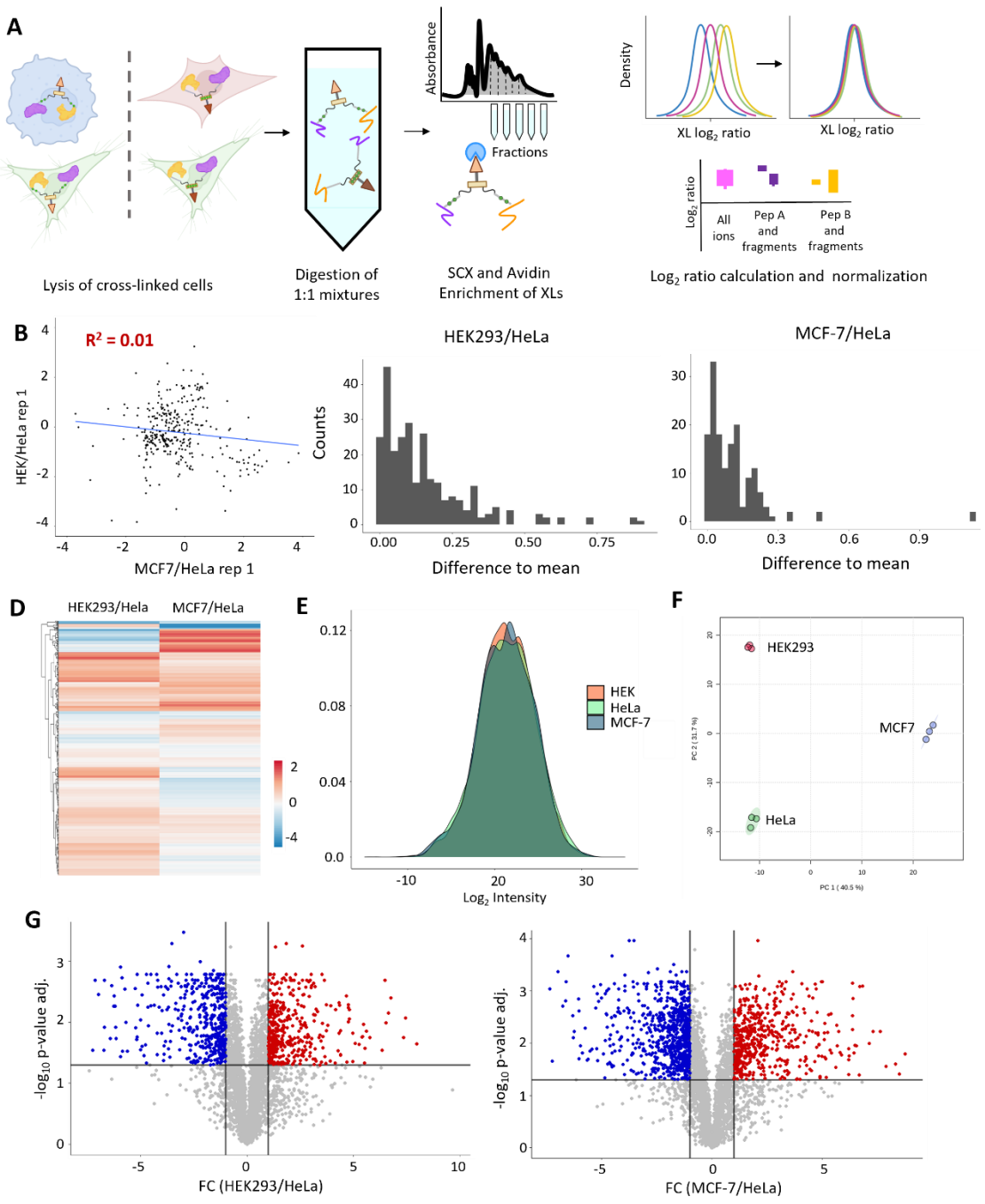

Figure 3.8 Quantitation of cross-links and proteins. A. Workflow for processing cross-linked cells. B.Correlation plot between MCF7/HeLa and HEK293/HeLa replicates. C. Difference to the mean for quantitation of cross-links corresponding to same residue pairs for HEK293/HeLa (left) and MCF-7/HeLa (right) datasets. D. Heatmap of cross-links common between MCF-7/HeLa and HEK293/HeLa datasets. E. Distribution of log2 intensities for DIA data in all three cell lines. F. PCA plot based of DIA data shows clustering of biological

replicates according to cell line. G. Volcano plots of protein level fold changes and Benjamin-Hotchberg corrected p-values with 0.05 cutoff for significance.

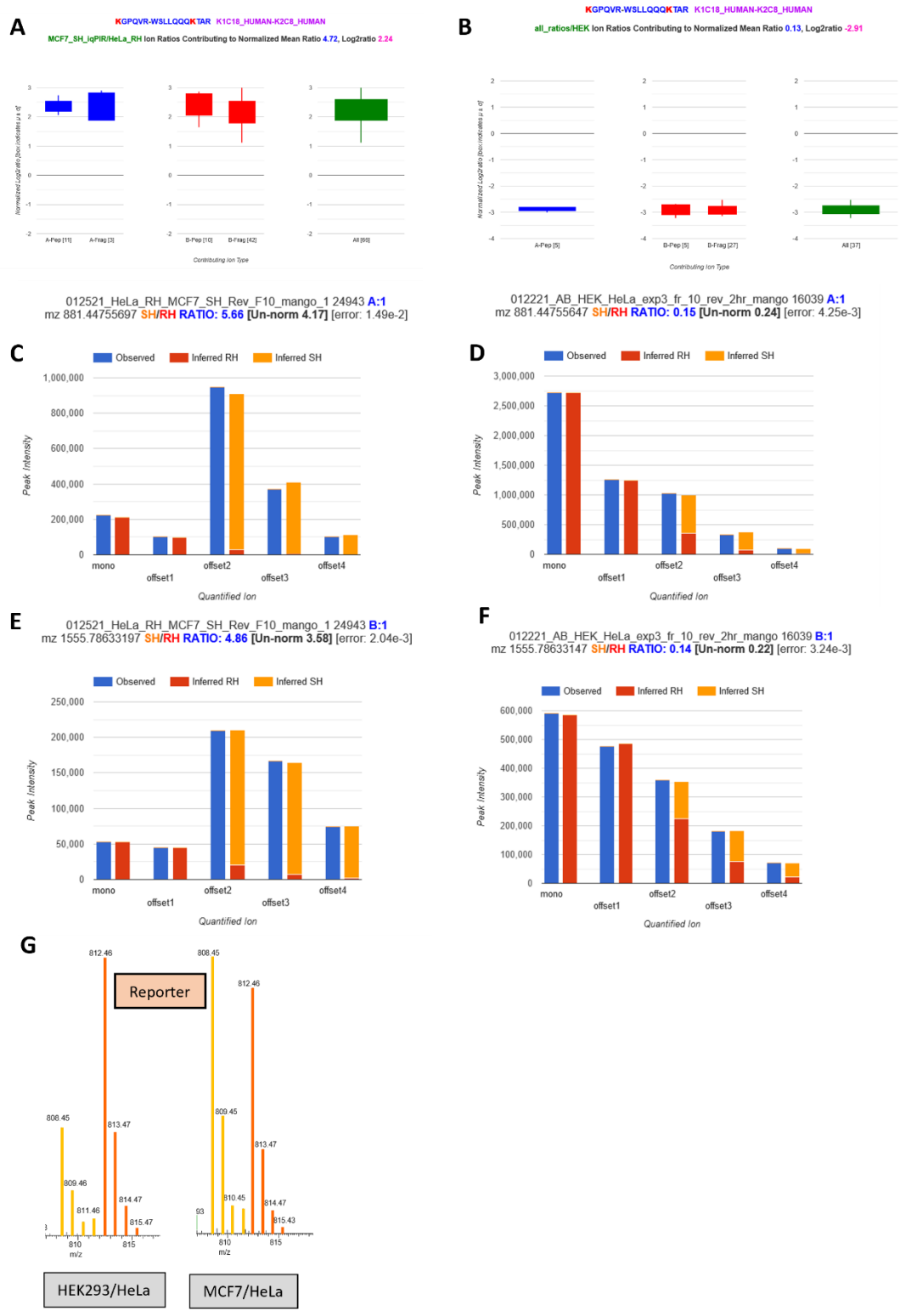

Figure 3.9 Quantitation of K1C18 K119 to K130 on K2C8 cross-link. **A, B**. Boxplots of all ions quantified in MCF-7/HeLa reverse replicate (A) or HEK293/HeLa reverse replicate (B). **C-F**. Decomposition of observed

isotopic envelops of released peptides with iqPIR algorithm into each channel (RH or SH) contribution. **G**. Reporter spectra with light reporter (808) in yellow and heavy reporter (812) in orange. Ratios of the reporter channels is closer to 1 than for peptides and their fragments because of ratio compression.

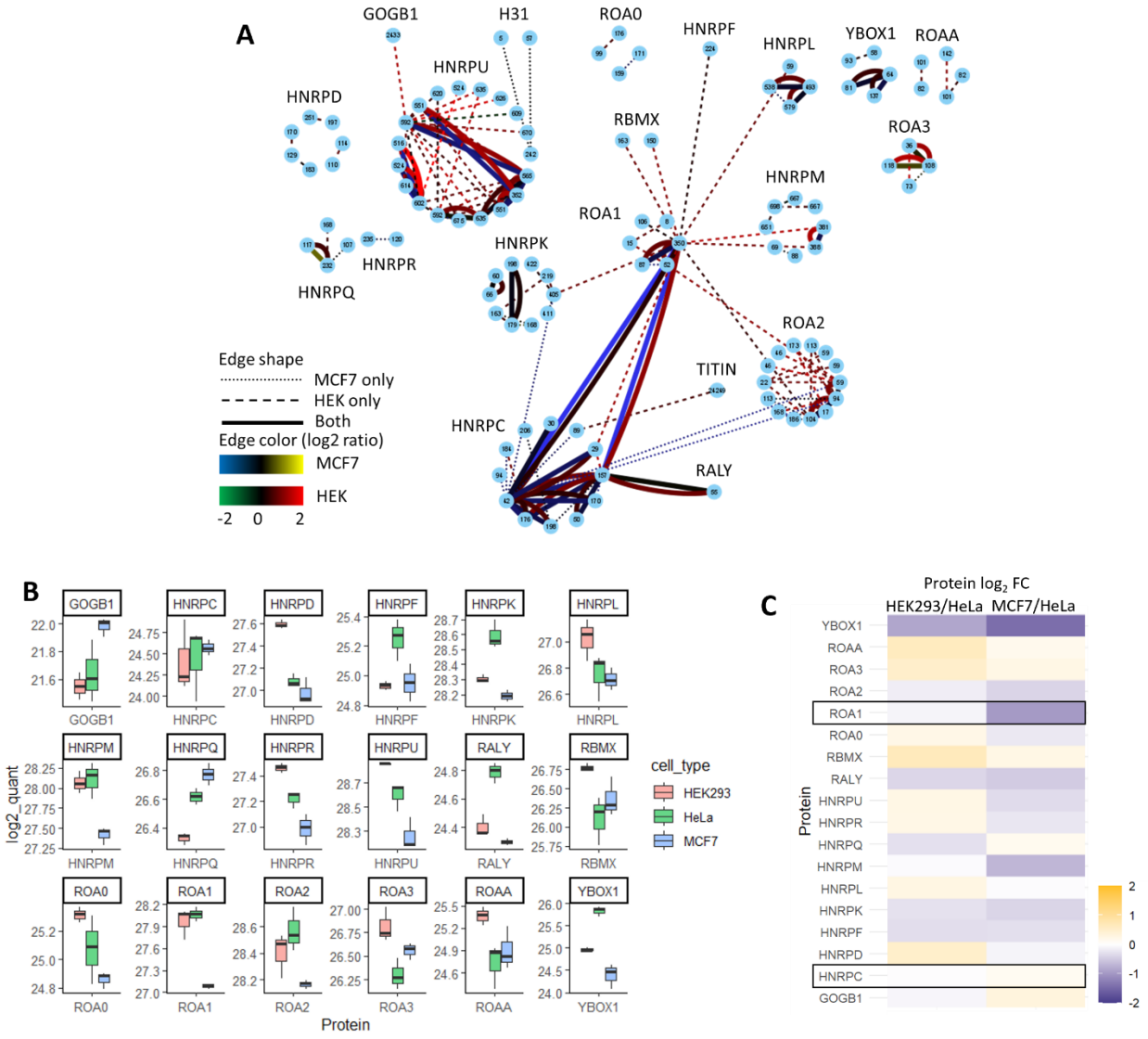

Figure 3.10 RNABPs cross-link networks and protein quantitation**. A**. Cytoscape network for RNPs. Each node represents cross-linked residue with its number indicated inside the node. Edges represent detected and quantified cross-links. **B**. Boxplots comparing DIA based protein levels for HNRNPs in three cell lines. **C**. Heatmap showing $\log_2$ fold change in HEK 293 or MCF7 compared to HeLa of protein levels based on DIA measurements for HNRNPs.

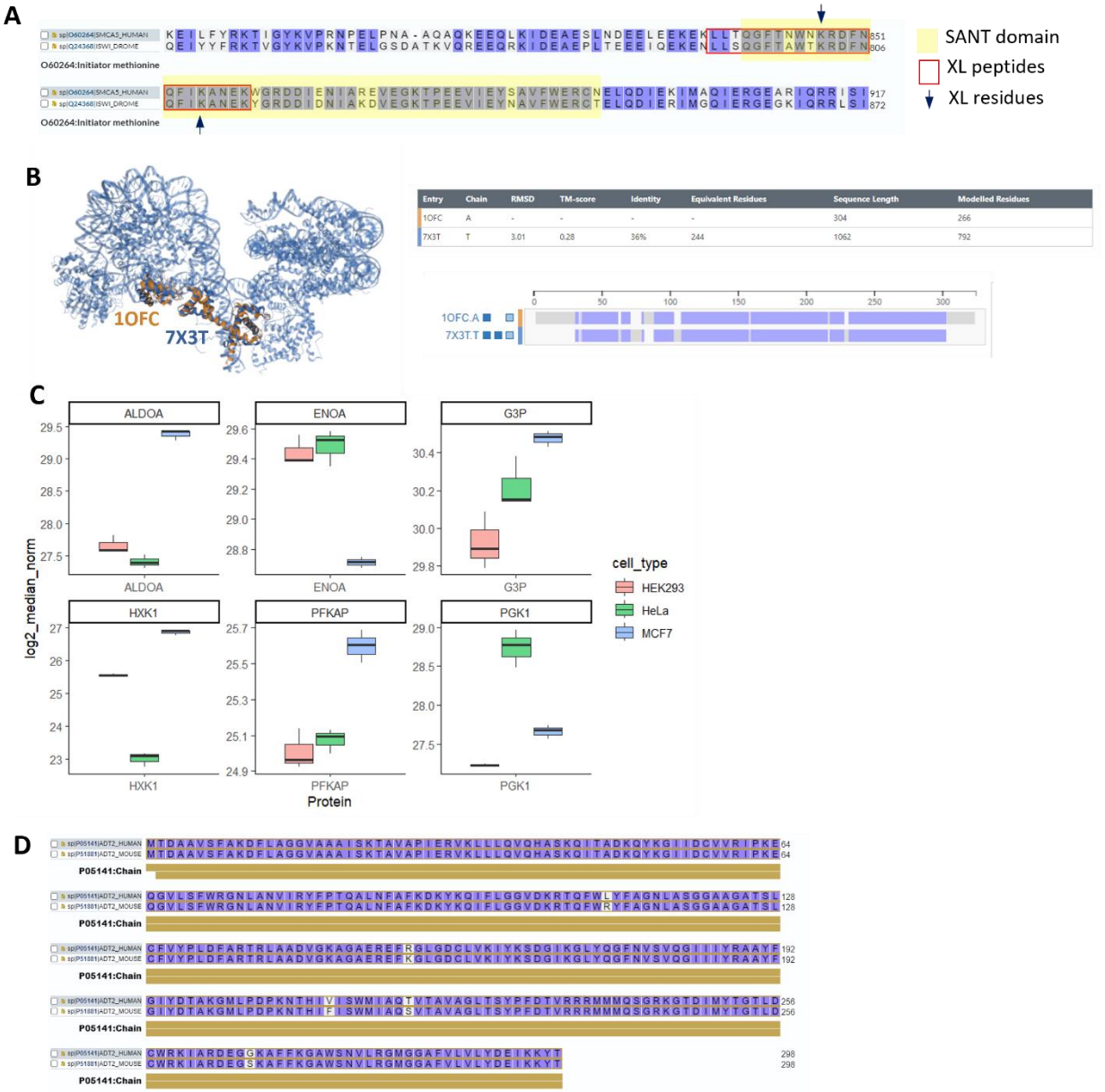

Figure 3.11 Chromatin remodeling, glyoxolase activity and ADT activity. **A.** Alignment of C-terminal residues of human SMCA5 and fly ISWI. **B**. Stractural alignment of fly ISWI (1OFC) and yeast ISW1a complexed with dinucleosomes (7X3T). **C**. Protein levels of glycolytic enzymes in all three cell lines. **D**. Alignment of mouse and human sequences of ADT2 showing a high homology.

Chapter 4. INTRA-ORGAN CELL-SPECIFIC MITOCHONDRIAL INTERACTOMES

4.1 ABSTRACT

Almost every organ consists of many cell types, each with its unique functions. Proteomes of these cell types are thus unique too. But it is reasonable to assume that interactome (inter and intra molecular interactions of proteins) are also distinct since protein interactions are what ultimately carry out the function. Podocytes and tubules are two cell types within kidney with vastly different functions: podocytes envelop the blood vessels in glomerulus and act as filters while tubules are located downstream of glomerulus and are responsible for reabsorption of important nutrients. It has been long known that for tubules mitochondria plays an important role as they require a lot of energy to carry out their function. In podocytes, however, it has been assumed that mitochondria might not matter as much in both normal physiology and pathology. Here we have applied quantitative cross-linking mass spectrometry to compare mitochondrial interactomes of tubules and podocytes. We have uncovered that mitochondrial proteomes of these cell types are quite similar, although still showing unique features that correspond to known functions, such as high energy production through TCA cycle in tubules and requirements for detoxification in podocytes which are on the frontline of filtering out compounds that could be toxic. But we gained much deeper insight with the interactomics data. We were able to find pathways differentially regulated in podocytes and tubules based on changing cross-link levels and not just protein levels. Among these pathways are betaine metabolism, lysine degradation, and many others. We have also demonstrated how quantitative interactomics could be used to detect different activity level of an enzyme even when protein abundances of it are the same. We have validated this finding with orthogonal activity assay. Overall, this work present a new view

at mitochondrial biology of both important but functionally distinct cell types within the mouse kidney showing both similarities and unique features. This data can be continued to be explored to find new aspects of mitochondrial biology, especially in podocytes, where mitochondria has been understudied. In the future this methodology can also be applied to other organs to uncover differences in function of the cell types.

4.2 INTRODUCTION

Over the last few years omics fields such as genomics, transcriptomics and proteomics have been moving toward studying cell type heterogeneity. This was made possible by great advances in single cell technologies.[182,183] Interactomics, or study of intra and inter protein interactions on a system level usually by the means of cross-linking mass spectrometry (XL-MS), has inherent constraints that make move toward single cell studies particularly challenging. Cross-links are formed by addition of a cross-linking reagent reactive toward specific protein residues (most commonly lysines), with low efficiency and require high input amounts to be detected[184]. Although, cell typed specific protein-protein interactions in cultured cell lines have been studied by other means, such AP-MS[17], there are no reported cell type specific interactomes stemming from the same animal organ. Making interactome data quantitative (i.e. finding differences that are not just present/absent but have a more subtle variation) is an even bigger challenge[55]. Here, we report the first quantitative comparison of mitochondrial interactomes of two cell types originating in the same organ substructure: podocytes and tubules from kidney glomerulus. By combining quantitative XL-MS (qXL-MS) technique that utilizes isobaric quantitative Protein Interaction Reporter (iqPIR)[63] and novel mouse models that express HA tag on mitochondrial outer membrane of kidney cells (unpublished data) in cell type specific manner, we were able to detect quantitative differences in the interactomes. qXL-MS allows to detect changes that are

interaction (protein-protein and protein-ligand), conformation, and lysine post translational modifications (PTMs) driven. Our method showed remarkable reproducibility between biological replicates with the lowest R^2 value of 0.8. By adding DIA-based quantitative mitochondrial proteome comparisons we established interactome differences that are independent of protein abundances.

Mitochondrial proteome differences between podocytes and tubules offered some insights but pathway analysis was limited as only 45 mitochondrial proteins are differentially expressed. On the other hand, utilizing proteins with differential cross-link abundances allowed us to perform pathway analysis and we were able to identify several pathways that were differentially expressed including betaine metabolism and lysine metabolism. It shows that mitochondria plays important albeit somewhat distinct role in podocytes compared to tubules.

Previously reported differences in cross-links in antenna region of glutamate dehydrogenase (DHE3) and their relation to the activity[143] were detected and differences in DHE3 activity between podocytes and tubules were confirmed orthogonally with colorimetric activity assay.

Overall, this work demonstrates the ability to quantitatively compare interactomes of mitochondria originating from different cell types within an organ. Moreover, insights gained into underexplored mitochondrial biology of podocytes open the door to further studies that can elucidate role of mitochondria in podocyte physiology and podocyte dependent kidney pathology.

4.3 Results and Discussion

4.3.1 *Quantification of interactome differences between podocyte and tubule mitochondria*

Mitochondria was isolated from mouse kidneys with HA tag on either podocyte mitochondria (NPHS2-mtHA) or tubule mitochondria (CDH16-mtHA) using affinity purification column.

Mitochondria from podocytes was cross-linked with reporter heavy (RH) cross-linker and tubule mitochondria was cross-linked with stump heavy (SH). Podocyte mitochondria from each mouse was combined with tubule mitochondria creating three pairs (P1 = pod1/tub1, P2 = pod2/tub2, P3 = pod3/tub3) in 1:1 ratio. Each combined sample was then digested and cross-linked peptides were enriched and fractionated. The fractions were then analyzed with LC-MS/MS, data searched against mouse Mitocarta database[87] and cross-links identified and $\log_2$ ratios were calculated as described previously (**Figure 4.1**) [63,143]. We were able to identify 5119 cross-links and confidently (at least 4 ions contributing to the ratio and 95% confidence < 0.5) and quantify 835, 1994, 1996 in P1, P2, P3 respectively (**Figure 4.1,** Figure 4.5). We then calculated a combined ratio based on ions from all replicates. Filtering for combined ratios that have also at least 2 individual ratios resulted in 2040 ratios. P1 had lower starting protein amount than P2 and P3. Due to this and sample processing issues P1 had fewer identified and quantified cross-links than P2 and P3. Log_2 ratios for each pair are approximately normally distributed with majority of cross-links not changing as expected (Figure 4.5). We were able to achieve great reproducibility between the pairs as indicated by R^2 values of 0.80, 0.82 and 0.84 (**Figure 4.1**). Cross-links that are decreased, increased or do not change have been quantified as indicated by heatmap of cross-links quantified in at least two out of three pairs (**Figure 4.1**). Applying Student's t-test with Bonferroni correction, we were able to identify cross-links with ratios different from 0 ($|\log_2$ ratio$| > 0.5$) with statistical significance (**Figure 4.1**).

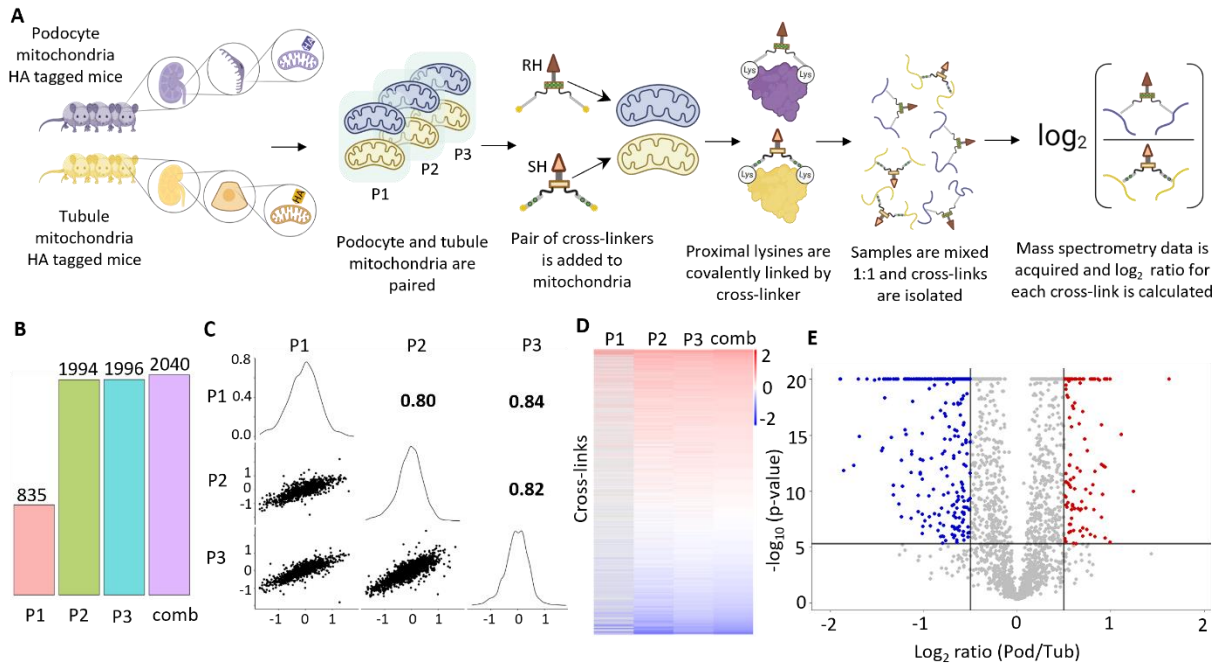

Figure 4.1 Quantitative comparison of tubules and podocytes interactomes. A. Quantitative cross-linking with iqPIR workflow. Mitochondria was isolated from mice expressing the HA tag on outer mitochondrial membrane in either podocytes or tubules. Mitochondria from podocytes was then cross-linked with reporter heavy (RH) iqPIR reagent and from tubules with stump heavy (SH) reagent to produce a ratio for each cross-link. B. Number of confidently quantified cross-links (95% confidence < 0.5 and at least 4 ions used for quantitation) in each pair (P1-P3) and number of cross-links with confident combined ratio (comb, at least 2 out of three individual confident ratios). C. Pairwise correlations between confidently quantified cross-links with Pearson's R2 values indicated. D. Heatmap of confidently quantified cross-links shows great agreement among the pairs. E. Volcano plot of cross-links log2 ratios with 0.05 Bonferroni corrected p-value from one-sample t-test and 0.5 log2 ratio used to determine significance.

To complement quantitative interactome data we also acquired proteome measurements for the same samples utilizing DIA-based quantitative proteomics workflow[179,180]. Having information about protein level changes allowed us to distinguish cross-links that are different due to changes in protein abundance and the cross-links that are different due to protein-protein interactions, conformations, protein-ligand interactions or PTMs. Utilizing chromatographic libraries and DIA based quantitation we have confidently quantified 779 protein groups searching against mitochondrial proteome database Mitocarta[87] (Figure 4.5). Overall, mitochondrial proteomes of

tubules and podocytes seem quite similar with only 45 proteins out of 779 being differentially expressed (Benjamin-Hochberg corrected p-value < 0.05 and |FC|> 0.5, Figure 4.5). This result is somewhat surprising considering that generally tubules are believed to have greater reliance on mitochondria than podocytes[185]. This could partially be explained by the fact that we normalize mitochondrial protein amount, and it is known that mitochondrial density is lower in podocytes[186]. Overall, with only 21 proteins significantly up in podocytes and 24 in tubules, it is challenging to perform a meaningful pathway enrichment analysis, but tubule mitochondria shows upregulation of TCA cycle and respiratory chain complex I assembly, while cellular detoxification and antioxidant activity is upregulated in podocytes (Figure 4.5). While the number of differential proteins is low for an extensive pathway analysis, these results generally agree with functions of tubules and podocytes. Tubules have high energy demand due to the active transport across cell membrane. Podocytes are located right at the interface with blood that needs to be filtered by the kidney, so a robust antioxidant system that can help counteract cytotoxicity is needed.

Genetically encoded affinity tag such as HA, placed at outer mitochondrial membrane, allows for enrichment of the organelle from the tissue homogenate, but this enrichment is not perfect and organelles and proteins that surround the mitochondria are also pulled down. To investigate how this background compares between podocyte and tubule mitochondria we have searched both cross-linking and DIA proteomics data against whole mouse database. We have quantified 2024 proteins in these searches with 943 proteins being differentially expressed (**Figure 4.2**), a much larger number than in our mitochondrial searches. We have performed pathway enrichment analysis that showed that the majority of proteins increased in tubule mitochondria are mitochondrial (536 out of 562 proteins, **Figure 4.2**), while proteins up in podocyte mitochondria

are lysosomal (107), cytosolic (299) and cytoskeletal (67) (**Figure 4.2**). The upregulation of xmitochondrial proteins and pathways in tubules thus reflects higher mitochondrial content in the pull-down from tubules and not differential expression of proteins in the mitochondria. At the same time mitochondrial pull-down in podocyte has a large amount of non-mitochondrial proteins. It is particularly interesting that lysosomal proteins represent a large portion of the non-mitochondrial proteins in podocytes. This is in agreement with previous work (unpublished), where western blots were used to compare abundance of lysosomal marker LAMP1 between the pull-downs. Quantitative proteomics done in this study also shows higher abundance of LAMP1 in podocyte pull-down (**Figure 4.2).** Similarly, components of lysosomal proton pump also have higher abundance in podocyte pull-down (Figure 4.6). On a cross-link level we see similar increase in lysosomal proton pump cross-links (**Figure 4.2**). Besides intralinks in VATA, VATE1, VATB2, we have also detected and quantified inter-links connecting these proton pump subunits, indicating that intact lysosomal proton pump has been pulled down and not just individual subunits. Taken together our data show that podocyte mitochondria might have more lysosomal contacts as indicated by increase in lysosomal protein abundances and cross-links. Lysosomal clearance of damaged mitochondria is important for podocytes since these are terminally differentiated cells that are under constant cytotoxic stress, so abundance of lysosomes near mitochondria could be expected.

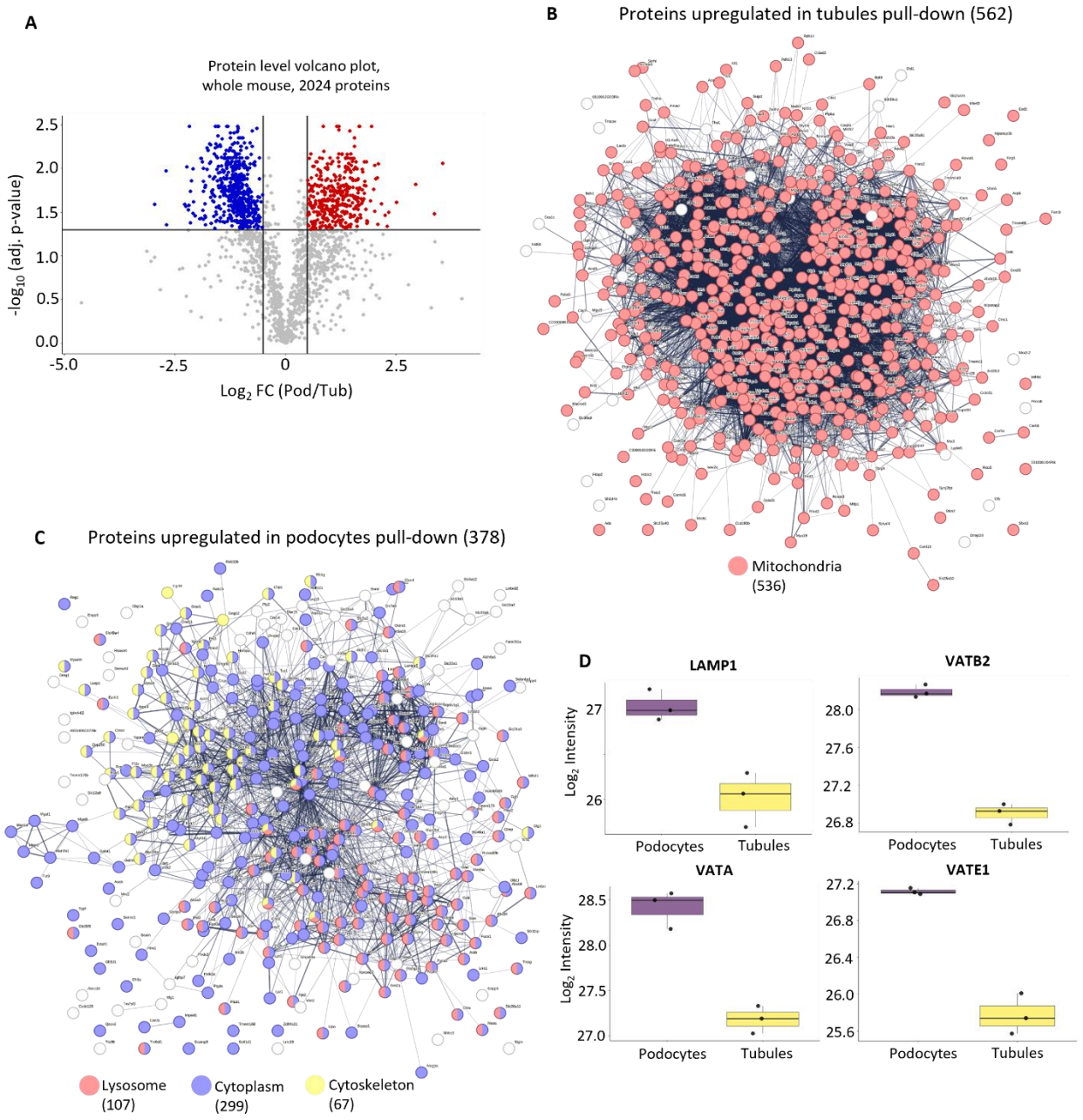

Figure 4.2 Proteomics analysis utilizing whole mouse database searches in the podocyte and tubules pull-down. A. Volcano plot demonstrating differential proteins between podocyte and tubule pull-down. B. Proteins increased in tubule pull-down. The majority of proteins are annotated as mitochondrial. C. Proteins increased in podocyte pull-down. Lysosomal, cytosolic and cytoskeletal proteins are enriched in this pull-down. D. Boxplots comparing select lysosomal protein levels between podocytes and tubules.

4.3.2 *Significantly changed cross-links identify mitochondrial pathways different between podocytes and tubules.*

While mitochondrial proteomes do not show large number of proteins changing, the main advantage of this study is quantitative interactome data that allows us to leverage knowledge of differences in protein interactions and conformations even when protein levels do not change. We used proteins with significantly changed cross-links (both increased and decreased in podocytes compared to tubules) to perform a pathway enrichment analysis. The top gene ontology biological process was identified as betaine metabolic process (**Figure 4.3**). Cross-links belonging to 9 proteins from this pathway have been identified as significantly changed (**Figure 4.3**) with both increased and decreased cross-links present (**Figure 4.3**). None of the proteins in this pathway show significantly changed abundancies (OCTC, peroxisomal carnitine O-octanoyltransferase, having the biggest change with $\log_2$ FC = 0.76 and adjusted p-value = 0.07, so this pathway wouldn't have been identified as significant based on proteome data alone. Betaine (also known as trimethylglycine) is an amino acid that is important for osmotic regulation[187]. In kidney, it has been shown that supplementation with betaine can have a protective effect during chronic kidney disease and doxorubicin induced toxicity[188,189]. Investigating further the differences in betaine processing between podocytes and tubules could shed light on mechanisms of betaine protection.

Another pathway that we weren't able to identify without interactomics data is lysine degradation, which is the top hit in KEGG (Kyoto Encyclopedia of Genes and Genomes) analysis (**Figure 4.3**). Kidney plays an integral role in lysine metabolism[190]. Lysine role in chronic kidney disease has also been documented[191]. Effect of lysine supplementation on a kidney proteome has been investigated and AASS, an enzyme responsible for lysine oxidation to

saccaropine was highlighted[190]. Levels of AASS are the same between podocytes and tubules (**Figure 4.3**) but cross-link level analysis shows significant differences. The majority of studies of lysine role in kidney physiology and pathology uses whole kidney tissue or isolated proximal tubules. Our quantitative comparisons of tubule and podocyte interactomes and proteomes could help study lysine metabolism at higher resolution in kidney.

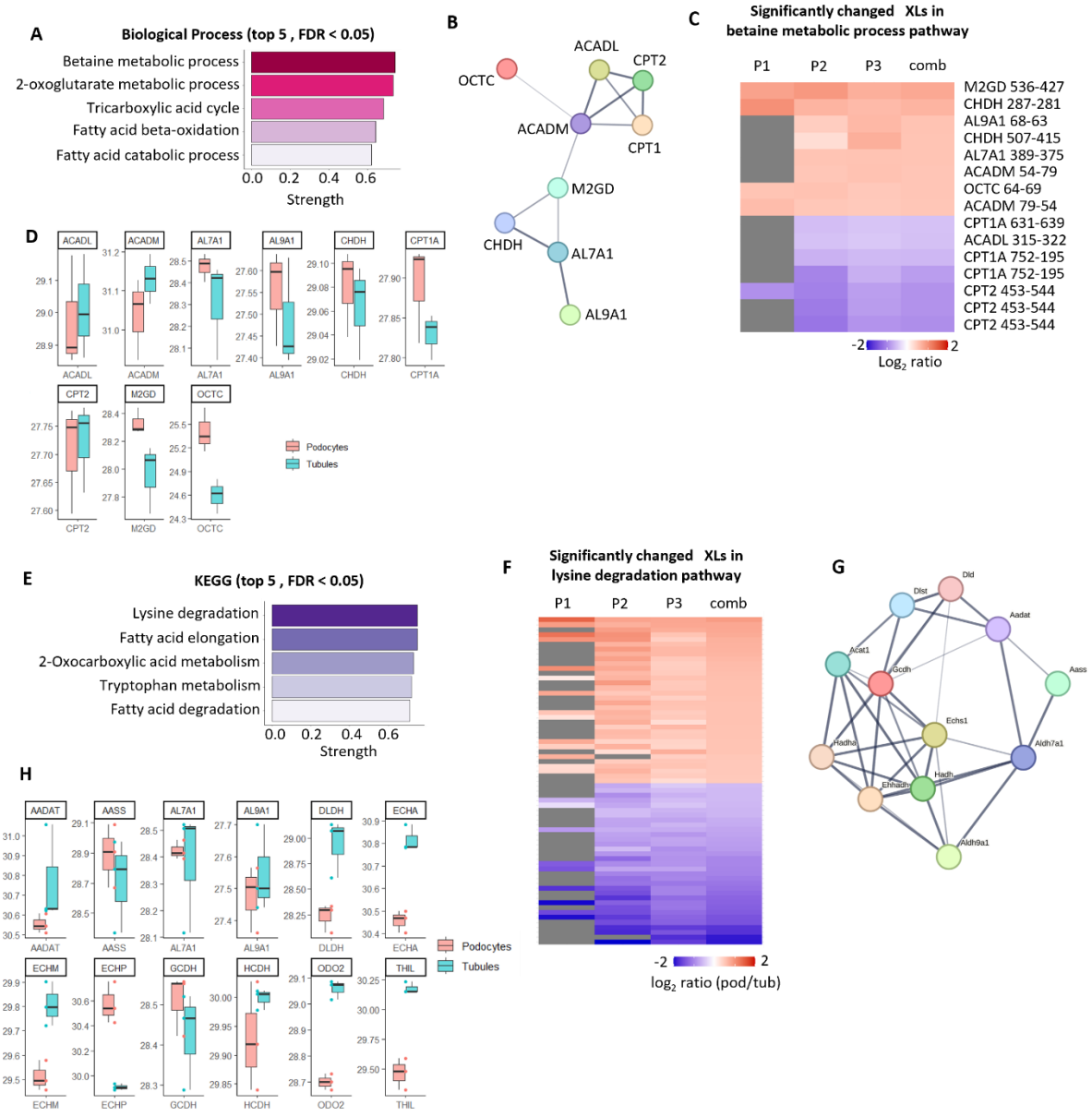

Figure 4.3 Pathway analysis of differential cross-links. A. Top 5 biological processes differential in podocytes and tubules. B. Proteins in betaine metabolic pathway that have differential cross-links. C. Heatmap of

differential cross-links from betaine metabolic pathway. D. Protein level comparison of betaine metabolic process proteins that had differential cross-links. E. Top 5 KEGG pathways identified. F. Heatmap of significantly changed cross-links in lysine degradation pathway. G. Proteins from lysine degradation pathway with differential cross-links. H. Protein level comparison of lysine degradation proteins that had differential cross-links.

4.3.3 *Glutamate dehydrogenase activity but not protein levels are decreased in podocytes.*

Glutamate dehydrogenase (DHE3), encoded by *Glud1* gene, is a mitochondrial matrix enzyme responsible for oxidative deamination of glutamate to produce alpha-ketoglutarate (aKG), an intermediate of TCA cycle (**Figure 4.4**)[107]. The expression of DHE3 in mitochondria between podocytes and tubules is the same (**Figure 4.4**), while on the cross-link level there are extensive differences (**Figure 4.4**). There are cross-links that show no change and some that are increased. There is also a subset of cross-links that are significantly decreased in podocytes. These cross-links are localized to the antenna regions of hexameric DHE3. We have previously shown that the same cross-links are decreased in female muscle mitochondria with aging[143] and were able to demonstrate that these cross-link increase with treatment by ADP, a well-known activator of DHE3 activity[110]. To investigate further DHE3 activity in podocytes and tubules we performed an activity assay which measures NADH absorbance as it being produced during the reaction, using both mitochondria from the same mice as were cross-linked and also 3 more pairs. Indeed, time to reach half maximum of the NADH absorbance in tubules was shorter compared to podocytes, indicating that DHE3 activity is higher in tubules (**Figure 4.4,** Figure 4.7). DHE3 is an important enzyme that operates as a metabolic switch by employing intricate regulatory system that, curiously, co-evolved with the antenna[107]. To investigate a possible underlying mechanism driving increased activity we have performed activity assays and quantitative cross-linking experiments treating mouse liver mitochondria with either DHE3 activator (ADP), inhibitor (GTP), or both (**Figure 4.4,** Figure 4.7**)**. The antenna cross-links increased in response

to ADP or ADP + GTP treatment but not to GTP treatment alone. There was also no response to either ADP or GTP when no substrates were added (the mitochondria was previously frozen, so it is expected that due to membrane raptures small molecules like glutamate and NAD^+ would be lost). These results indicate that antenna cross-links are responsive to ADP activation but not to GTP inhibition, indicating that differences in DHE3 activity in podocytes in tubules might be driven by the ADP activation and not GTP inhibition.

Another reported way of how DHE3 is regulated is through association with HCDH, hydroxyacyl-coenzyme A dehydrogenase encoded by *Hadh* gene[192,193]. HCDH is an enzyme involved in oxidation of short chain fatty acids that has been shown to interact with multiple mitochondrial metabolic enzymes[194]. HCDH protein abundance does not change between mitochondria of podocytes and tubules (**Figure 4.4**). On the other hand, cross-links $\log_2$ ratios seem to form two clusters, one does not change in agreement with protein level data, while a second cluster is increased (**Figure 4.4**). The second cluster is comprised of cross-links that are only within the distance constraints of iqPIR if they are mapped as an interlinks in HCDH homodimer, suggesting an increase in a dimer formation (**Figure 4.4**). Dimerization of HCDH has been shown to be important for catalytic efficiency[195]. It is unclear if HCDH interacts with DHE3 as a dimer or a monomer, but its regulation of DHE3 activity appears to be non-enzymatic[193]. So, it is possible that higher abundance of HCDH dimers together with higher catalytic activity leads to higher levels of CHE3 inhibition in podocyte mitochondria relative to tubule mitochondria.

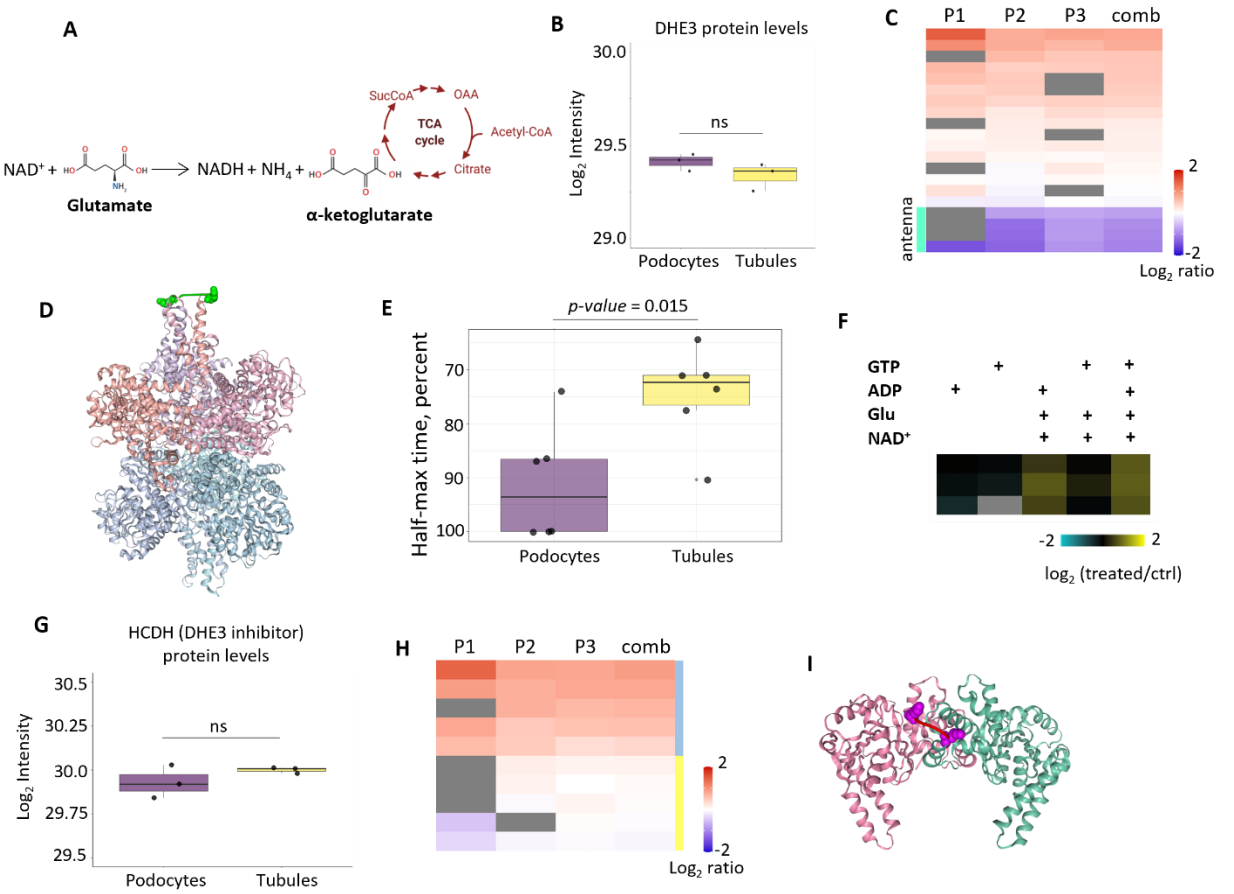

Figure 4.4 DHE3 cross-links and its activity are decreased in podocytes compared to tubules. A. DHE3 converts glutamate and NAD^+ to NADH, ammonia and alpha-ketoglutarate, a TCA cycle intermediate. B. Podocyte and tubule mitochondria have similar DHE3 levels. Significance is determined by two-sided t-test with Benjamin-Hochebrg correction (ns = non-significant). C. Heatmap of all confidently quantified DHE3 cross-links. D. Structure of DHE3 with a representative antenna link. E. Boxplot comparing time to reach half maximum of NADH absorbance as measured by DHE activity assay in podocytes and tubules. The times are normalized to the maximum of each experiment. Statistical significance is determined by two-sided t-test. F. Heatmap of antenna cross-links measured in previously frozen liver mitochondria with addition of ADP, GTP and ADP+GTP. G. HCDH protein levels in podocytes and tubules. H. Heatmap of HCDH cross-links. Blue bar indicates homodimeric interlinks and yellow bar indicates intralinks. I. A representative homodimeric link mapped to a human HCDH structure.

4.3.4 *Concluding remarks*

Here we have demonstrated, for the first time, that iqPIR based quantitative cross-linking mass spectrometry can be used to detect reproducible differences in interactomes originating from the

different cell types withing the same organ. Mitochondria of kidney podocytes and tubules show few differences on a proteome level but more extensive once on interactome level. We were able to identify pathways that are differentially regulated using cross-linking data that would not be apparent with just proteome data. We have discovered differential activity of glutamate dehydrogenase through cross-links in its antenna region and confirmed it by orthogonal assay. Data generated in this study will be publicly available and could be used by the community to gain a deeper understanding in differences between mitochondrial biology of tubules and podocytes. In the future, interactomes of other intra-organ cell types could be studied with this method to gain new insights into their biology.

4.4 METHODS

4.4.1 *Cross-linking of mitochondria*

Mitochondria was cross-linked and processed as reported before.[143] Briefly, mitochondria was cross-linked with either RH iqPIR reagent (podocytes) or SH reagent (tubules). Reaction was allowed to proceed for 30 minutes. Mitochondria weas then lysed in 8 M urea, sonicated, reduced with TCEP and alkylated with IAA. Protein content was measured with Bradford assay and then protein from podocytes and tubules were mixed pairwise in 1:1 to maximize total protein per pair (podocyte sample with highest protein amount was mixed with tubule sample with highest protein amount and so on). Mixed samples were digested overnight with trypsin and cleaned up using c18 SepPak (Waters). Peptides were then fractionated using SCX column and fractions containing cross-links or deadends were used for avidin capture. Fractions were then separated on Aquity nanoHPLC (Waters) and analyzed on QE plus mass spectrometer

(ThermoFischer Scientific). The data was acquired in DDA mode with top 5 peaks with charge >3 chosen for MS^2.

4.4.2 *Data processing and analysis*

Mass spectrometry data was then searched with Mango software to identify spectra containing cross-linked peptides.[46] The spectra was then searched with comet engine and cross-link identifications verified with XLinkProphet.[47,48] Cross-links and deadends were then quantified with iqPIR algorithm to produce $\log_2$ ratio.[63] A combined ratio was calculated by using ions from all samples. Cross-links IDs and associated quants were then uploaded into XLinkDB for structure mapping, further analysis and visualization.[129] XLinkDB formatted table was exported for downstream analysis in R using tidyverse environment.[133]

4.4.3 *DIA based protein quantitation.*

After cross-linked mitochondrial samples were lysed and alkylated 20 ug of each sample was set aside for whole proteome quantitative analysis. The samples were digested overnight with trypsin, peptides were then cleaned up using c18 SepPak columns, dried down, and resuspended in 0.1% formic acid to a final concentration of 0.5 ug/uL. DIA data was acquired and analyzed as reported before.[179,180] Briefly, a pooled samples was made by mixing all samples in equal amounts. Gas phase fractionated (GPF) narrow window (4 m/z) libraries were then acquired using pooled sample. Wide window (24 m/z) DIA runs were then acquired for each sample. The chromatographic libraries were constructed in Encyclopedia using GPF runs searched against mouse Mitocarta 3.0 database.[87] Wide window runs were searched against the libraries. Table with protein quantitation was then imported into R for downstream analysis.

4.4.4 *Glutamate dehydrogenase assay*

Mitochondria was thawed on ice and 25 ug from each sample was prepared for glutamate dehydrogenase assay according to manufacturer instructions (Millipore Sigma MAK099). The absorbance at 450 nm was then measured every two minutes for 4 hours on Cytation 5 (Biotek) in 96-well plate. The data was then imported into R for further analysis. Half-time absorbances were calculated for each sample as a time of the first measurement after half maximum of each sample's absorbance is reached.

4.4.5 *Liver mitochondria treatment with ADP/GTP and cross-linking*

Liver mitochondria was isolated as described in Fezza et al[181]. Briefly, tissue was homogenized in glass homogenizer, cellular debris were cleared by centrifugation at 800 g at 4C and mitochondrial pellet was isolated by centrifugation at 10000g. Mitochondria was washed in isolation buffer and stored in -80C until cross-linking experiments. For treatments and cross-linking experiments mitochondria was thawed on ice and split into pools. Substrates and inhibitors/activators were added as described in **Figure 4.4**. Mitochondria was then cross-linked as described for podocyte and tubule mitochondria cross-linking. Samples were processed and analyzed in similar fashion.

4.5 SUPPLEMENTAL FOR CHAPTER 4

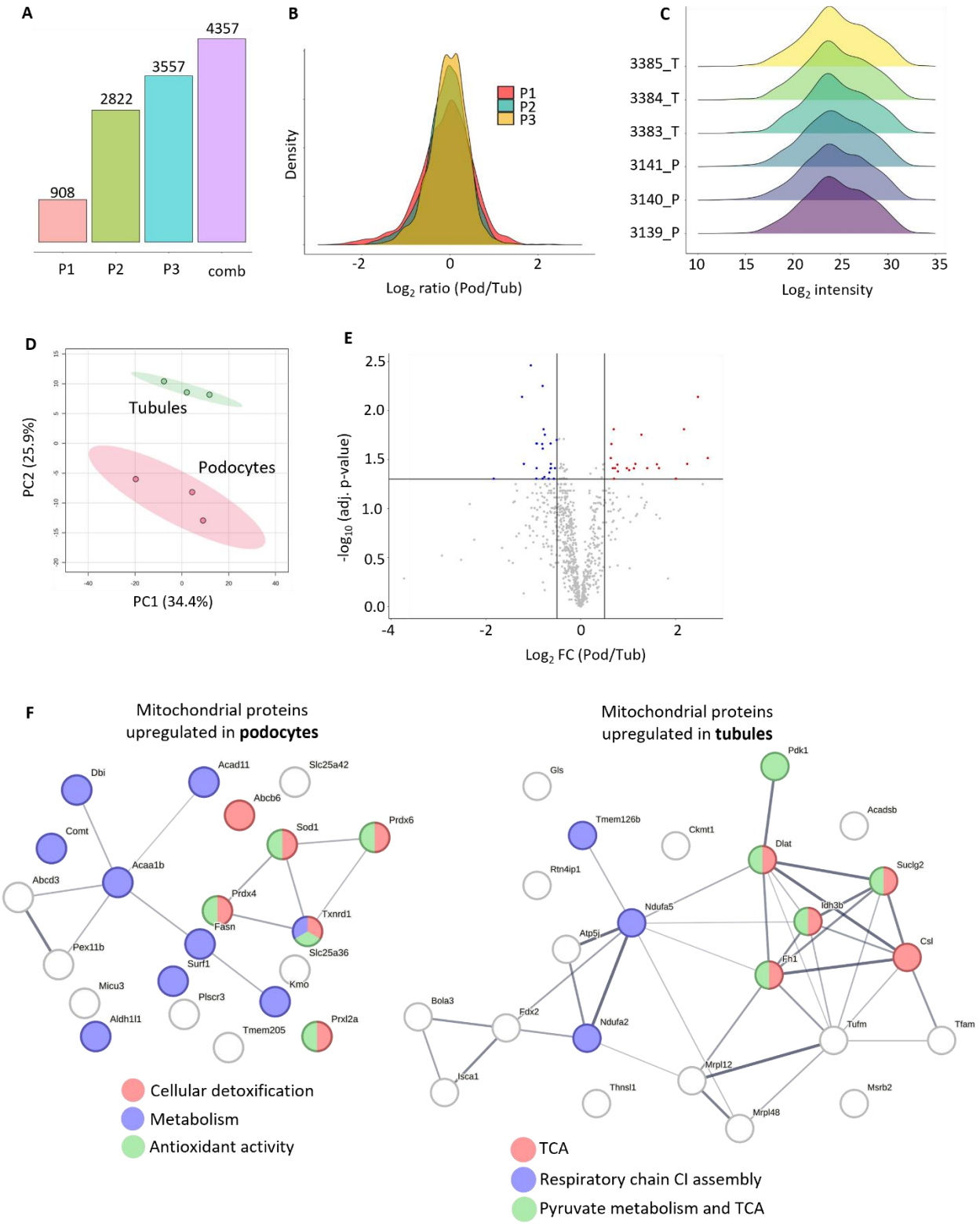

Figure 4.5 Interactome and proteome quantitation in podocyte and tubule cells.

Peptide A	Protein A	Lys A	Peptide B	Protein B	Lys B	Link type	P1	P2	P3	comb
DIKWEFIPSKNLR	VATA_MOUSE	139	VGSHITGGDIYGIVNENSLIKHK	VATA_MOUSE	163	Intra		1.62	1.84	1.77
FKDPVKDGEAK	VATA_MOUSE	591	EHMGEILYKLSSMK	VATA_MOUSE	580	Intra		1.45	1.95	1.81
HKIMLPPR	VATA_MOUSE	165	ALDEYYDKHFTEFVPLR	VATA_MOUSE	467	Intra		1.98	2.38	2.22
HKIMLPPR	VATA_MOUSE	165	DIKWEFIPSKNLR	VATA_MOUSE	139	Intra		1.8	2.37	2.21
HKIMLPPR	VATA_MOUSE	165	WEFIPSKNLR	VATA_MOUSE	139	Intra		1.73	2.32	2.28
HKIM[147.04]LPPR	VATA_MOUSE	165	ALDEYYDKHFTEFVPLR	VATA_MOUSE	467	Intra		2.02	2.38	2.25
HKIM[147.04]LPPR	VATA_MOUSE	165	DIKWEFIPSKNLR	VATA_MOUSE	139	Intra		1.82	2.19	2.13
HKIM[147.04]LPPR	VATA_MOUSE	165	WEFIPSKNLR	VATA_MOUSE	139	Intra		1.95	2.39	2.28
VGSHITGGDIYGIVNENSLIKHKIM[147.04]LPPR	VATA_MOUSE	163	LOOPLINK	VATA_MOUSE	165	Intra	0.95		1.62	1.2
VKCLGNPER	VATA_MOUSE	393	ALDEYYDKHFTEFVPLR	VATA_MOUSE	467	Intra		1.74	2.16	1.92
WEFIPSKNLR	VATA_MOUSE	139	VGSHITGGDIYGIVNENSLIKHK	VATA_MOUSE	163	Intra		1.93	2.28	2.06
IFPKEMLK	VATB2_MOUSE	489	EHMGEILYKLSSMK	VATA_MOUSE	580	1		1.57	1.86	1.64
IFPKEMLK	VATB2_MOUSE	489	FKDPVKDGEAK	VATA_MOUSE	591	1		1.63	2.22	1.89
LM[147.04]KSAIGEGMTR	VATB2_MOUSE	403	KHFPSVNWLISYSK	VATA_MOUSE	443	1		1.92	2.52	2.33
YAEIVHLTLPDGTKR	VATB2_MOUSE	81	QVRPVTEKLPANHPLLTGQR	VATA_MOUSE	220	1		1.56	2.23	2.06
LSKVVKDTTR	VATE1_MOUSE	104	LOOPLINK	VATE1_MOUSE	107	Intra		1.39	1.95	1.58
YAEIVHLTLPDGTKR	VATB2_MOUSE	81	ARDDLITDLLNEAKQR	VATE1_MOUSE	99	1		1.63	2.16	1.94
KTSCEFTGDILR	VATB2_MOUSE	109	LTYKTVSGVNGPLVILDHVK	VATB2_MOUSE	48	Intra		1.6	2.23	2
KTSCEFTGDILR	VATB2_MOUSE	109	YAEIVHLTLPDGTKR	VATB2_MOUSE	81	Intra		1.67	2.33	1.79
VFNGSGKPIDR	VATB2_MOUSE	137	YAEIVHLTLPDGTKR	VATB2_MOUSE	81	Intra	1.45	1.84	2.27	1.89
ENKFIVR	VATC1_MOUSE	245	KNAGSLLTR	VATC1_MOUSE	156	Intra	0.98	1.29		1.02

Figure 4.6 Cross-links from lysosomal proton pump show increase of both intra and intersubunit links in podocytes.

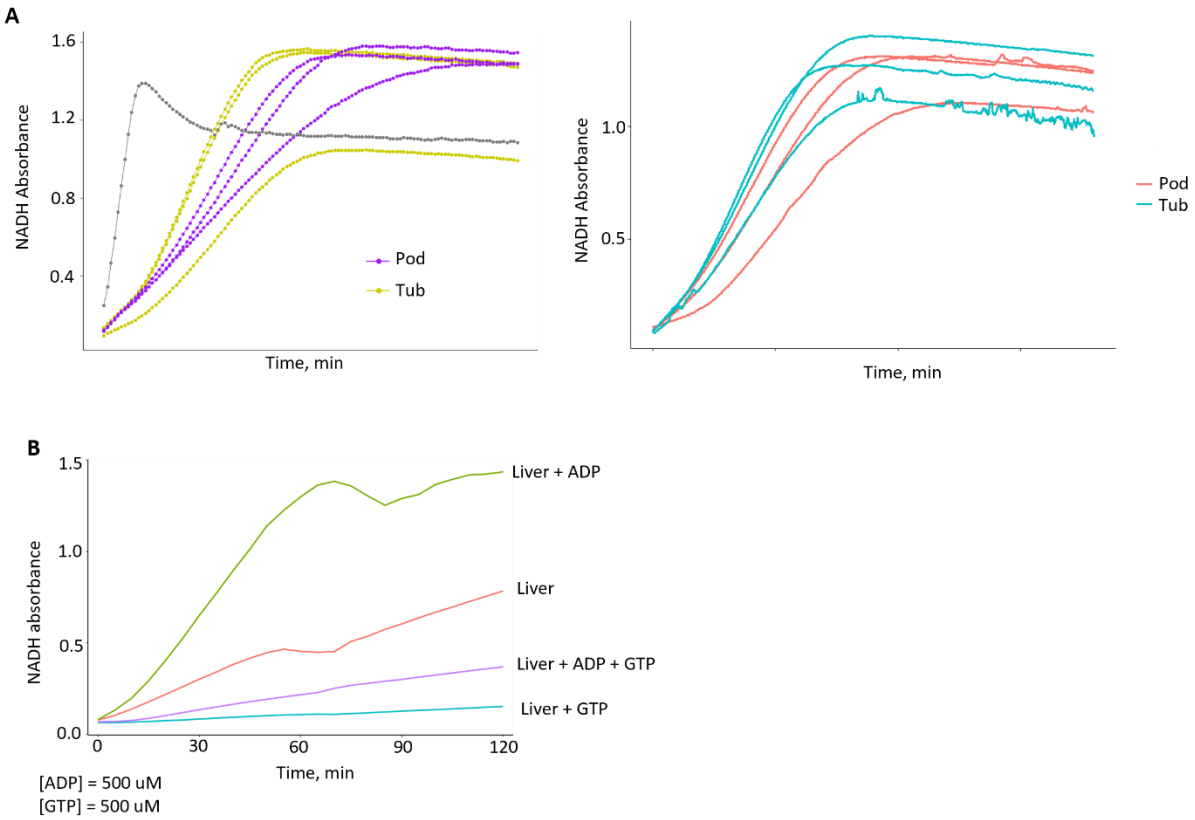

Figure 4.7 Assay to measure DHE3 activity. A. NADH absorbance measured at 450 nm in podocytes and tubules in the mitochondria used for cross-linking experiments (left) and additional samples (right). B. NADH absorbance measured in liver mitochondria after pre-incubation with substrates and addition of DHE3 inhibitor (GTP) and activator (ADP) or a combination of both.

VITA

Anna Bakhtina received her undergraduate degree in Biochemistry from the University of Washington where she was an undergraduate researcher in the Matt Bush's lab. She then worked as a research assistant in the lab of Dr. Sarah Franklin at the University of Utah. She has joined Genome Sciences department at the University of Washington for graduate studies. After rotating in Judit Villen and Mike MacCoss and Brooke Nunn labs she joined Bruce lab for her thesis work.

BIBLIOGRAPHY

1 McGuire, A. L. *et al*. The road ahead in genetics and genomics. *Nat Rev Genet* **21**, 581-596 (2020). https://doi.org/10.1038/s41576-020-0272-6

2 Wang, Z., Gerstein, M. & Snyder, M. RNA-Seq: a revolutionary tool for transcriptomics. *Nat Rev Genet* **10**, 57-63 (2009). https://doi.org/10.1038/nrg2484

3 Zubair, M. *et al*. Proteomics approaches: A review regarding an importance of proteome analyses in understanding the pathogens and diseases. *Front Vet Sci* **9**, 1079359 (2022). https://doi.org/10.3389/fvets.2022.1079359

4 Keenan, E. K., Zachman, D. K. & Hirschey, M. D. Discovering the landscape of protein modifications. *Mol Cell* **81**, 1868-1878 (2021). https://doi.org/10.1016/j.molcel.2021.03.015

5 Han, X. & Gross, R. W. The foundations and development of lipidomics. *J Lipid Res* **63**, 100164 (2022). https://doi.org/10.1016/j.jlr.2021.100164

6 Johnson, C. H., Ivanisevic, J. & Siuzdak, G. Metabolomics: beyond biomarkers and towards mechanisms. *Nat Rev Mol Cell Biol* **17**, 451-459 (2016). https://doi.org/10.1038/nrm.2016.25

7 Bludau, I. & Aebersold, R. Proteomic and interactomic insights into the molecular basis of cell functional diversity. *Nat Rev Mol Cell Biol* **21**, 327-340 (2020). https://doi.org/10.1038/s41580-020-0231-2

8 Elhabashy, H., Merino, F., Alva, V., Kohlbacher, O. & Lupas, A. N. Exploring protein-protein interactions at the proteome level. *Structure* **30**, 462-475 (2022). https://doi.org/10.1016/j.str.2022.02.004

9 Fields, S. & Sternglanz, R. The two-hybrid system: an assay for protein-protein interactions. *Trends Genet* **10**, 286-292 (1994). https://doi.org/10.1016/0168-9525(90)90012-u

10 Colas, P. & Brent, R. The impact of two-hybrid and related methods on biotechnology. *Trends Biotechnol* **16**, 355-363 (1998). https://doi.org/10.1016/s0167-7799(98)01225-6

11 Hamdi, A. & Colas, P. Yeast two-hybrid methods and their applications in drug discovery. *Trends Pharmacol Sci* **33**, 109-118 (2012). https://doi.org/10.1016/j.tips.2011.10.008

12 Lin, J. S. & Lai, E. M. Protein-Protein Interactions: Co-Immunoprecipitation. *Methods Mol Biol* **1615**, 211-219 (2017). https://doi.org/10.1007/978-1-4939-7033-9_17

13 Free, R. B., Hazelwood, L. A. & Sibley, D. R. Identifying novel protein-protein interactions using co-immunoprecipitation and mass spectroscopy. *Curr Protoc Neurosci* **Chapter 5**, Unit 5.28 (2009). https://doi.org/10.1002/0471142301.ns0528s46

14 Gnanasekaran, P. & Pappu, H. R. Affinity Purification-Mass Spectroscopy (AP-MS) and Co-Immunoprecipitation (Co-IP) Technique to Study Protein-Protein Interactions. *Methods Mol Biol* **2690**, 81-85 (2023). https://doi.org/10.1007/978-1-0716-3327-4_7

15 Gingras, A. C., Gstaiger, M., Raught, B. & Aebersold, R. Analysis of protein complexes using mass spectrometry. *Nat Rev Mol Cell Biol* **8**, 645-654 (2007). https://doi.org/10.1038/nrm2208

16 Meyer, K. & Selbach, M. Quantitative affinity purification mass spectrometry: a versatile technology to study protein-protein interactions. *Front Genet* **6**, 237 (2015). https://doi.org/10.3389/fgene.2015.00237

17 Huttlin, E. L. *et al*. Dual proteome-scale networks reveal cell-specific remodeling of the human interactome. *Cell* **184**, 3022-3040.e3028 (2021). https://doi.org/10.1016/j.cell.2021.04.011

18 Huttlin, E. L. *et al*. The BioPlex Network: A Systematic Exploration of the Human Interactome. *Cell* **162**, 425-440 (2015). https://doi.org/10.1016/j.cell.2015.06.043

19 Huttlin, E. L. *et al*. Architecture of the human interactome defines protein communities and disease networks. *Nature* **545**, 505-509 (2017). https://doi.org/10.1038/nature22366

20 Qin, W., Cho, K. F., Cavanagh, P. E. & Ting, A. Y. Deciphering molecular interactions by proximity labeling. *Nat Methods* **18**, 133-143 (2021). https://doi.org/10.1038/s41592-020-01010-5

21 Zhai, Y. *et al*. Spatiotemporal-resolved protein networks profiling with photoactivation dependent proximity labeling. *Nat Commun* **13**, 4906 (2022). https://doi.org/10.1038/s41467-022-32689-z

22 Qin, W. *et al*. Dynamic mapping of proteome trafficking within and between living cells by TransitID. *Cell* **186**, 3307-3324.e3330 (2023). https://doi.org/10.1016/j.cell.2023.05.044

23 Qin, W., Myers, S. A., Carey, D. K., Carr, S. A. & Ting, A. Y. Spatiotemporally-resolved mapping of RNA binding proteins via functional proximity labeling reveals a mitochondrial mRNA anchor promoting stress recovery. *Nat Commun* **12**, 4980 (2021). https://doi.org/10.1038/s41467-021-25259-2

24 Malinovska, L. *et al.* Proteome-wide structural changes measured with limited proteolysis-mass spectrometry: an advanced protocol for high-throughput applications. *Nat Protoc* **18**, 659-682 (2023). https://doi.org/10.1038/s41596-022-00771-x

25 Johnson, D. T., Di Stefano, L. H. & Jones, L. M. Fast photochemical oxidation of proteins (FPOP): A powerful mass spectrometry-based structural proteomics tool. *J Biol Chem* **294**, 11969-11979 (2019). https://doi.org/10.1074/jbc.REV119.006218

26 James, E. I., Murphree, T. A., Vorauer, C., Engen, J. R. & Guttman, M. Advances in Hydrogen/Deuterium Exchange Mass Spectrometry and the Pursuit of Challenging Biological Systems. *Chem Rev* **122**, 7562-7623 (2022). https://doi.org/10.1021/acs.chemrev.1c00279

27 Lin, X., Zmyslowski, A. M., Gagnon, I. A., Nakamoto, R. K. & Sosnick, T. R. Development of in vivo HDX-MS with applications to a TonB-dependent transporter and other proteins. *Protein Sci* **31**, e4402 (2022). https://doi.org/10.1002/pro.4402

28 Espino, J. A., King, C. D., Jones, L. M. & Robinson, R. A. S. Fast Photochemical Oxidation of Proteins Using Enhanced Multiplexing Proteomics. *Anal Chem* **92**, 7596-7603 (2020). https://doi.org/10.1021/acs.analchem.0c00174

29 Tang, X., Wippel, H. H., Chavez, J. D. & Bruce, J. E. Crosslinking mass spectrometry: A link between structural biology and systems biology. *Protein Sci* **30**, 773-784 (2021). https://doi.org/10.1002/pro.4045

30 Mohr, J. P., Caudal, A., Tian, R. & Bruce, J. E. Multidimensional Cross-Linking and Real-Time Informatics for Multiprotein Interaction Studies. *J Proteome Res* **23**, 107-116 (2024). https://doi.org/10.1021/acs.jproteome.3c00455

31 Leitner, A. *et al.* Chemical cross-linking/mass spectrometry targeting acidic residues in proteins and protein complexes. *Proc Natl Acad Sci U S A* **111**, 9455-9460 (2014). https://doi.org/10.1073/pnas.1320298111

32 Jones, A. X. *et al.* Improving mass spectrometry analysis of protein structures with arginine-selective chemical cross-linkers. *Nat Commun* **10**, 3911 (2019). https://doi.org/10.1038/s41467-019-11917-z

33 Huang, R. *et al.* A novel mass spectrometry-cleavable, phosphate-based enrichable and multi-targeting protein cross-linker. *Chem Sci* **10**, 6443-6447 (2019). https://doi.org/10.1039/c9sc00893d

34 Iacobucci, C., Piotrowski, C., Rehkamp, A., Ihling, C. H. & Sinz, A. The First MS-Cleavable, Photo-Thiol-Reactive Cross-Linker for Protein Structural Studies. *J Am Soc Mass Spectrom* **30**, 139-148 (2019). https://doi.org/10.1007/s13361-018-1952-8

35 Tang, X., Munske, G. R., Siems, W. F. & Bruce, J. E. Mass Spectrometry Identifiable Cross-Linking Strategy for Studying Protein−Protein Interactions. *Anal. Chem.* **77**, 311-318 (2005). https://doi.org/10.1021/ac0488762

36 Chavez, J. D. & Bruce, J. E. Chemical cross-linking with mass spectrometry: a tool for systems structural biology. *Curr Opin Chem Biol* **48**, 8-18 (2019). https://doi.org/10.1016/j.cbpa.2018.08.006

37 Jiang, P. L. *et al.* A Membrane-Permeable and Immobilized Metal Affinity Chromatography (IMAC) Enrichable Cross-Linking Reagent to Advance In Vivo Cross-Linking Mass Spectrometry. *Angew Chem Int Ed Engl* **61**, e202113937 (2022). https://doi.org/10.1002/anie.202113937

38 Steigenberger, B., Pieters, R. J., Heck, A. J. R. & Scheltema, R. A. PhoX: An IMAC-Enrichable Cross-Linking Reagent. *ACS Cent. Sci.* **5**, 1514-1522 (2019). https://doi.org/10.1021/acscentsci.9b00416

39 Klykov, O. *et al.* Efficient and robust proteome-wide approaches for cross-linking mass spectrometry. *Nature Protocols* **13**, 2964-2990 (2018). https://doi.org/10.1038/s41596-018-0074-x

40 Leitner, A., Faini, M., Stengel, F. & Aebersold, R. Crosslinking and Mass Spectrometry: An Integrated Technology to Understand the Structure and Function of Molecular Machines. *Trends Biochem Sci* **41**, 20-32 (2016). https://doi.org/10.1016/j.tibs.2015.10.008

41 Keller, A., Tang, X. & Bruce, J. E. Integrated Analysis of Cross-Links and Dead-End Peptides for Enhanced Interpretation of Quantitative XL-MS. *J Proteome Res* **22**, 2900-2908 (2023). https://doi.org/10.1021/acs.jproteome.3c00191

42 Weisbrod, C. R. *et al.* In vivo protein interaction network identified with a novel real-time cross-linked peptide identification strategy. *J. Proteome Res.* **12**, 1569-1579 (2013). https://doi.org/10.1021/pr3011638

43 Kolbowski, L., Fischer, L. & Rappsilber, J. Cleavable Cross-Linkers Redefined by a Novel MS. *Anal Chem* **95**, 15461-15464 (2023). https://doi.org/10.1021/acs.analchem.3c01673

44 Tang, X. & Bruce, J. E. A new cross-linking strategy: protein interaction reporter (PIR) technology for protein-protein interaction studies. *Mol Biosyst* **6**, 939-947 (2010). https://doi.org/10.1039/b920876c

45 Götze, M., Iacobucci, C., Ihling, C. H. & Sinz, A. A Simple Cross-Linking/Mass Spectrometry Workflow for Studying System-wide Protein Interactions. *Anal Chem* **91**, 10236-10244 (2019). https://doi.org/10.1021/acs.analchem.9b02372

46 Mohr, J. P., Perumalla, P., Chavez, J. D., Eng, J. K. & Bruce, J. E. Mango: A General Tool for Collision Induced Dissociation-Cleavable Cross-Linked Peptide Identification. *Anal. Chem.* **90**, 6028-6034 (2018). https://doi.org/10.1021/acs.analchem.7b04991

47 Eng, J. K. *et al.* A Deeper Look into Comet—Implementation and Features. *J. Am. Soc. Mass Spectrom.* **26**, 1865-1874 (2015). https://doi.org/10.1007/s13361-015-1179-x

48 Keller, A., Chavez, J. D. & Bruce, J. E. Increased sensitivity with automated validation of XL-MS cleavable peptide crosslinks. *Bioinformatics* **35**, 895-897 (2019). https://doi.org/10.1093/bioinformatics/bty720

49 Zhang, H. *et al.* In vivo identification of the outer membrane protein OmcA-MtrC interaction network in Shewanella oneidensis MR-1 cells using novel hydrophobic chemical cross-linkers. *J. Proteome Res.* **7**, 1712-1720 (2008). https://doi.org/10.1021/pr7007658

50 Chavez, J. D. *et al.* Cross-linking measurements of the Potato leafroll virus reveal protein interaction topologies required for virion stability, aphid transmission, and virus-plant interactions. *J. Proteome Res.* **11**, 2968-2981 (2012). https://doi.org/10.1021/pr300041t

51 Chavez, J. D. *et al.* Quantitative interactome analysis reveals a chemoresistant edgotype. *Nature Communications* **6**, 7928 (2015). https://doi.org/10.1038/ncomms8928

52 Schweppe, D. K. *et al.* Host-Microbe Protein Interactions during Bacterial Infection. *Chem. Biol.* **22**, 1521-1530 (2015). https://doi.org/10.1016/j.chembiol.2015.09.015

53 Schweppe, D. K. *et al.* Mitochondrial protein interactome elucidated by chemical cross-linking mass spectrometry. *Proc Natl Acad Sci USA* **114**, 1732-1737 (2017). https://doi.org/10.1073/pnas.1617220114

54 Wheat, A. *et al.* Protein interaction landscapes revealed by advanced in vivo cross-linking-mass spectrometry. *Proc Natl Acad Sci U S A* **118** (2021). https://doi.org/10.1073/pnas.2023360118

55 Wippel, H. H., Chavez, J. D., Tang, X. & Bruce, J. E. Quantitative interactome analysis with chemical cross-linking and mass spectrometry. *Curr Opin Chem Biol* **66**, 102076 (2022). https://doi.org/10.1016/j.cbpa.2021.06.011

56 Chavez, J. D., Keller, A., Zhou, B., Tian, R. & Bruce, J. E. Cellular Interactome Dynamics during Paclitaxel Treatment. *Cell Rep* **29**, 2371-2383.e2375 (2019). https://doi.org/10.1016/j.celrep.2019.10.063

57 Zhong, X. *et al.* Large-Scale and Targeted Quantitative Cross-Linking MS Using Isotope-Labeled Protein Interaction Reporter (PIR) Cross-Linkers. *J. Proteome Res.* **16**, 720-727 (2017). https://doi.org/10.1021/acs.jproteome.6b00752

58 Makepeace, K. A. T. *et al.* Improving Identification of In-organello Protein-Protein Interactions Using an Affinity-enrichable, Isotopically Coded, and Mass Spectrometry-cleavable Chemical Crosslinker. *Molecular & Cellular Proteomics* **19**, 624-639 (2020). https://doi.org/10.1074/mcp.RA119.001839

59 Chavez, J. D. *et al.* A General Method for Targeted Quantitative Cross-Linking Mass Spectrometry. *PLoS ONE* **11**, e0167547 (2016). https://doi.org/10.1371/journal.pone.0167547

60 Yu, C. *et al.* Developing a Multiplexed Quantitative Cross-Linking Mass Spectrometry Platform for Comparative Structural Analysis of Protein Complexes. *Anal. Chem.* **88**, 10301-10308 (2016). https://doi.org/10.1021/acs.analchem.6b03148

61 Chu, F. *et al.* Allosteric Regulation of Rod Photoreceptor Phosphodiesterase 6 (PDE6) Elucidated by Chemical Cross-Linking and Quantitative Mass Spectrometry. *J Mol Biol* **431**, 3677-3689 (2019). https://doi.org/10.1016/j.jmb.2019.07.035

62 Müller, F., Kolbowski, L., Bernhardt, O. M., Reiter, L. & Rappsilber, J. Data-independent Acquisition Improves Quantitative Cross-linking Mass Spectrometry. *Mol Cell Proteomics* **18**, 786-795 (2019). https://doi.org/10.1074/mcp.TIR118.001276

63 Chavez, J. D., Keller, A., Mohr, J. P. & Bruce, J. E. Isobaric Quantitative Protein Interaction Reporter Technology for Comparative Interactome Studies. *Anal. Chem.*, acs.analchem.0c03128 (2020). https://doi.org/10.1021/acs.analchem.0c03128

64 Ruwolt, M. *et al.* Optimized TMT-Based Quantitative Cross-Linking Mass Spectrometry Strategy for Large-Scale Interactomic Studies. *Anal Chem* **94**, 5265-5272 (2022). https://doi.org/10.1021/acs.analchem.1c04812

65 Yu, C., Wang, X. & Huang, L. Developing a Targeted Quantitative Strategy for Sulfoxide-Containing MS-Cleavable Cross-Linked Peptides to Probe Conformational Dynamics of Protein Complexes. *Anal Chem* **94**, 4390-4398 (2022). https://doi.org/10.1021/acs.analchem.1c05298

66 Milenkovic, D. *et al.* Preserved respiratory chain capacity and physiology in mice with profoundly reduced levels of mitochondrial respirasomes. *Cell Metab* **35**, 1799-1813.e1797 (2023). https://doi.org/10.1016/j.cmet.2023.07.015

67 Hao, Y. *et al.* 4D-diaXLMS: Proteome-wide Four-Dimensional Data-Independent Acquisition Workflow for Cross-Linking Mass Spectrometry. *Anal Chem* **95**, 14077-14085 (2023). https://doi.org/10.1021/acs.analchem.3c02824

68 Chavez, J. D., Keller, A., Wippel, H. H., Mohr, J. P. & Bruce, J. E. Multiplexed Cross-Linking with Isobaric Quantitative Protein Interaction Reporter Technology. *Anal Chem* **93**, 16759-16768 (2021). https://doi.org/10.1021/acs.analchem.1c02209

69 Wippel, H. H., Chavez, J. D., Keller, A. D. & Bruce, J. E. Multiplexed Isobaric Quantitative Cross-Linking Reveals Drug-Induced Interactome Changes in Breast Cancer Cells. *Anal Chem* **94**, 2713-2722 (2022). https://doi.org/10.1021/acs.analchem.1c02208

70 Chavez, J. D., Keller, A., Mohr, J. P. & Bruce, J. E. Isobaric Quantitative Protein Interaction Reporter Technology for Comparative Interactome Studies. *Anal Chem* **92**, 14094-14102 (2020). https://doi.org/10.1021/acs.analchem.0c03128

71 López-Otín, C., Blasco, M. A., Partridge, L., Serrano, M. & Kroemer, G. The hallmarks of aging. *Cell* **153**, 1194-1217 (2013). https://doi.org/10.1016/j.cell.2013.05.039

72 Harman, D. Aging: a theory based on free radical and radiation chemistry. *J Gerontol* **11**, 298-300 (1956). https://doi.org/10.1093/geronj/11.3.298

73 Peterson, C. M., Johannsen, D. L. & Ravussin, E. Skeletal Muscle Mitochondria and Aging: A Review. *Journal of Aging Research* **2012**, 1-20 (2012). https://doi.org/10.1155/2012/194821

74 Sun, N., Youle, R. J. & Finkel, T. The Mitochondrial Basis of Aging. *Mol Cell* **61**, 654-666 (2016). https://doi.org/10.1016/j.molcel.2016.01.028

75 Short, K. R. *et al.* Decline in skeletal muscle mitochondrial function with aging in humans. *Proc Natl Acad Sci USA* **102**, 5618-5623 (2005). https://doi.org/10.1073/pnas.0501559102

76 Hepple, R. T. Mitochondrial Involvement and Impact in Aging Skeletal Muscle. *Front. Aging Neurosci.* **6** (2014). https://doi.org/10.3389/fnagi.2014.00211

77 Ubaida-Mohien, C. *et al.* Discovery proteomics in aging human skeletal muscle finds change in spliceosome, immunity, proteostasis and mitochondria. *eLife* **8**, e49874 (2019). https://doi.org/10.7554/eLife.49874

78 Tumasian, R. A. *et al.* Skeletal muscle transcriptome in healthy aging. *Nature Communications* **12**, 2014 (2021). https://doi.org/10.1038/s41467-021-22168-2

79 Hwang, C. Y. *et al.* Quantitative proteome analysis of age-related changes in mouse gastrocnemius muscle using mTRAQ. *Proteomics* **14**, 121-132 (2014). https://doi.org/10.1002/pmic.201200497

80 Hunt, L. C. *et al.* Integrated genomic and proteomic analyses identify stimulus-dependent molecular changes associated with distinct modes of skeletal muscle atrophy. *Cell Rep* **37**, 109971 (2021). https://doi.org/10.1016/j.celrep.2021.109971

81 Yu, Q. *et al.* Sample multiplexing for targeted pathway proteomics in aging mice. *Proc Natl Acad Sci USA* **117**, 9723-9732 (2020). https://doi.org/10.1073/pnas.1919410117

82 Yeo, D., Kang, C. & Ji, L. L. Aging alters acetylation status in skeletal and cardiac muscles. *GeroScience* **42**, 963-976 (2020). https://doi.org/10.1007/s11357-020-00171-7

83 Wagner, G. R. & Payne, R. M. Mitochondrial Acetylation and Diseases of Aging. *Journal of Aging Research* **2011**, 1-13 (2011). https://doi.org/10.4061/2011/234875

84 Hofer, A. & Wenz, T. Post-translational modification of mitochondria as a novel mode of regulation. *Experimental Gerontology* **56**, 202-220 (2014). https://doi.org/10.1016/j.exger.2014.03.006

85 Müller, F. & Rappsilber, J. A protocol for studying structural dynamics of proteins by quantitative crosslinking mass spectrometry and data-independent acquisition. *Journal of Proteomics* **218**, 103721 (2020). https://doi.org/10.1016/j.jprot.2020.103721

86 Jumper, J. *et al.* Highly accurate protein structure prediction with AlphaFold. *Nature* **596**, 583-589 (2021). https://doi.org/10.1038/s41586-021-03819-2

87 Rath, S. *et al.* MitoCarta3.0: an updated mitochondrial proteome now with sub-organelle localization and pathway annotations. *Nucleic Acids Res* **49**, D1541-D1547 (2021). https://doi.org/10.1093/nar/gkaa1011

88 Figueiredo, P. A., Ferreira, R. M., Appell, H. J. & Duarte, J. A. Age-induced morphological, biochemical, and functional alterations in isolated mitochondria from murine skeletal muscle. *J Gerontol A Biol Sci Med Sci* **63**, 350-359 (2008). https://doi.org/10.1093/gerona/63.4.350

89 Han, Y. *et al.* Transcriptome features of striated muscle aging and predictability of protein level changes. *Mol. Omics* **17**, 796-808 (2021). https://doi.org/10.1039/D1MO00178G

90 Wiley, C. D. & Campisi, J. The metabolic roots of senescence: mechanisms and opportunities for intervention. *Nat Metab* **3**, 1290-1301 (2021). https://doi.org/10.1038/s42255-021-00483-8

91 Sánchez-Caballero, L., Guerrero-Castillo, S. & Nijtmans, L. Unraveling the complexity of mitochondrial complex I assembly: A dynamic process. *Biochimica et Biophysica Acta (BBA) - Bioenergetics* **1857**, 980-990 (2016). https://doi.org/10.1016/j.bbabio.2016.03.031

92 Kruse, S. E. *et al.* Age modifies respiratory complex I and protein homeostasis in a muscle type-specific manner. *Aging Cell* **15**, 89-99 (2016). https://doi.org/10.1111/acel.12412

93 Park, J. *et al.* SIRT5-Mediated Lysine Desuccinylation Impacts Diverse Metabolic Pathways. *Molecular Cell* **50**, 919-930 (2013). https://doi.org/10.1016/j.molcel.2013.06.001

94 Yang, W. *et al.* Mitochondrial Sirtuin Network Reveals Dynamic SIRT3-Dependent Deacetylation in Response to Membrane Depolarization. *Cell* **167**, 985-1000.e1021 (2016). https://doi.org/10.1016/j.cell.2016.10.016

95 Guerrero-Castillo, S. *et al.* The Assembly Pathway of Mitochondrial Respiratory Chain Complex I. *Cell Metabolism* **25**, 128-139 (2017). https://doi.org/10.1016/j.cmet.2016.09.002

96 Hirst, J. & Roessler, M. M. Energy conversion, redox catalysis and generation of reactive oxygen species by respiratory complex I. *Biochim Biophys Acta* **1857**, 872-883 (2016). https://doi.org/10.1016/j.bbabio.2015.12.009

97 Szczepanowska, K. *et al.* A salvage pathway maintains highly functional respiratory complex I. *Nat Commun* **11**, 1643 (2020). https://doi.org/10.1038/s41467-020-15467-7

98 Miwa, S. *et al.* Low abundance of the matrix arm of complex I in mitochondria predicts longevity in mice. *Nature Communications* **5**, 3837 (2014). https://doi.org/10.1038/ncomms4837

99 Protasoni, M. *et al.* Respiratory supercomplexes act as a platform for complex III - mediated maturation of human mitochondrial complexes I and IV. *EMBO J* **39** (2020). https://doi.org/10.15252/embj.2019102817

100 Balsa, E. *et al.* NDUFA4 Is a Subunit of Complex IV of the Mammalian Electron Transport Chain. *Cell Metabolism* **16**, 378-386 (2012). https://doi.org/10.1016/j.cmet.2012.07.015

101 Zong, S. *et al.* Structure of the intact 14-subunit human cytochrome c oxidase. *Cell Res* **28**, 1026-1034 (2018). https://doi.org/10.1038/s41422-018-0071-1

102 Caudal, A. *et al.* Mitochondrial interactome quantitation reveals structural changes in metabolic machinery in the failing murine heart. *Nat Cardiovasc Res* **1**, 855-866 (2022). https://doi.org/10.1038/s44161-022-00127-4

103 Clayton, S. A. *et al.* Inflammation causes remodeling of mitochondrial cytochrome. *Sci Adv* **7**, eabl5182 (2021). https://doi.org/10.1126/sciadv.abl5182

104 Pitceathly, Robert D. S. *et al.* NDUFA4 Mutations Underlie Dysfunction of a Cytochrome c Oxidase Subunit Linked to Human Neurological Disease. *Cell Rep* **3**, 1795-1805 (2013). https://doi.org/10.1016/j.celrep.2013.05.005

105 Yuan, R. *et al.* Genetic coregulation of age of female sexual maturation and lifespan through circulating IGF1 among inbred mouse strains. *Proc Natl Acad Sci U S A* **109**, 8224-8229 (2012). https://doi.org/10.1073/pnas.1121113109

106 Ferrucci, L. & Kuchel, G. A. Heterogeneity of Aging: Individual Risk Factors, Mechanisms, Patient Priorities, and Outcomes. *J Am Geriatr Soc* **69**, 610-612 (2021). https://doi.org/10.1111/jgs.17011

107 Smith, H. Q., Li, C., Stanley, C. A. & Smith, T. J. Glutamate Dehydrogenase, a Complex Enzyme at a Crucial Metabolic Branch Point. *Neurochem Res* **44**, 117-132 (2019). https://doi.org/10.1007/s11064-017-2428-0

108 Hamelin, M., Mary, J., Vostry, M., Friguet, B. & Bakala, H. Glycation damage targets glutamate dehydrogenase in the rat liver mitochondrial matrix during aging: Glycation of glutamate dehydrogenase with aging. *FEBS Journal* **274**, 5949-5961 (2007). https://doi.org/10.1111/j.1742-4658.2007.06118.x

109 Li, M., Li, C., Allen, A., Stanley, C. A. & Smith, T. J. The structure and allosteric regulation of mammalian glutamate dehydrogenase. *Archives of Biochemistry and Biophysics* **519**, 69-80 (2012). https://doi.org/10.1016/j.abb.2011.10.015

110 Banerjee, S., Schmidt, T., Fang, J., Stanley, C. A. & Smith, T. J. Structural Studies on ADP Activation of Mammalian Glutamate Dehydrogenase and the Evolution of Regulation [,]. *Biochemistry* **42**, 3446-3456 (2003). https://doi.org/10.1021/bi0206917

111 Hyyti, O. M., Ledee, D., Ning, X.-H., Ge, M. & Portman, M. A. Aging impairs myocardial fatty acid and ketone oxidation and modifies cardiac functional and metabolic responses to insulin in mice. *American Journal of Physiology-Heart and Circulatory Physiology* **299**, H868-H875 (2010). https://doi.org/10.1152/ajpheart.00931.2009

112 Houtkooper, R. H. *et al.* The metabolic footprint of aging in mice. *Sci Rep* **1**, 134 (2011). https://doi.org/10.1038/srep00134

113 Zhang, X. *et al.* Impaired Mitochondrial Energetics Characterize Poor Early Recovery of Muscle Mass Following Hind Limb Unloading in Old Mice. *The Journals of Gerontology: Series A* **73**, 1313-1322 (2018). https://doi.org/10.1093/gerona/gly051

114 Fan, J. *et al.* Tetrameric Acetyl-CoA Acetyltransferase 1 Is Important for Tumor Growth. *Molecular Cell* **64**, 859-874 (2016). https://doi.org/10.1016/j.molcel.2016.10.014

115 Wu, B. *et al.* Succinyl-CoA Ligase Deficiency in Pro-inflammatory and Tissue-Invasive T Cells. *Cell Metabolism* **32**, 967-980.e965 (2020). https://doi.org/10.1016/j.cmet.2020.10.025

116 Hayflick, L. The greatest risk factor for the leading cause of death is ignored. *Biogerontology* **22**, 133-141 (2021). https://doi.org/10.1007/s10522-020-09901-y

117 Asadi Shahmirzadi, A. *et al.* Alpha-Ketoglutarate, an Endogenous Metabolite, Extends Lifespan and Compresses Morbidity in Aging Mice. *Cell Metabolism* **32**, 447-456.e446 (2020). https://doi.org/10.1016/j.cmet.2020.08.004

118 Su, Y. *et al.* Alpha-ketoglutarate extends Drosophila lifespan by inhibiting mTOR and activating AMPK. *Aging* **11**, 4183-4197 (2019). https://doi.org/10.18632/aging.102045

119 Kaeberlein, M., Burtner, C. R. & Kennedy, B. K. Recent Developments in Yeast Aging. *PLoS Genet* **3**, e84 (2007). https://doi.org/10.1371/journal.pgen.0030084

120 Chin, R. M. *et al.* The metabolite α-ketoglutarate extends lifespan by inhibiting ATP synthase and TOR. *Nature* **510**, 397-401 (2014). https://doi.org/10.1038/nature13264

121 Hagopian, K. Caloric restriction increases gluconeogenic and transaminase enzyme activities in mouse liver. *Experimental Gerontology* **38**, 267-278 (2003). https://doi.org/10.1016/S0531-5565(02)00202-4

122 Lyu, Y. *et al.* Drosophila serotonin 2A receptor signaling coordinates central metabolic processes to modulate aging in response to nutrient choice. *eLife* **10**, e59399 (2021). https://doi.org/10.7554/eLife.59399

123 Lombardi, A. A. *et al.* Mitochondrial calcium exchange links metabolism with the epigenome to control cellular differentiation. *Nature Communications* **10**, 4509 (2019). https://doi.org/10.1038/s41467-019-12103-x

124 Rardin, M. J. *et al.* Label-free quantitative proteomics of the lysine acetylome in mitochondria identifies substrates of SIRT3 in metabolic pathways. *Proc Natl Acad Sci USA* **110**, 6601-6606 (2013). https://doi.org/10.1073/pnas.1302961110

125 Mimaki, M., Wang, X., McKenzie, M., Thorburn, D. R. & Ryan, M. T. Understanding mitochondrial complex I assembly in health and disease. *Biochim Biophys Acta* **1817**, 851-862 (2012). https://doi.org/10.1016/j.bbabio.2011.08.010

126 Martínez-Reyes, I. & Chandel, N. S. Mitochondrial TCA cycle metabolites control physiology and disease. *Nat Commun* **11**, 102 (2020). https://doi.org/10.1038/s41467-019-13668-3

127 Lee, S.-H., Lee, S.-K., Paik, D. & Min, K.-J. Overexpression of Fatty-Acid- β -Oxidation-Related Genes Extends the Lifespan of Drosophila melanogaster. *Oxidative Medicine and Cellular Longevity* **2012**, 1-8 (2012). https://doi.org/10.1155/2012/854502

128 Nguyen, D., Samson, S. L., Reddy, V. T., Gonzalez, E. V. & Sekhar, R. V. Impaired mitochondrial fatty acid oxidation and insulin resistance in aging: novel protective role of glutathione. *Aging Cell* **12**, 415-425 (2013). https://doi.org/10.1111/acel.12073

129 Keller, A., Chavez, J. D., Eng, J. K., Thornton, Z. & Bruce, J. E. Tools for 3D Interactome Visualization. *J. Proteome Res.* **18**, 753-758 (2019). https://doi.org/10.1021/acs.jproteome.8b00703

130 Lark, D. S. *et al.* Direct real-time quantification of mitochondrial oxidative phosphorylation efficiency in permeabilized skeletal muscle myofibers. *Am J Physiol Cell Physiol* **311**, C239-245 (2016). https://doi.org/10.1152/ajpcell.00124.2016

131 Figueiredo, P. A., Ferreira, R. M., Appell, H. J. & Duarte, J. A. Age-induced morphological, biochemical, and functional alterations in isolated mitochondria from murine skeletal muscle. *The Journals of Gerontology. Series A, Biological Sciences and Medical Sciences* **63**, 350-359 (2008). https://doi.org/10.1093/gerona/63.4.350

132 Crouch, M.-L. *et al.* Cyclophosphamide leads to persistent deficits in physical performance and in vivo mitochondria function in a mouse model of chemotherapy late effects. *PLoS ONE* **12**, e0181086 (2017). https://doi.org/10.1371/journal.pone.0181086

133 Wickham, H. *et al.* Welcome to the Tidyverse. *JOSS* **4**, 1686 (2019). https://doi.org/10.21105/joss.01686

134 Kaur, G. & Dufour, J. M. Cell lines: Valuable tools or useless artifacts. *Spermatogenesis* **2**, 1-5 (2012). https://doi.org/10.4161/spmg.19885

135 Geiger, T., Wehner, A., Schaab, C., Cox, J. & Mann, M. Comparative proteomic analysis of eleven common cell lines reveals ubiquitous but varying expression of most proteins. *Mol Cell Proteomics* **11**, M111.014050 (2012). https://doi.org/10.1074/mcp.M111.014050

136 Burkard, T. R. *et al.* Initial characterization of the human central proteome. *BMC Syst Biol* **5**, 17 (2011). https://doi.org/10.1186/1752-0509-5-17

137 Lundberg, E. *et al.* Defining the transcriptome and proteome in three functionally different human cell lines. *Mol Syst Biol* **6**, 450 (2010). https://doi.org/10.1038/msb.2010.106

138 Havugimana, P. C. *et al.* A census of human soluble protein complexes. *Cell* **150**, 1068-1081 (2012). https://doi.org/10.1016/j.cell.2012.08.011

139 Holding, A. N. XL-MS: Protein cross-linking coupled with mass spectrometry. *Methods* **89**, 54-63 (2015). https://doi.org/10.1016/j.ymeth.2015.06.010

140 O'Reilly, F. J. & Rappsilber, J. Cross-linking mass spectrometry: methods and applications in structural, molecular and systems biology. *Nat Struct Mol Biol* **25**, 1000-1008 (2018). https://doi.org/10.1038/s41594-018-0147-0

141 Schmidt, C. & Urlaub, H. Combining cryo-electron microscopy (cryo-EM) and cross-linking mass spectrometry (CX-MS) for structural elucidation of large protein assemblies. *Current Opinion in Structural Biology* **46**, 157-168 (2017). https://doi.org/10.1016/j.sbi.2017.10.005

142 Burke, D. F. *et al.* Towards a structurally resolved human protein interaction network. *Nat Struct Mol Biol* **30**, 216-225 (2023). https://doi.org/10.1038/s41594-022-00910-8

143 Bakhtina, A. A. *et al.* Skeletal muscle mitochondrial interactome remodeling is linked to functional decline in aged female mice. *Nat Aging* **3**, 313-326 (2023). https://doi.org/10.1038/s43587-023-00366-5

144 Karantza, V. Keratins in health and cancer: more than mere epithelial cell markers. *Oncogene* **30**, 127-138 (2011). https://doi.org/10.1038/onc.2010.456

145 Schweizer, J. *et al.* New consensus nomenclature for mammalian keratins. *J Cell Biol* **174**, 169-174 (2006). https://doi.org/10.1083/jcb.200603161

146 Savitski, M. M. *et al.* Measuring and managing ratio compression for accurate iTRAQ/TMT quantification. *J Proteome Res* **12**, 3586-3598 (2013). https://doi.org/10.1021/pr400098r

147 Hentze, M. W., Castello, A., Schwarzl, T. & Preiss, T. A brave new world of RNA-binding proteins. *Nat Rev Mol Cell Biol* **19**, 327-341 (2018). https://doi.org/10.1038/nrm.2017.130

148 Geuens, T., Bouhy, D. & Timmerman, V. The hnRNP family: insights into their role in health and disease. *Hum Genet* **135**, 851-867 (2016). https://doi.org/10.1007/s00439-016-1683-5

149 Chaudhury, A., Chander, P. & Howe, P. H. Heterogeneous nuclear ribonucleoproteins (hnRNPs) in cellular processes: Focus on hnRNP E1's multifunctional regulatory roles. *RNA* **16**, 1449-1462 (2010). https://doi.org/10.1261/rna.2254110

150 Han, N., Li, W. & Zhang, M. The function of the RNA-binding protein hnRNP in cancer metastasis. *J Cancer Res Ther* **9 Suppl**, S129-134 (2013). https://doi.org/10.4103/0973-1482.122506

151 Huang, M. *et al.* The C-protein tetramer binds 230 to 240 nucleotides of pre-mRNA and nucleates the assembly of 40S heterogeneous nuclear ribonucleoprotein particles. *Mol Cell Biol* **14**, 518-533 (1994). https://doi.org/10.1128/mcb.14.1.518-533.1994

152 Cáceres, J. F., Stamm, S., Helfman, D. M. & Krainer, A. R. Regulation of alternative splicing in vivo by overexpression of antagonistic splicing factors. *Science* **265**, 1706-1709 (1994). https://doi.org/10.1126/science.8085156

153 Bessonov, S., Anokhina, M., Will, C. L., Urlaub, H. & Lührmann, R. Isolation of an active step I spliceosome and composition of its RNP core. *Nature* **452**, 846-850 (2008). https://doi.org/10.1038/nature06842

154 Wippel, H. H., Fioramonte, M., Chavez, J. D. & Bruce, J. E. Deciphering the architecture and interactome of hnRNP proteins and enigmRBPs. *Mol. Omics* **17**, 503-516 (2021). https://doi.org/10.1039/D1MO00024A

155 Izaurralde, E. *et al.* A role for the M9 transport signal of hnRNP A1 in mRNA nuclear export. *J Cell Biol* **137**, 27-35 (1997). https://doi.org/10.1083/jcb.137.1.27

156 Nair, S. S. & Kumar, R. Chromatin remodeling in cancer: a gateway to regulate gene transcription. *Mol Oncol* **6**, 611-619 (2012). https://doi.org/10.1016/j.molonc.2012.09.005

157 Corona, D. F. *et al.* ISWI is an ATP-dependent nucleosome remodeling factor. *Mol Cell* **3**, 239-245 (1999). https://doi.org/10.1016/s1097-2765(00)80314-7

158 Grüne, T. *et al.* Crystal structure and functional analysis of a nucleosome recognition module of the remodeling factor ISWI. *Mol Cell* **12**, 449-460 (2003). https://doi.org/10.1016/s1097-2765(03)00273-9

159 Li, L. *et al.* Structure of the ISW1a complex bound to the dinucleosome. *Nat Struct Mol Biol* **31**, 266-274 (2024). https://doi.org/10.1038/s41594-023-01174-6

160 Zhang, H. *et al.* Proteome-wide profiling of transcriptional machinery on accessible chromatin with biotinylated transposons. *Sci Adv* **7**, eabh1022 (2021). https://doi.org/10.1126/sciadv.abh1022

161 de Hemptinne, V., Rondas, D., Toepoel, M. & Vancompernolle, K. Phosphorylation on Thr-106 and NO-modification of glyoxalase I suppress the TNF-induced transcriptional activity of NF-kappaB. *Mol Cell Biochem* **325**, 169-178 (2009). https://doi.org/10.1007/s11010-009-0031-7

162 Allaman, I., Bélanger, M. & Magistretti, P. J. Methylglyoxal, the dark side of glycolysis. *Front Neurosci* **9**, 23 (2015). https://doi.org/10.3389/fnins.2015.00023

163 Gatenby, R. A. & Gillies, R. J. Why do cancers have high aerobic glycolysis? *Nat Rev Cancer* **4**, 891-899 (2004). https://doi.org/10.1038/nrc1478

164 Wang, J., Yang, X. & Wang, Z. Role of the Glyoxalase System in Breast Cancer and Gynecological Cancer-Implications for Therapeutic Intervention: a Review. *Front Oncol* **12**, 857746 (2022). https://doi.org/10.3389/fonc.2022.857746

165 Kim, J. Y., Jung, J. H., Lee, S. J., Han, S. S. & Hong, S. H. Glyoxalase 1 as a Therapeutic Target in Cancer and Cancer Stem Cells. *Mol Cells* **45**, 869-876 (2022). https://doi.org/10.14348/molcells.2022.0109

166 Birkenmeier, G. *et al.* Posttranslational modification of human glyoxalase 1 indicates redox-dependent regulation. *PLoS ONE* **5**, e10399 (2010). https://doi.org/10.1371/journal.pone.0010399

167 Bround, M. J., Bers, D. M. & Molkentin, J. D. A 20/20 view of ANT function in mitochondrial biology and necrotic cell death. *Journal of Molecular and Cellular Cardiology* **144**, A3-A13 (2020). https://doi.org/10.1016/j.yjmcc.2020.05.012

168 Ruprecht, J. J. *et al.* The Molecular Mechanism of Transport by the Mitochondrial ADP/ATP Carrier. *Cell* **176**, 435-447.e415 (2019). https://doi.org/10.1016/j.cell.2018.11.025

169 Jang, J. Y., Choi, Y., Jeon, Y. K. & Kim, C. W. Suppression of adenine nucleotide translocase-2 by vector-based siRNA in human breast cancer cells induces apoptosis and inhibits tumor growth in vitro and in vivo. *Breast Cancer Res* **10**, R11 (2008). https://doi.org/10.1186/bcr1857

170 Zhao, L. *et al.* Conformational change of adenine nucleotide translocase-1 mediates cisplatin resistance induced by EBV-LMP1. *EMBO Mol Med* **13**, e14072 (2021). https://doi.org/10.15252/emmm.202114072

171 Mayes, K., Qiu, Z., Alhazmi, A. & Landry, J. W. ATP-dependent chromatin remodeling complexes as novel targets for cancer therapy. *Adv Cancer Res* **121**, 183-233 (2014). https://doi.org/10.1016/B978-0-12-800249-0.00005-6

172 Mittal, P. & Roberts, C. W. M. The SWI/SNF complex in cancer - biology, biomarkers and therapy. *Nat Rev Clin Oncol* **17**, 435-448 (2020). https://doi.org/10.1038/s41571-020-0357-3

173 Rabbani, N., Xue, M., Weickert, M. O. & Thornalley, P. J. Multiple roles of glyoxalase 1-mediated suppression of methylglyoxal glycation in cancer biology-Involvement in tumour suppression, tumour growth, multidrug resistance and target for chemotherapy. *Semin Cancer Biol* **49**, 83-93 (2018). https://doi.org/10.1016/j.semcancer.2017.05.006

174 The UniProt, C. UniProt: a worldwide hub of protein knowledge. *Nucleic Acids Res* **47**, D506-D515 (2019). https://doi.org/10.1093/nar/gky1049

175 Schweppe, D. K. *et al.* XLinkDB 2.0: integrated, large-scale structural analysis of protein crosslinking data. *Bioinformatics* **32**, 2716-2718 (2016). https://doi.org/10.1093/bioinformatics/btw232

176 Shannon, P. Cytoscape: A Software Environment for Integrated Models of Biomolecular Interaction Networks. *Genome Research* **13**, 2498-2504 (2003). https://doi.org/10.1101/gr.1239303

177 Combe, C. W., Fischer, L. & Rappsilber, J. xiNET: Cross-link Network Maps With Residue Resolution. *Molecular & Cellular Proteomics* **14**, 1137-1147 (2015). https://doi.org/10.1074/mcp.O114.042259

178 Rose, A. S. & Hildebrand, P. W. NGL Viewer: a web application for molecular visualization. *Nucleic Acids Res* **43**, W576-W579 (2015). https://doi.org/10.1093/nar/gkv402

179 Pino, L. K., Just, S. C., MacCoss, M. J. & Searle, B. C. Acquiring and Analyzing Data Independent Acquisition Proteomics Experiments without Spectrum Libraries. *Mol Cell Proteomics* **19**, 1088-1103 (2020). https://doi.org/10.1074/mcp.P119.001913

180 Searle, B. C. *et al.* Chromatogram libraries improve peptide detection and quantification by data independent acquisition mass spectrometry. *Nat Commun* **9**, 5128 (2018). https://doi.org/10.1038/s41467-018-07454-w

181 Frezza, C., Cipolat, S. & Scorrano, L. Organelle isolation: functional mitochondria from mouse liver, muscle and cultured fibroblasts. *Nat Protoc* **2**, 287-295 (2007). https://doi.org/10.1038/nprot.2006.478

182 Baysoy, A., Bai, Z., Satija, R. & Fan, R. The technological landscape and applications of single-cell multi-omics. *Nat Rev Mol Cell Biol* **24**, 695-713 (2023). https://doi.org/10.1038/s41580-023-00615-w

183 MacCoss, M. J. *et al.* Sampling the proteome by emerging single-molecule and mass spectrometry methods. *Nat Methods* **20**, 339-346 (2023). https://doi.org/10.1038/s41592-023-01802-5

184 Chavez, J. D. *et al.* Systems structural biology measurements by in vivo cross-linking with mass spectrometry. *Nature Protocols* **14**, 2318-2343 (2019). https://doi.org/10.1038/s41596-019-0181-3

185 Gujarati, N. A., Vasquez, J. M., Bogenhagen, D. F. & Mallipattu, S. K. The complicated role of mitochondria in the podocyte. *Am J Physiol Renal Physiol* **319**, F955-F965 (2020). https://doi.org/10.1152/ajprenal.00393.2020

186 Brinkkoetter, P. T. *et al.* Anaerobic Glycolysis Maintains the Glomerular Filtration Barrier Independent of Mitochondrial Metabolism and Dynamics. *Cell Rep* **27**, 1551-1566.e1555 (2019). https://doi.org/10.1016/j.celrep.2019.04.012

187 Kempson, S. A., Vovor-Dassu, K. & Day, C. Betaine transport in kidney and liver: use of betaine in liver injury. *Cell Physiol Biochem* **32**, 32-40 (2013). https://doi.org/10.1159/000356622

188 Alvarenga, L., Ferreira, M. S., Kemp, J. A. & Mafra, D. The Role of Betaine in Patients With Chronic Kidney Disease: a Narrative Review. *Curr Nutr Rep* **11**, 395-406 (2022). https://doi.org/10.1007/s13668-022-00426-z

189 Patel, D. *et al.* Betaine alleviates doxorubicin-induced nephrotoxicity by preventing oxidative insults, inflammation, and fibrosis through the modulation of Nrf2/HO-1/NLRP3 and TGF-β expression. *J Biochem Mol Toxicol* **38**, e23559 (2024). https://doi.org/10.1002/jbt.23559

190 Rinschen, M. M. *et al.* Accelerated lysine metabolism conveys kidney protection in salt-sensitive hypertension. *Nat Commun* **13**, 4099 (2022). https://doi.org/10.1038/s41467-022-31670-0

191 McMahon, G. M. *et al.* Urinary metabolites along with common and rare genetic variations are associated with incident chronic kidney disease. *Kidney Int* **91**, 1426-1435 (2017). https://doi.org/10.1016/j.kint.2017.01.007

192 Palladino, A. A. & Stanley, C. A. The hyperinsulinism/hyperammonemia syndrome. *Rev Endocr Metab Disord* **11**, 171-178 (2010). https://doi.org/10.1007/s11154-010-9146-0

193 Li, C. *et al.* Mechanism of hyperinsulinism in short-chain 3-hydroxyacyl-CoA dehydrogenase deficiency involves activation of glutamate dehydrogenase. *J Biol Chem* **285**, 31806-31818 (2010). https://doi.org/10.1074/jbc.M110.123638

194 Narayan, S. B. *et al.* Short-chain 3-hydroxyacyl-coenzyme A dehydrogenase associates with a protein super-complex integrating multiple metabolic pathways. *PLoS ONE* **7**, e35048 (2012). https://doi.org/10.1371/journal.pone.0035048

195 Xu, Y., Li, H., Jin, Y. H., Fan, J. & Sun, F. Dimerization interface of 3-hydroxyacyl-CoA dehydrogenase tunes the formation of its catalytic intermediate. *PLoS ONE* **9**, e95965 (2014). https://doi.org/10.1371/journal.pone.0095965